Turbulent bubble suspensions and crystal growth in microgravity
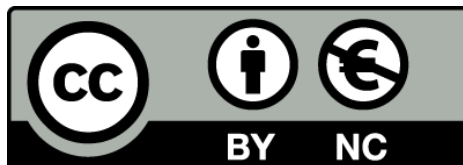
Drop tower experiments and numerical simulations

Pau Bitlloch Puigvert

Turbulent bubble suspensions and crystal growth in microgravity

Drop tower experiments and numerical simulations

P A U   B I T L L O C H   P U I G V E R T

Turbulent bubble suspensions and crystal growth in microgravity

Drop tower experiments and numerical simulations
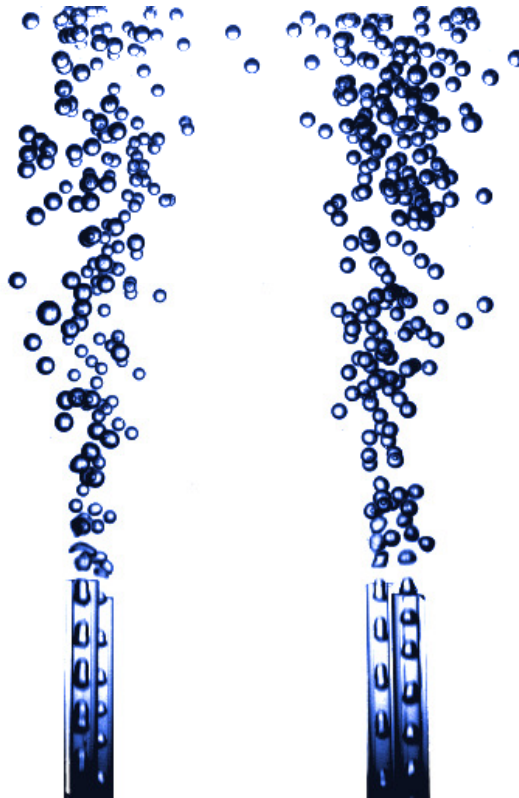
by

PAU BITLLOCH PUIGVERT

Ph.D. advisors:

JAUME CASADEMUNT VIADER

XAVIER RUIZ MARTÍ

UNIVERSITAT DE BARCELONA

Programa de Doctorat en Física

Departament d'Estructura i Constituents de la Matèria

Agraïments / Acknowledgments

Són moltes les persones que m'han inspirat i motivat durant la realització d'aquesta tesi doctoral. Persones que directa o indirectament m'han ajudat en el bonic camí que és la recerca científica. És per a mi molt difícil d'expressar fins a quin punt em sento agraït cap a tots ells, així com l'impacte positiu que han causat en tots els àmbits de la meva vida. Espero que ningú s'ofengui si no troba el seu nom imprès entre aquestes línies. Això no significa que m'hagi oblidat de vosaltres o que us consideri poc dignes de menció, sinó que aquí he hagut de limitar-me a aquells qui han tingut un impacte més directe en la meva tesi.

En primer lloc, vull donar les gràcies als meus directors de tesi, en Jaume i en Xavier, per la confiança i la gran paciència que m'han mostrat al llarg de tots aquests anys. Em considero molt afortunat d'haver tingut la oportunitat de treballar amb vosaltres i mai us ho podré agrair el suficient. El que m'heu ensenyat m'ha ajudat tant en l'àmbit professional com en el personal, i això és una cosa que no oblidaré.

També, és important per a mi donar un especial agraïment a en Laureano Ramírez de la Piscina, qui tot i no ser oficialment un dels meus directors, ha sigut una incessant font d'idees i solucions per als diversos problemes que han anat sorgint durant aquests anys. Moltes gràcies per tot el que m'has ensenyat, pel teu bon humor i, a més, per a ser la persona que va ser capaç d'estabilitzar les meves simulacions de Lattice-Boltzmann amb una sola equació.

An important part of the work in this thesis has been centered in the design and implementation of a new experiment, for its study in the drop tower of ZARM. This would not have been possible without the initial guidance and advice of Michael Dreyer, to whom I am very grateful. I want to thank also the technical staff of the tower for the wonderful hospitality and the invaluable assistance that has provided me throughout all my stays. Special thanks to Frank Ciecior, who helped me in the first designing stages of the project, and to Dieter Bischoff, who took all my requests and dreams and made them much better, and real. Dieter, thank you for your tireless ability to overcome obstacles, your unlimited amount of ideas, your perpetual smile, your great sense of humor and, above all, for your

Contents

Chapter 1

Introduction

Fluid Mechanics is a key area of interest in Science, covering a wide spectrum of important problems, from blood flow through our veins up to ocean currents and hurricane predictions. The same discipline studies how butterflies fly and how convective patterns of plasma self-organize in the sun inner structure. The methods of fluid mechanics have even been applied to model the motion of galaxies [Binney and Tremaine (2008); Lou (2005)], social behaviors in crowds [Narain et al. (2009)], traffic jams [Lighthill and Whitham (1955); Richards (1956)], or evolution of financial markets [Voit (2005)].

From a technological point of view, any significant improvement has a huge impact on society. Everyday, thousands of scientists around the globe work to design better refrigeration systems, combustion propellers or to improve the aerodynamics of high speed vehicles, like planes or cars in F1 races, for example, where they get notorious advances. Overpopulated cities survive thanks to their complex water supply network, many times fed by reservoirs which are regulated by huge dams that are architectural wonders. Even most power plants take advantage of boiling water and the injection of its resulting vapor through large scale turbines in order to convert heat energy into electricity.

The main issue in this area of knowledge is that the governing equations for the motion of fluids, despite they were first introduced in 1822 by Claude Louis Navier and almost two centuries have passed since then, still remain essentially unsolved, a situation that does not seem very likely to change in a near future. This is the reason why, in order to deepen our knowledge of the physics of fluids, and to gain insight into the fundamental mechanisms underlying the large variety of phenomena that they cover, it is useful to learn from the study of particular cases or simple model systems. This is true in particular for the study of turbulence, one of the most difficult problems in fluid mechanics, widely recognized among the few outstanding and most challenging problems in fundamental physics.

1.1   Two-phase flows

From the large spectrum of topics covered by fluid mechanics, two-phase flows constitute a particularly complex area, very common in nature and in technological applications. Some examples can be found on issues like oxygenation of the upper layers of the ocean [Biesheuvel and Wijngaarden (1984)], clouds [Pruppacher et al. (1998)], foams created at the breaking of waves [Peltzer and Griffin (1988)] and even the proper generation and evolution of waves [Kinsman (2012)].

Its study is relevant for understanding drag forces on ships [Carrica et al. (1998)], heat transfer [Ishii and Hibiki (2011); Webb (1994)] and mass transport processes [Sun et al. (2005)], as well as for the construction and development of new and improved engines [Hays and Elliott (1974)], environmental control systems (such as air conditioners), chemical reactors, propulsion systems, and an endless list of other applications. When we apply deodorant spray or shaving foam, or when we eat some deserts of fine cuisine, we benefit from of two-phase flows research funded by beauty and food companies.

One may distinguish two main classes of problems in multiphase flows: free-surface flows, where one has to explicitly solve for the dynamics of a deformable interface, and disperse multiphase flows, characterized by a dispersed phase that is distributed within a carrier phase in the form of particles, droplets, or bubbles, where the evolution of the interface shape is of secondary importance. In part of this thesis we will study an example of the first, in the context of crystal growth, but most of it will be devoted to the study of bubbles dispersed in a liquid phase, all of them in microgravity conditions. The main difficulty in all cases will come from the complexity of the liquid flow, rather than the dynamics of the interfaces.

Dispersed multiphase flows are common in many engineering and environmental applications, and they are often turbulent. If turbulence and multiphase flows are, separately, two of the most challenging topics in fluid mechanics, when combined they pose a formidable challenge [Balachandar and Eaton (2010)]. The inherent fluctuations of the turbulent carrier are further complicated by the random distribution of the dispersed phase, and the existence of break-up and coalescence phenomena. This is why in this work we will put a particular effort in designing experimental conditions to achieve the simplest possible bubble dispersions, aiming at uniform sizes of bubbles and dilute homogeneous distributions, two aspects that find particular difficulties in microgravity.

1.2   Bubbles in Microgravity

Experimentation in microgravity usually entails a substantial increase of technical complexity compared to the corresponding studies on-ground, in addition to the much higher costs. However, the increasing technological demand on the area for space exploration is fostering microgravity research in a continuously growing community. This is particularly true for the study of two-phase flows, widely recognized by all space agencies as a strategic area of research for applications in space technology, being critical in many aspects of life support systems and environmental control for life in space [Hurlbert et al. (2010)], power generation and propulsion [Meyer et al. (2010)], or thermal management with gas-liquid heat exchangers [Hill et al. (2010)]. Many of such situations involve generic problems in phase mixture/separation, two-phase fluid management and control, wetting and contact line dynamics, phase change, or heat and mass transfer. While these processes are encountered in many engineering fields already in terrestrial conditions, the study in non-terrestrial gravity conditions poses additional challenges from the point of view of fundamental physics, in particular because of the limited access to microgravity platforms and the corresponding lack of high quality data.

All the previously cited examples, and others like bioreactors (which require a homogeneous oxygenation of the cell-growth media) or chemical reactors (needing to maximize the contact area between phases), are sensitive to the shape and dimensions of the interface between gas and liquid. They usually benefit from maximizing the ratio of contact-area between phases versus volume of gas, which can usually be achieved by the injection of large amounts of bubbles of small and controlled size. This can be easily accomplished in normal gravity conditions, where buoyancy forces detach bubbles on their own by simply injecting gas into a quiescent cavity, but it is an impotent challenge when buoyancy forces are absent. Then, other mechanisms and physical principles must be exploited to detach bubbles in a controlled manner [Carrera et al. (2006)].

Although two-phase flows research has been continuously expanding in the last decades [McQuillen et al. (1998); Ohta et al. (2002)], that kind of precise bubble control has not been achieved until very recently [Carrera et al. (2008)]. The method first introduced by Carrera et al. consists in the generation of bubbles in a T-Junction of capillary tubes of the order of 1 mm, obtaining a very regular train of bubbles of prescribed size. A more detailed description of the procedure will be reviewed later in Chapter 3, and the same bubble generation system will also be the basis of the experiment detailed in Chapter 4. The practical value of this bubble injection procedure for both fundamental and applied studies has also been exploited in the recent contributions of Suñol (2011) and Arias (2011).

Finally, it is worth remarking that, in addition to the technological motivation

of the study of bubbles in microgravity and its implication for space exploration, there is also a remarkable scientific interest from the point of view of fundamental physics, in the context of turbulent two-phase dispersions mentioned above. In the case of bubbles, the physics of such dispersions is dramatically different from its counterpart with normal gravity, and many subtle effects and interactions that are usually masked by strong buoyancy forces may now emerge. We hope that aiming at the experimental acquisition of relatively high quality microgravity data in sufficiently simplified and controlled conditions, we will gain new insights on fundamental aspects of fluid mechanics, which may eventually turn to be relevant for applications in space technology.

1.3   Reduced gravity facilities

Experimentation in microgravity is currently conducted in a few platforms, which differ largely in the duration and the quality of the reduced gravity, and in the actual cost. In a crescent order of the microgravity duration we have: drop towers, parabolic flights, sounding rockets, orbiting spacecrafts (like space shuttles) and permanent orbital platforms (such as the International Space Station). All of these systems provide a reduced gravity environment by exploiting Einstein's equivalence principle, which states that "The outcome of any local non-gravitational experiment in a freely falling laboratory is independent of the velocity of the laboratory and its location in spacetime" [Haugan and Lammerzahl (2001)]. That means that if we have our experiment confined in a small volume (compared to the scale of variation of the gravity field), following a free fall trajectory (without any external force acting upon it, in addition to gravity), then the observer inside the volume will not be able to distinguish whether he is in free fall or away from any gravitational field.

Drop towers are based on the release of a capsule (with a running experiment) from the top of a tower, and let it have a free fall in the range of 2 to 5 seconds, depending on the facility. One of the main technological issues to overcome is the air frictional force acting upon the falling capsule, which increases over time with the velocity of the object. This introduces an external force that prevents the object from freely falling, consequently modifying the acceleration environment and the effective gravity level. This problem is solved in different ways depending on the facilities. At the ZARM ("Center of Applied Space Technology and Microgravity") drop Tower in Bremen, for example, where all the experiments in the present thesis have been conducted, a complex system of vacuum pumps reduces the pressure inside the whole tower down to 20 Pa prior to the drop, in order to reduce the frictional effects to a negligible point. Thanks to that procedure, a high

quality microgravity is obtained, of the order of $10^{-6}g_0$ (being $g_0 = 9.8m/s^2$ the gravitational acceleration at Earth's surface) during a 4.7 s interval. The ZARM facilities have recently incorporated a catapult system which allows to double that time by throwing the capsule upwards from the bottom of the tower and let it fall again.

The drop tower at INTA ("National Institute of Aerospace Technology") in Madrid, uses a double capsule system for its 2 s free fall, in which frictional effects act upon an external container while the free falling laboratory is inside this external shell, moving relative to it but with reduced friction.

If the experiments require longer times of microgravity, then parabolic flights are the "cheapest" way to increase the reduced gravity time, but at expenses of its quality. These systems are based on planes that describe parabolas of around 20-30 seconds of free fall, during which the engines and the aerodynamics of the plane are used to correct for the residual forces from the friction with the air. The quality of the microgravity is very variable but it rarely achieves values below $10^{-2}g_0$. In addition, the accelerometric signal is subject to strong high-frequency noise (known as g-jitter) due to turbulences affecting the plane. For systems weakly sensitive to the residual gravity this is a good option, because in addition to the duration, many parabolas can be repeated in a single flight. But in the case of bubbles it is a delicate issue that depends on the processes and magnitudes that are going to be studied.

The third class of microgravity platforms in Earth-based facilities is that of Sounding Rockets (or ballistic rockets). In this case, rockets are sent on a sub-orbital flight between 50 km and 1500 km above the surface of the Earth. This trajectory provides 5 to 20 minutes of reduced gravity experimentation far beyond the atmosphere (over 100km from the surface of the planet), thus minimizing frictional effects and other kind of interactions of the capsule with the atmosphere, achieving values of effective gravity of $10^{-5}g_0$ for these long periods of several minutes [NASA (2005)].

Finally, the last possible platform for microgravity research is the use of an orbiting platform such as the ISS, for which the microgravity time is virtually unlimited, although the cost is much greater. It is worth remarking that the quality of the microgravity at the ISS is also subject to some degree of g-jitter, which may depend on the position of the experiment in the structure and on the level of mechanical activity in the station, resulting in a microgravity environment that may be poorer than that in the ZARM Drop Tower.

The issue of the g-jitter, which is generically present in any microgravity platform, is precisely the focus of interest in the chapter of this thesis devoted to simulations of crystal growth, where we study the correlation between the stochastic

variation of the effective acceleration environment, as measured in real microgravity platforms, and the final quality of crystals grown under those conditions.

1.4   Structure of the Book

After the introductory chapter, in chapter 2 we introduce and discuss the main numerical methods used in our research work. On the one hand, the finite-volume methods that are used both for an effective model of turbulence and for the study of semiconductor crystal growth. On the other hand, we discuss extensively the Lattice-Boltzmann method and its use for the study of turbulence.

Chapter 3 is devoted to the study of turbulent bubble jets, carefully processing data from experiments performed by [Carrera et al. (2008)] with particle tracking techniques, and obtaining the jet structure, and the statistics of bubble velocities and their fluctuations. We compare the obtained data with an effective model of turbulent dispersion that we introduce and solve numerically.

In chapter 4 we explain the motivation and the design of a series of experiments conducted at the ZARM drop tower, and the data processing to obtain the statistics of bubble velocities and their fluctuations. Results are compared with Lattice-Boltzmann simulation of the same conditions of the experiment in the absence of bubbles. We also study the distribution of time separation of bubbles and compare with the predictions of the simulation.

Finally, chapter 5 is focused on the impact of g-jitter in the degree of dopant segregation in semiconductor crystal growth in microgravity conditions. We solve the complete problem numerically, and develop an effective model that captures the basic physical mechanisms and may be used as a predictive tool for real systems.

We conclude with a summary of results and perspectives and an appendix with the summary of the thesis in catalan.

Chapter 2

Numerical methods

In the last decades, Computational Fluid Dynamics (CFD) has become a fundamental pillar of study for physics of fluids. Theoretical scientists are continuously searching for better ways to exploit the crescent power of computation provided by new technologies. As time goes by, more physical phenomena are being numerically reproduced, and the improvements in simulation models also increase the accuracy of results. This brings us an extremely valuable tool to complement the experimental approach and to help gaining theoretical insights that cannot be accessed by means of direct analysis of Navier-Stokes equations.

There exist many highly effective models of CFD, each one of them with its own strengths and weaknesses, like Finite Differences, Finite Volumes, Spectral Methods, Large Eddy Simulations, and Lattice-Boltzmann Models, within others. In our focus of study here we face the combination two ingredients that constitute particular challenges from a numerical point of view: two-phase flows and turbulence. In our problems it will be justified to treat the interfaces as non-deformable, so the most demanding aspect of the computation will be to address the simulation of turbulence. In this chapter we will briefly review the numerical methods used in this thesis for problems involving turbulent flows. This will be done at different levels of description, combining both finite-volume integration of effective models of turbulence, described in section 2.1, and first-principle solution of the equations of motion by means of Lattice-Boltzmann methods, described in section 2.2.

2.1   The finite volume method for the k-ε model

2.1.1   Basics of the method

The finite volume method is a widely used technique to solve numerically partial differential equations, and in particular the Navier-Stokes equations in CFD. It is based on the discretization of space into a grid of small volumes, at each of which we assume a homogeneous value of all hydrodynamic magnitudes. Then, as we will see, one obtains the evolution of the flow properties by balancing the incoming/outgoing flux through each side of every particular elementary volume. Here we will not review the details of how this is done in practice, because this is quite standard. In particular, for the numerical computations of turbulent flows conducted with this method we have used the commercial software package FLUENT. For a deeper discussion of the approach, in particular in the context of the effective models of turbulence that we will use here, readers should refer for example to [Versteeg and Malalasekera (1995)].

To introduce the basic insight of the finite-volume method, let us consider the transport equation of a certain scalar magnitude ϕ in a compressible Newtonian fluid, defined by the expression:

$$\frac{\partial(\rho\phi)}{\partial t} + \nabla \cdot (\rho\phi\mathbf{u}) = \nabla \cdot (\Gamma_\phi \nabla\phi) + S_\phi \ , \tag{2.1}$$

where ρ is the density of the fluid, $\mathbf{u}$ the velocity of the flow, Γ_ϕ the diffusion coefficient of ϕ, and S_ϕ a source term of generation of ϕ.

In order to study the evolution of the flow at each elementary volume V, we integrate Equation (2.1) in the form:

$$\int\limits_V \frac{\partial(\rho\phi)}{\partial t}\,dV + \int\limits_V \nabla \cdot (\rho\phi\mathbf{u})\,dV = \int\limits_V \nabla \cdot (\Gamma_\phi \nabla\phi)\,dV + \int\limits_V S_\phi\,dV \ . \tag{2.2}$$

Now we can simplify the resulting equation by means of Gauss's divergence theorem:

$$\int\limits_V (\nabla \cdot \mathbf{a})\,dV = \oint\limits_A (\hat{\mathbf{n}} \cdot \mathbf{a})\,dA \ . \tag{2.3}$$

Here, the integral is over the whole closed surface A which encloses the volume V, and $\hat{\mathbf{n}}$ is the unity vector with direction perpendicular to the surface element dA. Applying this equivalence to equation (2.2), and integrating over one time step δt

of the simulation, we reach the expression:

$$\int_{\delta t} \frac{\partial}{\partial t} \left(\int_V (\rho \phi) \, dV \right) dt + \int_{\delta t} \oint_A \hat{\mathbf{n}} \cdot (\rho \phi \mathbf{u}) \, dA \, dt =$$
$$= \int_{\delta t} \oint_A \hat{\mathbf{n}} \cdot (\Gamma_\phi \nabla \phi) \, dA \, dt + \int_{\delta t} \int_V S_\phi \, dV \, dt \, . \tag{2.4}$$

This equation, is the commonly used by most CFD codes using finite volumes. By properly adjusting the diffusion coefficient Γ_ϕ and the source term S_ϕ, one can take ϕ as each of the velocity components (u_x, u_y, u_z), the temperature T or any other scalar variable φ.

The first term at left-hand side of equation (2.4) describes the variation of the concentration of ϕ in the volume during one time step. The second term stands for the net flow of the scalar advected through the closed surface A. The first term at the right-hand side, corresponds to the net flux of ϕ diffused through the surface. Finally, last term is the amount of ϕ that has been generated inside the volume.

The numerical approach of the problem of crystal growth addressed in chapter 5, which involves both (non-turbulent) fluid flow and thermo-solutal transport, will be based on finite-volume methods and the details will be discussed specifically in that chapter. In this chapter we are concerned with the specific difficulties that arise when dealing with turbulent flows, present in any CFD strategy, due to the inherent dynamic instability of the flow and its complex multiple-scale spatio-temporal structure. In the context of finite-volume methods, it becomes impossible to specify a grid of elementary volumes fine enough to fully describe all the scales of turbulence, because of the prohibitive computer time required to numerically solve it. In order to overcome this problem, different approximation strategies have been proposed to coarse-grain the flow at small scales while keeping the effective dynamics at larger scales as correct as possible. The rationale of the approach is to define some type of averaging that reduces the problem to a mean flow that looks as laminar, plus a small perturbation that contains the fluctuations, i.e. we write

$$\mathbf{u} = \mathbf{U} + \mathbf{u}' = (U_x + u'_x, U_y + u'_y, U_z + u'_z) \, , \tag{2.5}$$

where we define the velocity of the flow $\mathbf{u}$ as the sum of the mean velocity $\mathbf{U}$ of the volume during one time step, and the fluctuating part $\mathbf{u}'$ with zero mean, that describes the fast fluctuations in this volume. We can split any other scalar variable φ in the same way:

$$\varphi = \Phi + \varphi' \, . \tag{2.6}$$

The idea is then to find the effective equations for the mean flow after proper averaging over the fast fluctuating components. This yields a set of effective transport equations for a compressible newtonian fluid of the form:

$$\frac{\partial \rho}{\partial t} + \nabla \cdot (\rho \mathbf{U}) = 0 \tag{2.7}$$

$$\begin{cases} \frac{\partial(\rho U_x)}{\partial t} + \nabla \cdot (\rho U_x \mathbf{U}) = \nabla \cdot (\mu \nabla U_x) - \left[\frac{\partial(\rho \overline{u_x'^2})}{\partial x} + \frac{\partial(\rho \overline{u_x' u_y'})}{\partial y} + \frac{\partial(\rho \overline{u_x' u_z'})}{\partial z} \right] - \frac{\partial P}{\partial x} + S_x \; . \\[3mm] \frac{\partial(\rho U_y)}{\partial t} + \nabla \cdot (\rho U_y \mathbf{U}) = \nabla \cdot (\mu \nabla U_y) - \left[\frac{\partial(\rho \overline{u_x' u_y'})}{\partial x} + \frac{\partial(\rho \overline{u_y'^2})}{\partial y} + \frac{\partial(\rho \overline{u_y' u_z'})}{\partial z} \right] - \frac{\partial P}{\partial y} + S_y \; . \\[3mm] \frac{\partial(\rho U_z)}{\partial t} + \nabla \cdot (\rho U_z \mathbf{U}) = \nabla \cdot (\mu \nabla U_z) - \left[\frac{\partial(\rho \overline{u_x' u_z'})}{\partial x} + \frac{\partial(\rho \overline{u_y' u_z'})}{\partial y} + \frac{\partial(\rho \overline{u_z'^2})}{\partial z} \right] - \frac{\partial P}{\partial z} + S_z \; . \end{cases} \tag{2.8}$$

$$\frac{\partial(\rho \Phi)}{\partial t} + \nabla \cdot (\rho \Phi \mathbf{U}) = \nabla \cdot (\Gamma_\Phi \nabla \Phi) - \left[\frac{\partial(\rho \overline{u_x' \varphi'})}{\partial x} + \frac{\partial(\rho \overline{u_y' \varphi'})}{\partial y} + \frac{\partial(\rho \overline{u_z' \varphi'})}{\partial z} \right] + S_\Phi \; . \tag{2.9}$$

where μ stands for the dynamic viscosity of the flow and P is the pressure.

The equations are not yet closed until we specify an explicit form for the averages of the fluctuating terms $\overline{u_i' u_j'}$. This cannot be performed exactly, and different choices for those terms define different approximations, that may be more or less accurate depending on the type of flows and geometries under study. In the literature one can find many different models of turbulence based on this scheme, with a variable complexity and computational cost that range from very simple assumptions up to the inclusion of six new partial differential equations (for the so-called Reynolds stress equations). In the next section, we will focus on the so-called $k - \varepsilon$ models, specifically on the so-called realizable $k - \varepsilon$ [Shih et al. (1995)].

2.1.2   Realizable $k - \varepsilon$ model

The so-called $k - \varepsilon$ models are based on the description of the fluctuating part of the flow in terms of two fields, the local turbulent kinetic energy k of the fluctuating part, and its dissipation rate ε. This introduces two new transport equations coupled to the system of equations (2.7), (2.8) and (2.9), as we will see later.

The kinetic energy of turbulence per unit mass is defined by the expression:

$$k = \frac{1}{2}\left(\overline{u_x'^2} + \overline{u_y'^2} + \overline{u_z'^2}\right) . \tag{2.10}$$

We relate this magnitude to equations (2.8) and (2.9) by means of an extended Boussinesq relationship of the form:

$$-\rho\overline{u_i'u_j'} = \mu_t\left(\frac{\partial U_i}{\partial x_j} + \frac{\partial U_j}{\partial x_i}\right) - \frac{2}{3}\rho k\delta_{ij} = 2\mu_t E_{ij} - \frac{2}{3}\rho k\delta_{ij} . \tag{2.11}$$

where we have used the definition of the rate-of-strain tensor E_{ij} ,

$$E_{ij} = \frac{1}{2}\left(\frac{\partial U_i}{\partial x_j} + \frac{\partial U_j}{\partial x_i}\right) . \tag{2.12}$$

Finally, μ_t stands for the so-called eddy viscosity, defined by:

$$\mu_t = \rho C_\mu \frac{k^2}{\varepsilon} , \tag{2.13}$$

where C_μ is a constant to be fitted to optimize the results, which in the most standard case is usually taken as $C_\mu = 0.09$.

One of the shortcomings of the method is that it uses assumptions of isotropic turbulence. As we can see at equation (2.11), we impose one third of the total kinetic energy of the turbulence at each direction.

In the case of interest here for the application of this approach, namely the study of turbulent jets, the standard $k - \varepsilon$ model predicts opening angles of jets slightly excessive (a point that is of crucial importance for our study). This is the reason why we use an improved version, the so-called realizable $k - \varepsilon$ model [Shih et al. (1995)]. This introduces the transport equations:

$$\frac{\partial(\rho k)}{\partial t} + \nabla \cdot (\rho k\mathbf{U}) = \nabla \cdot \left[\left(\mu + \frac{\mu_t}{\sigma_k}\right)\nabla k\right] + 2\mu_t E_{ij} \cdot E_{ij} - \rho\varepsilon , \tag{2.14}$$

$$\frac{\partial(\rho\varepsilon)}{\partial t} + \nabla \cdot (\rho\varepsilon\mathbf{U}) = \nabla \cdot \left[\left(\mu + \frac{\mu_t}{\sigma_\varepsilon}\right)\nabla\varepsilon\right] - \rho C_2\frac{\varepsilon^2}{k + \sqrt{\nu\varepsilon}} , \tag{2.15}$$

which are slightly different from those of the standard model, and in addition take C_μ, defined in equation (2.13), as a flow depending function (instead of a constant parameter), with the form:

$$C_\mu = \frac{1}{A_0 + A_s\frac{kU^{(*)}}{\varepsilon}} , \tag{2.16}$$

where

$$U^{(*)} = \sqrt{E_{ij}E_{ij} + \Omega_{ij}\Omega_{ij}} \ , \tag{2.17}$$

$$\Omega_{ij} = \frac{1}{2}\left(\frac{\partial U_i}{\partial x_j} - \frac{\partial U_j}{\partial x_i}\right) \ . \tag{2.18}$$

The other constants, *i.e.*

$$A_0 = 4.04, \quad A_s = \sqrt{6}cos\phi \ , \tag{2.19}$$

$$\phi = \frac{1}{3}cos^{-1}\left(\sqrt{6}\frac{E_{ij}E_{jk}E_{ki}}{(\sqrt{E_{ij}E_{ij}})^3}\right) \ , \tag{2.20}$$

$$C_2 = 1.9, \ \sigma_k = 1.0, \ \sigma_\varepsilon = 1.2 \ , \tag{2.21}$$

have been fitted to values that offer an overall optimal performance of the model.

In chapter 3 we will carry out the numerical integration of this model by means of the package FLUENT as a reference calculation to understand the behavior of bubbles within a jet, in particular to work out to what extent their interaction with the carrying jet may be considered as that of a passive tracer.

2.2   Lattice-Boltzmann simulations

When facing Navier-Stokes equations, we have to deal with a set of coupled non-linear differential equations. In most CFD models, this brings up the issue that evolution of each fluid element typically depends on the whole system, which prevents to take full advantage of parallel computing. The Lattice-Boltzmann approach, however, presents a way of numerically solving the Navier-Stokes equations in a completely local manner, well amenable to massive parallelization. As we will see in next sections, this means that for a small time step, each fluid element is only affected by its nearest neighbors, allowing to split the computational effort of any simulation within any number of CPUs, thus reducing in that way the computer time of calculation virtually by the same factor. The Lattice-Boltzmann approach has become more and more competitive in recent years with respect to more traditional methods, due to its versatility and its adaptation to massively parallel computing in modern supercomputers with hundreds or even thousands of CPU units, and is currently appreciated by the CFD community as one of the most powerful methods, in particular in the study of complex fluids and complex flows (such as for turbulence).

The Lattice Boltzmann Model was born from the idea of addressing computational fluid dynamics from a microscopic point of view, using the concepts of kinetic theory but without trying to describe the flow by tracking actual particles

at molecular level. Solving the exact microscopic dynamics is obviously out of the question, because of the huge computational effort to obtain lots of useless information (even assuming that we know the initial condition of all particles, it would take longer than the age of the universe to simulate a few seconds of our experiment). On the basis that microscopic details are not relevant to a hydrodynamic description, we can make use of statistical mechanics. More specifically, the method is inspired in kinetic theory by assuming time-dependent one-particle distribution functions of the microscopic observables at each spatial cell, and defining the evolution of those distributions in accordance with the appropriate collision terms that govern the transport of conserved quantities.

In the following sections we present the basic principles as well as the simple but useful tools necessary to build a Lattice-Boltzmann simulation scheme. We do not pretend to provide here a complete an exhaustive description of the model. For more information we recommend [Succi (2001)], [Chen and Doolen (1998)], [Aidun and Clausen (2010)] and [Nourgaliev et al. (2003)], amongst many others.

2.2.1   Boltzmann Equation

Given an ensemble of particles, we can specify their probability distribution function as $f(\mathbf{r}, \mathbf{e}, t)$. This construction stands for the distribution of single particles at position $\mathbf{r}$ with velocity $\mathbf{e}$ at instant t. By integrating f over all velocities, we obtain the density of particles ρ at each point $\mathbf{r}$:

$$N = \rho(\mathbf{r}, t)d^3r = d^3r \int_{e_x=-\infty}^{e_x=+\infty} \int_{e_y=-\infty}^{e_y=+\infty} \int_{e_z=-\infty}^{e_z=+\infty} f(\mathbf{r}, \mathbf{e}, t)d^3e \,, \qquad (2.22)$$

where N is the number of particles contained in a differential element of fluid d^3r placed on $\mathbf{r}$ at time t.

Evolution of f with time can be expressed when realizing that changes in the flow of that distribution (expressed by means of the material derivative) can only be caused by particle interactions. Then we obtain (as seen, for example, in [Huang (1963)]):

$$(\partial_t + \mathbf{e} \cdot \nabla_r + \mathbf{a} \cdot \nabla_{\mathbf{e}}) f(\mathbf{r}, \mathbf{e}, t) = \Omega_{coll} \,. \qquad (2.23)$$

In this expression, $\mathbf{a}$ stands for an external force that is being applied upon a volume element. At the right-hand side of the equation, Ω_{coll} represents the effect of the collision between particles, which was expressed by Boltzmann (1872) as

$$\Omega_{coll} = \int d\phi \int d^3e^{(0)}\sigma(\phi)|\mathbf{e} - \mathbf{e}^{(0)}|(f'f'^{(0)} - ff^{(0)}) \,, \qquad (2.24)$$

where f' denote the distribution function after the collision, ϕ is the scattering

angle and σ, the differential cross-section of the collision. Here, some assumptions have been made. In the first place, it only takes into account particle interactions in pairs, which is a rule that only fits for very dilute gases. It also assumes that velocity is statistically uncorrelated with position, which stands for the hypothesis of molecular chaos or Boltzmann's *stosszahlansatz* [Nourgaliev et al. (2003)].

The link of kinetic theory to thermodynamics, stems from from Boltzmann's $\mathbb{H}$-theorem, which states that for solutions of the Boltzmann equation, the function $\mathbb{H}(t)$ defined by:

$$\mathbb{H} = \int -f \ln f d\mathbf{e} \, , \tag{2.25}$$

for a closed system, is always a monotonically non-increasing function of time, i.e.:

$$\frac{d\mathbb{H}}{dt} \geq 0 \, , \tag{2.26}$$

which connects the statistics of collisions to entropy and the second law of thermodynamics.

2.2.2 BGK-Model

In practice, equation (2.24) provides a collision term too complicated to be introduced in a simulation method. This is why we can find in literature several methods of Lattice-Boltzmann simulation, which differ in the approach they use for the collision term. In recent years, equation (2.24) has been widely studied and modeled. The most popular approach is the Bhatnagar-Gross-Krook (BGK) approximation. This model arises from an assumption of having, for each element of fluid, a local near-equilibrium distribution. Then, with a sufficiently large ensemble of particles (to be statistically relevant), collisions should relax to the distribution of local equilibrium (as $\mathbb{H}(t)$ shows us in (2.26)). We can express this local equilibrium distribution with the Maxwellian configuration [He and Luo (1997)]:

$$f^{eq} = \frac{\rho}{(2\pi RT)^{\mathbb{D}_0/2}} \exp\left[-\frac{(\mathbf{e} - \mathbf{u})^2}{2RT}\right] \, , \tag{2.27}$$

being R the gas constant and $\mathbb{D}_0$ the space dimension. This expression depends on hydrodynamic magnitudes such as temperature T, density ρ and flow velocity $\mathbf{u}$, which are measured for a uniform element of fluid, and at the same time it depends on the single-particle velocity $\mathbf{e}$ for which we are calculating the distribution function.

Once we have established f^{eq}, we express the local relaxation term Ω_{coll} of the distribution function as stated by BGK collision operator (introduced by Bhatna-

gar et al. (1954)):

$$\Omega_{coll} = -\frac{f - f^{eq}}{\tau^\star} \, , \tag{2.28}$$

being $\tau^\star$ a relaxation time.

The major strength of this model is the accuracy of results that is capable to reproduce in spite of its enormous simplicity. However, as pointed out by Succi (2001), having only one relaxation time implies that mass, momentum and heat transfer all take place at the same rate, and this is only appropriate for ideal gases. We can find several studies in the literature that perform much elaborated Lattice-Boltzmann simulations with multiple relaxation times in order to avoid this simplification [d'Humieres et al. (2002); Premnath et al. (2009)]. They also exploit the fact that when having multiple relaxation times, it is possible to tune them in order to increase the stability of the model. Those improvements are mandatory for some specific configurations, but it seems that they are not strictly necessary for the present studies, and for that reason they will not be described here. Instead, we will restrict our discussions to LBGK (Lattice BGK) model with a single relaxation time, which has proven to be a really efficient and simple model. Also, we will consider an isothermal system, but any reader interested can find an application of LBGK model with heat transfer in [Chew et al. (2006)].

Incorporating the collision term from equation (2.28) into expression (2.23) and rearranging, we obtain:

$$\left(\partial_t + \mathbf{e} \cdot \nabla_r\right) f = -\frac{f - f^{eq}}{\tau^\star} - \mathbf{a} \cdot \nabla_\mathbf{e} f \, . \tag{2.29}$$

In order to solve the last term in the right-hand side of the previous equation, we can make a call to the hypothesis of near equilibrium distribution, assuming that

$$\nabla_\mathbf{e} f \approx \nabla_\mathbf{e} f^{eq} \, , \tag{2.30}$$

which, deriving equation (2.27), brings us to

$$\nabla_\mathbf{e} f \approx \nabla_\mathbf{e} f^{eq} = -\frac{(\mathbf{e} - \mathbf{u})}{RT} f^{eq} \, . \tag{2.31}$$

Finally, by introducing this approximation into equation (2.29) we obtain that

$$\left(\partial_t + \mathbf{e} \cdot \nabla_r\right) f = -\frac{f - f^{eq}}{\tau^\star} + \frac{\mathbf{a} \cdot (\mathbf{e} - \mathbf{u})}{RT} f^{eq} \, . \tag{2.32}$$

In the left-hand side of the equation, we have the streaming operator, which stands for the propagation of the distribution function. In the right-hand side, we find a first term that takes into account the statistical effect of the collisions

between particles, which causes the relaxation of the distribution function to the local equilibrium. The last term in the right-hand side is the force term on the fluid element. As we will see in section 2.2.6, about Boundary Conditions, there are different ways of reproduce a constant flow in a simulation, but the one that we are going to implement requires to specify a force at each fluid element, to account for the overall pressure drop between the ends of the system that drives the constant flow.

2.2.3   Discretizing the model

In order to find the numerical evolution in time of equation (2.32), we must discretize all the arguments of the distribution function, that is, position ($\mathbf{r}$), particle velocity ($\mathbf{e}$) and time (t).

Discretizing space

For space discretization, we create a lattice of equispaced points with a separation between first neighbors of δx (Figure 2.1). Each node of the grid represents an element of fluid sufficiently small to have all the hydrodynamic magnitudes constant in the corresponding volume (Figure 2.2). Typically, the criteria to set how fine the grid must be depends on the length scale of the smallest phenomenon that one wants to be able to reproduce, since anything occurring at smaller scales of the grid will not be reproduced but at the same time may cause numerical instabilities if not properly filtered out (as we will see later, in section 2.2.8). We also need to keep in mind that sometimes larger scale effects emerge from smaller ones, and for that reason we need to make sure that our mesh is fine enough to reproduce all the significant scales.

It is also imperative to create the space discretization fine enough to prevent big changes between neighbor nodes of any magnitude. All spatial changes (as well as the temporal ones) should be sufficiently smooth, otherwise instabilities would arise.

Often when designing the lattice size, we feel constrained by computational limitations and we cannot choose the size of the grid that we would like to. Maybe we need a much thiner and precise lattice for some critical areas of the simulation (like near the walls, for example), while we could use a coarser grid for the rest of the experiment. The answer to this problem can be found on some elaborate ways of using compost grids with different lattice sizes, which serve to refine the grid only in the parts where it is needed, saving a lot of computational time [Lin and Lai (2000)].
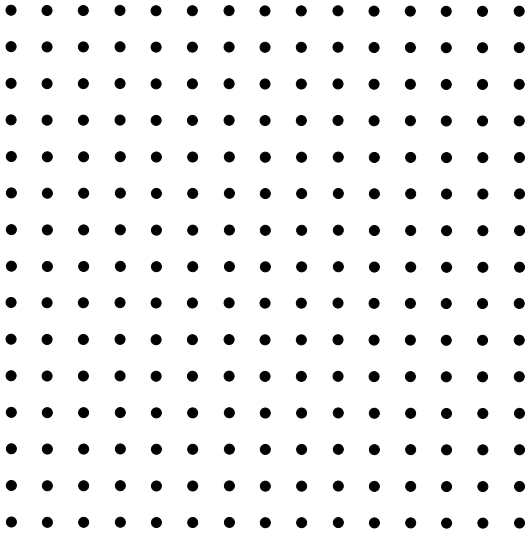
Figure 2.1: Space discretization
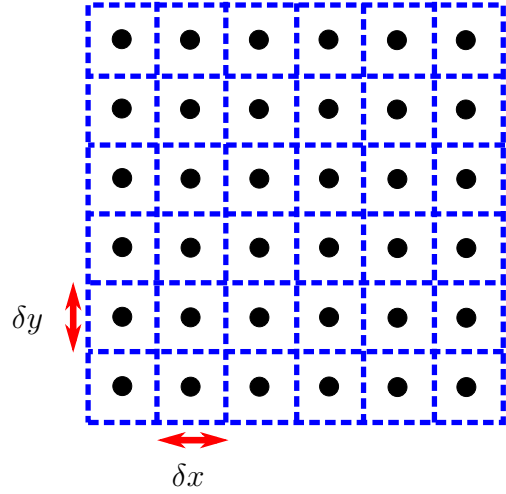
Figure 2.2: Two dimensional space lattice

Discretizing velocity and time

When choosing the discretized particle velocities $\mathbf{e}_k$, we demand that for each time step δt, all particles must reach simultaneously one neighbor node. It is not possible for any particle to be placed elsewhere between nodes, they must all collide at the same point. In that way, our model becomes much simpler and computationally more efficient.

As a matter of simplification, we define f_k as the distribution function with velocity $\mathbf{e}_k$, i.e.:

$$f_k(\mathbf{r}, t) \equiv f(\mathbf{r}, \mathbf{e_k}, t) \; . \tag{2.33}$$

Figure 2.3 shows an example of streaming the distribution functions in a two-dimensional space. In that example, each particle can take one of the 9 possible velocities, each one of them taking the particles to another of the 8 surrounding nodes in one exact δt, or remaining at the same initial node.

Once we have limited in this way the range of possible particle velocities, those also restrain our time discretization. The key point is that if we have a really thin space grid with a large time step, particles will not be fast enough to transmit the information of the real macroscopic changes in the flow, and this will break down our system due to instabilities. For instance, it is not possible to correctly simulate a system in which some hydrodynamic effects are moving faster than our fastest lattice particle velocity. This behavior draws a line for the largest time step possible, which is the time needed for the information to travel one δx in our space grid. That speed at which the information travels through our lattice is what we know as lattice sound velocity c_s. As we can find in [He and Luo (1997)],
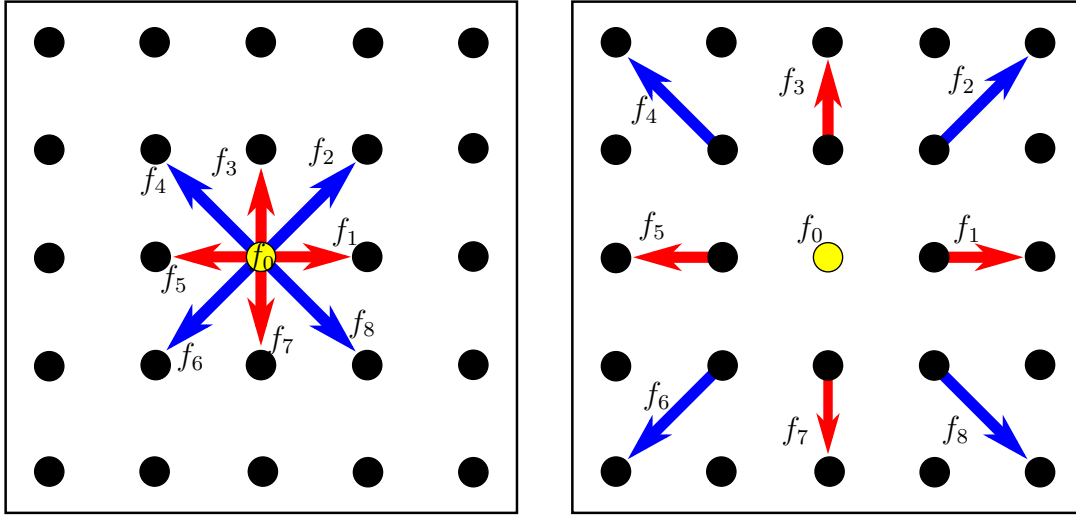
(a) Before streming ($t = t_0$). All functions belong to the central yellow node.

(b) After streaming ($t = t_0 + \delta t$). Each function belong to a different node

Figure 2.3: Streaming of the distribution functions from the central yellow node in a D2Q9 configuration after one simple time step δt

this pseudo-sound speed of a 3D lattice is defined by:

$$c_s \equiv \sqrt{RT} \ , \tag{2.34}$$

$$c_s = \frac{c}{\sqrt{3}} \ . \tag{2.35}$$

$$c = \frac{\delta x}{\delta t} \ . \tag{2.36}$$

If we want to work with incompressible liquids, it is clear from a theoretical point of view that most of the effects should be instantaneous (corresponding to $\delta t \approx 0$ or $c_s \approx \infty$). In order to reach a fair degree of incompressibility, we need all fluid velocities to be much smaller than the lattice sound velocity. That is achieved by decreasing the time step, but this implies increasing the computation time, which is usually an important limiting factor. Simulations may easily take hundreds or thousands of hours on nowadays computers, so it is often not possible to take the time step as small as we would desire on physical principles. In our experience, it is usually enough to take c_s around 10 times bigger than the maximum flow velocity ($u_{\max}$) of the experiment. This can be expressed in terms of the Mach number of the lattice (Ma):

$$Ma = \frac{u_{\max}}{c_s} < 0.1 \ . \tag{2.37}$$

Equation (2.37), in conjunction with the definitions of c_s and c that we find

respectively in equations (2.35) and (2.36), leads us to an expression for the maximum time step of the form

$$\delta t < \frac{0.1}{\sqrt{3}}\delta x \approx 0.06\delta x \; . \tag{2.38}$$

In these conditions, executing highly turbulent simulations, we get a maximum degree of compressibility smaller than 0.3%. This is an acceptable error range, taking into account all the approximations that have been used.

DdQq models

As already stated, we impose that for any time step, all particles reach a node, so we never have any particle in an intermediate point, and that they only travel to their nearest neighbors. That kind of configurations are typically called DdQq in which "d" stands for the number of dimensions of our space, and "q" is the number of particle velocities allowed in the model (for example, D2Q9 is a model of nine possible particle velocities in a two-dimensional space). What we need to take into account is that not all velocity discretizations can be used to reproduce realistic physical phenomena. For example, in a 2D configuration, if we use a D2Q5 model (corresponding to Figure 2.3 without the 4 diagonal velocities), we will not have a complete ensemble of possible particle velocities. This produces that it is not possible to describe properly all macroscopic behaviors, regardless of how thin we would build our space lattice, and how small we would make our time step. In fact, this model leads to some kind of artificial non-realistic eddies of square shape (as discussed by Succi (2001)).

The key point is to choose a set of velocities with enough symmetry and rotational invariance to be able to recover the Navier-Stokes equations in the appropriate limit. This has been thoroughly studied by many authors [Qian et al. (1992); Succi (2001); Nourgaliev et al. (2003)], and in a 3D space, there are only 3 universally used models: D3Q15, D3Q19 and D3Q27.

As one increases the number of possible particle velocities, one is also increasing the number of neighbors associated to each lattice node. Theoretically, this better interconnection should improve the stability of the model, but it also increases the complexity and computational load of simulations. In Figures 2.4 and 2.5, we can see the schematics of configurations D3Q15 and D3Q19, respectively. Particle velocities for both cases are written in detail in Table 2.1.

Once one has discretized the system, one needs to express the equilibrium distribution function in terms of the new lattice particle velocities. In order to do that, we use the Chapman-Enskog expansion (as discussed in Qian et al. (1992)),
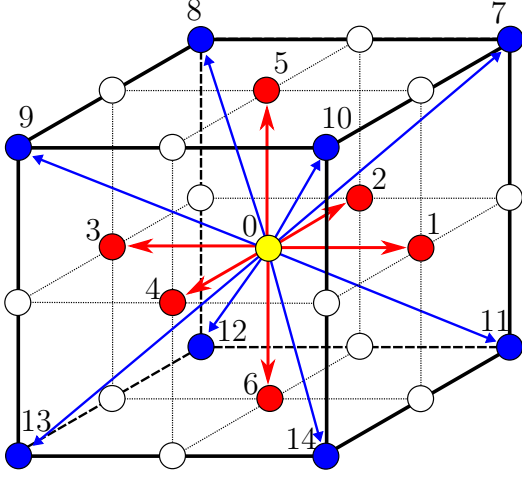
Figure 2.4: D3Q15 model   **Figure 2.5:** D3Q19 model
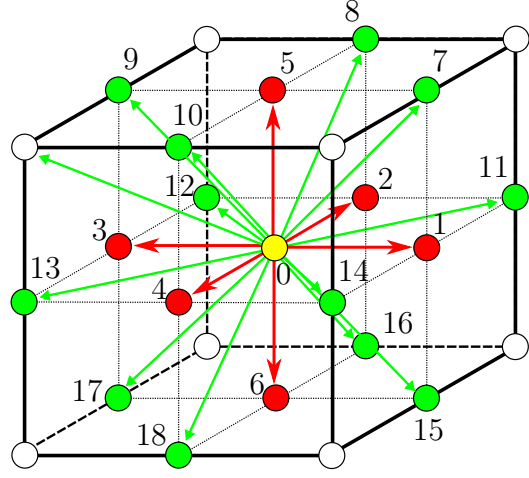
leading to:

$$f_k^{eq} = \rho w_k \left(1 - \frac{\mathbf{u}}{2c_s^2} + \frac{\mathbf{e}_k \cdot \mathbf{u}}{c_s^2} + \frac{(\mathbf{e}_k \cdot \mathbf{u})^2}{2c_s^4} \right) \ , \tag{2.39}$$

which works only for small Mach numbers.

Discretized BGK-model

Now we are in the conditions to express equation (2.32) in terms of the discretized variables that we will use in a simulation. In the first place, we can express it in terms of $\mathbf{e}_k$ as

$$\left(\partial_t + \mathbf{e}_k \cdot \nabla_r \right) f_k = -\frac{f_k - f_k^{eq}}{\tau^\star} + \frac{\mathbf{a} \cdot (\mathbf{e}_k - \mathbf{u})}{c_s^2} f_k^{eq} \ . \tag{2.40}$$

Terms on left-hand side of this equation can be discretized by means of Taylor expansions:

$$\partial_t f_k(\mathbf{r}, t) = \frac{f_k(\mathbf{r}, t + \delta t) - f_k(\mathbf{r}, t)}{\delta t} \ , \tag{2.41}$$

$$\mathbf{e}_k \cdot \nabla_r f_k(\mathbf{r}, t + \delta t) = \frac{f_k(\mathbf{r} + \mathbf{e}_k \delta t, t + \delta t) - f_k(\mathbf{r}, t + \delta t)}{\delta t} \ , \tag{2.42}$$

and by assuming that

$$\mathbf{e}_k \cdot \nabla_r f_k(\mathbf{r}, t) \approx \mathbf{e}_k \cdot \nabla_r f_k(\mathbf{r}, t + \delta t) \ , \tag{2.43}$$

combining equations (2.41) and (2.42) we finally obtain

$$\partial_t f_k(\mathbf{r}, t) + \mathbf{e_k} \cdot \nabla_r f_k(\mathbf{r}, t) = \frac{f_k(\mathbf{r} + \mathbf{e}_k \delta t, t + \delta t) - f_k(\mathbf{r}, t)}{\delta t} \ , \tag{2.44}$$

k	$\mathbf{e}_k$	w_k
0	$(0, 0, 0)$	$1/3$
1	$(+1, 0, 0)c$	$1/18$
2	$(0, +1, 0)c$	$1/18$
3	$(-1, 0, 0)c$	$1/18$
4	$(0, -1, 0)c$	$1/18$
5	$(0, 0, +1)c$	$1/18$
6	$(0, 0, -1)c$	$1/18$
7	$(+1, 0, +1)c$	$1/36$
8	$(0, +1, +1)c$	$1/36$
9	$(-1, 0, +1)c$	$1/36$
10	$(0, -1, +1)c$	$1/36$
11	$(+1, +1, 0)c$	$1/36$
12	$(-1, +1, 0)c$	$1/36$
13	$(-1, -1, 0)c$	$1/36$
14	$(+1, -1, 0)c$	$1/36$
15	$(+1, 0, -1)c$	$1/36$
16	$(0, +1, -1)c$	$1/36$
17	$(-1, 0, -1)c$	$1/36$
18	$(0, -1, -1)c$	$1/36$

(b) D3Q19

k	$\mathbf{e}_k$	w_k
0	$(0, 0, 0)$	$2/9$
1	$(+1, 0, 0)c$	$1/9$
2	$(0, +1, 0)c$	$1/9$
3	$(-1, 0, 0)c$	$1/9$
4	$(0, -1, 0)c$	$1/9$
5	$(0, 0, +1)c$	$1/9$
6	$(0, 0, -1)c$	$1/9$
7	$(+1, +1, +1)c$	$1/72$
8	$(-1, +1, +1)c$	$1/72$
9	$(-1, -1, +1)c$	$1/72$
10	$(+1, -1, +1)c$	$1/72$
11	$(+1, +1, -1)c$	$1/72$
12	$(-1, +1, -1)c$	$1/72$
13	$(-1, -1, -1)c$	$1/72$
14	$(+1, -1, -1)c$	$1/72$

(a) D3Q15

Table 2.1: Particle Velocities $\mathbf{e}_k$ and weights w_k of D3Q15 and D3Q19 configurations

which is called the Taylor expansion of the finite streaming operator. Introducing equation (2.44) into (2.40) and rearranging we get

$$f_k(\mathbf{r} + \mathbf{e}_k \delta t, t + \delta t) = \left(1 - \frac{1}{\tau}\right) f_k(\mathbf{r}, t) + \left[\frac{1}{\tau} + \mathbf{a} \cdot \frac{(\mathbf{e}_k - \mathbf{u})}{c_s^2} \delta t\right] f_k^{eq}(\mathbf{r}, t) , \quad (2.45)$$

where $\tau = \frac{\tau^\star}{\delta t}$ is the nondimensionalized version (in units of δt) of the relaxation time. Note that all hydrodynamic variables (i.e., $\mathbf{u}$ and $\mathbf{a}$) are also calculated at the node at position $\mathbf{r}$ at time t. With regard to the force term $\mathbf{a}$, there are many other suitable ways of implementing it, as the one explained by Du and Shi (2006).

As seen by Alexander et al. (1993), Sterling and Chen (1996) and Nourgaliev et al. (2003), from Equation 2.45 one finds that the kinetic viscosity ν of the fluid in the simulation is determined by

$$\nu = \left(\tau - \frac{1}{2}\right) \delta_t c_s^2 . \quad (2.46)$$

2.2.4   Hydrodynamic magnitudes

The ultimate goal of the Lattice-Boltzmann method, like in any other CFD method, is to obtain the time evolution of the macroscopic properties of the system. Those magnitudes arise from the calculation of the moments of order 0 and 1 of the distribution function:

$$\rho(\mathbf{r}, t) = \int [f(\mathbf{r}, \mathbf{e}, t)] d\mathbf{e} = \int [f^{eq}(\mathbf{r}, \mathbf{e}, t)] d\mathbf{e} \ . \tag{2.47}$$

$$\rho(\mathbf{r}, t) \mathbf{u}(\mathbf{r}, t) = \int [\mathbf{e}\, f(\mathbf{r}, \mathbf{e}, t)] d\mathbf{e} = \int [\mathbf{e}\, f^{eq}(\mathbf{r}, \mathbf{e}, t)] d\mathbf{e} \ . \tag{2.48}$$

Accordingly, we are claiming that the moments calculated using f^{eq} yield the same result than using the actual distribution function. This property is satisfied by construction.

Once that we have discretized the particle velocities $\mathbf{e}_k$, equations (2.47) and (2.48) become, respectively, for a given node at a given time t:

$$\rho = \sum_k f_k = \sum_k f_k^{eq} \ . \tag{2.49}$$

$$\rho \mathbf{u} = \sum_k f_k \mathbf{e}_k = \sum_k f_k^{eq} \mathbf{e}_k \ . \tag{2.50}$$

2.2.5   Nondimensionalization of the model

In any kind of CFD method it is customary to work with nondimensional variables, both for simplicity of the theoretical analysis and for practical advantages from the computational point of view. In order to nondimensionalize all variables, we will take as characteristic magnitudes the basic properties of the lattice: the distance between nodes in the grid δx and the period of a simulation time step δt. From those, it arises that a characteristic velocity scale of the system is $c = \delta x / \delta t$, as discussed above. Finally, the characteristic density will be defined by the mean density of the media ρ_0. Using those characteristic quantities, we express the new nondimensional variables (marked with hats) as follows:

$$\widehat{\delta x} = \widehat{\delta t} = \hat{c} = \hat{\rho}_0 = 1 \tag{2.51}$$

$$\hat{\mathbf{r}} = \frac{\mathbf{r}}{\delta x} \tag{2.52}$$

$$\hat{t} = \frac{t}{\delta t} \tag{2.53}$$

$$\hat{\rho} = \frac{\rho}{\rho_0} \tag{2.54}$$

$$\hat{f}_k = \frac{f_k}{\rho_0} \tag{2.55}$$

$$\hat{\mathbf{u}} = \mathbf{u}\frac{\delta t}{\delta x} = \frac{\mathbf{u}}{c} \tag{2.56}$$

$$\hat{c}_s = \frac{c_s}{c} = \frac{1}{\sqrt{3}} \tag{2.57}$$

$$\hat{\mathbf{a}} = \mathbf{a}\frac{\delta t^2}{\delta x} = \mathbf{a}\frac{\delta t}{c} \tag{2.58}$$

$$\hat{\nu} = \nu\frac{\delta t}{\delta x^2} = \frac{\nu}{c\,\delta x}. \tag{2.59}$$

Accordingly, equations (2.45) and (2.46) turn respectively into

$$\hat{f}_k(\mathbf{r} + \mathbf{e}_k\delta t, t + \delta t) = \left(1 - \frac{1}{\tau}\right)\hat{f}_k(\mathbf{r}, t) + \left[\frac{1}{\tau} + 3\hat{\mathbf{a}}\cdot(\hat{\mathbf{e}}_k - \hat{\mathbf{u}})\right]\hat{f}_k^{eq}(\mathbf{r}, t), \quad (2.60)$$

$$\hat{\nu} = \frac{2\tau - 1}{6}. \tag{2.61}$$

2.2.6   Boundary Conditions

A good specification of boundary conditions is a key point in any kind of numerical simulation model. The entire evolution of the system depends on the ability of those specified conditions to efficiently reproduce the circumstances in which the experiment takes place. There is a variety of different physical boundary conditions, and different ways to implement them in the simulations, according to the needs of each particular case. Here we will only address some of the most common and fundamental ones, which are also those required in our simulations. We can split the discussion in two main parts, referring respectively to wall conditions (and its boundary-layer effects), and inlet/oulet conditions (to drive a given flow).

No-slip wall conditions

The no-slip boundary condition that arises from the boundary-layer theory, tells us that the velocity of the fluid microlayer in contact with a solid wall has zero velocity relative to the wall. For us, this means that we could impose the velocity of the fluid on the lattice nodes adjacent to the walls, by simply reversing the direction of all the distribution functions at those nodes (what it is called the "on-wall bouncing back method"), as seen in Figure 2.6. However, for numerical
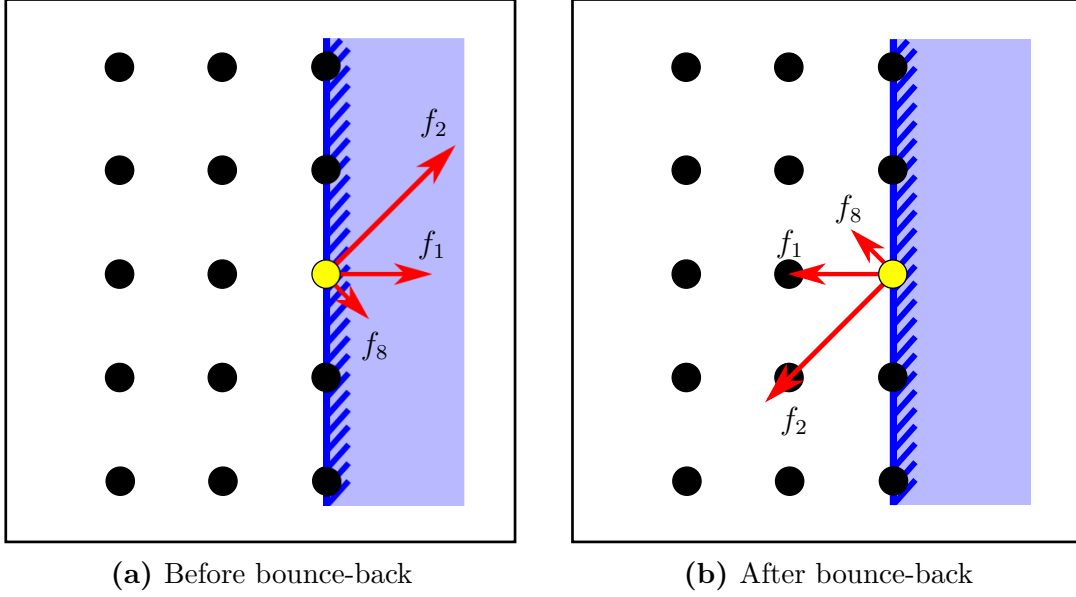
(a) Before bounce-back   **(b)** After bounce-back

Figure 2.6: On-wall boundary conditions for no-slip walls

reasons, this method only provides first order accuracy in the results. Alternatively, we can get second order accuracy by simply displacing the bouncing back line half node ($\frac{\delta x}{2}$) away from the physical wall [Succi (2001)].

This solution is the so called no-slip boundary conditions for mid-way walls (Figure 2.7). With this method we are designing our grid in a way that walls are always located at the exact middle distance between 2 nodes. This implies that one node is at the liquid part of the simulation (the one we want to study), while the other represents a virtual node at the solid part. Then we implement the bouncing back method in the solid nodes as follows:

$$f^*_{-k}(\mathbf{r} - \mathbf{e}_k \delta t, t) = f_k(\mathbf{r}, t), \tag{2.62}$$

$$\mathbf{e}_{-k} \equiv -\mathbf{e}_k, \tag{2.63}$$

where $\mathbf{r}$ is the position of each wall node, subscript k stands for any distribution that has been streamed into the solid wall node, and superscript $*$ refers to the value of f after the bouncing back.

This method gives very good agreement between the position where we placed the walls in our design and the effective position resulting from the numerical computations. For further improvements in the wall boundary conditions, the reader can refer, for instance, to [Verschaeve (2009)].

By adding all the changes in the distribution functions that the wall nodes have introduced into the flow, we could be able to calculate the frictional effect of the walls and the total force $\mathbf{F_w}$ exerted by the walls into the fluid. For each f_k

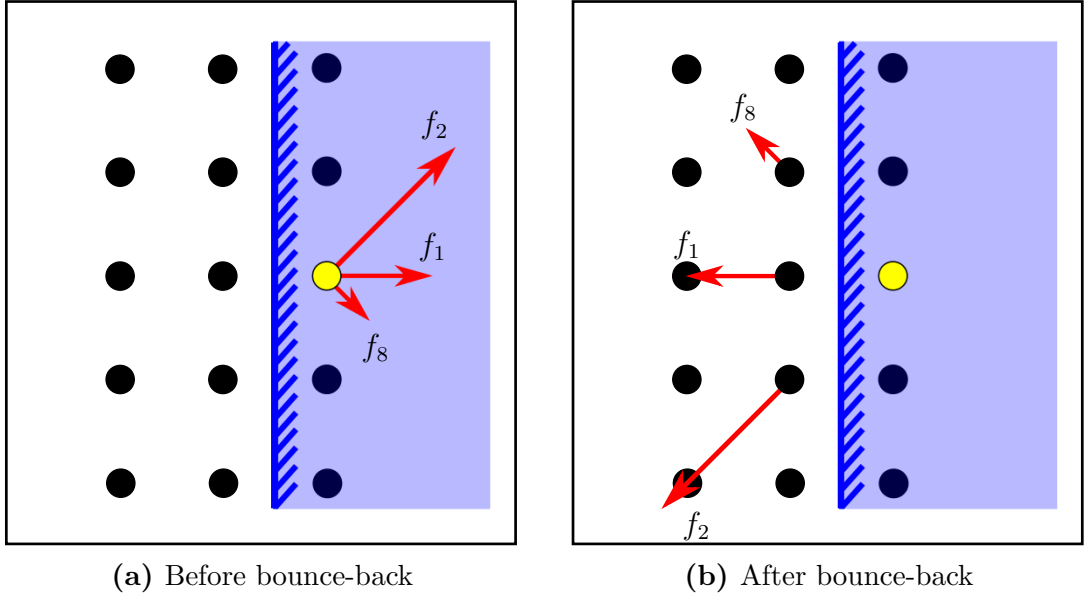**(a)** Before bounce-back   **(b)** After bounce-back

Figure 2.7: Mid-way wall boundary conditions for no-slip walls

that has been streamed to a wall node, the collision has changed the distribution as:

$$f_k \mathbf{e}_k \qquad \rightarrow \qquad f_k \mathbf{e}_{-k} = -f_k \mathbf{e}_k$$

which implies that the impulse dI caused by every piece of wall reads

$$dI = (f_{\text{after}} - f_{\text{before}}) = -2f_k. \tag{2.64}$$

Extending this analysis to all wall nodes and adding their contributions, we obtain an expression for the constant force $\mathbf{F_w}$ needed to cause this total momentum transfer to the flow in the period of one time step δt of the form

$$\mathbf{F_w} = -\frac{1}{\delta t} \sum_{\text{walls}} (2f_k \mathbf{e}_k). \tag{2.65}$$

Inlet/Outlet conditions

There are mainly two simple ways of implementing a constant flow in a Lattice-Boltzmann simulation of a channel: imposing an inlet velocity or using periodic conditions. The first one is the method of the constant velocity inlet [Zou and He (1997); Hecht and Harting (2008); Latt et al. (2008)]. It consists of setting a layer where we impose the constant flow entering inside our lattice. We enforce the velocity of the fluid at that layer, by specifying the probability distribution function at each of those nodes, at each time step. The main problem of this method, when dealing with turbulent flows, is that any velocity distribution imposed on
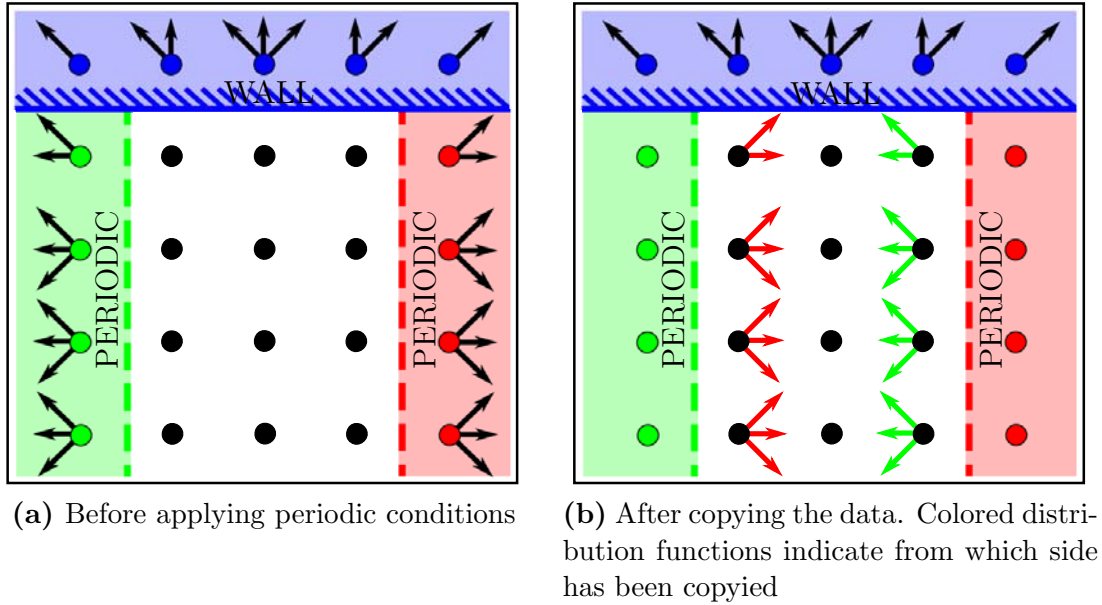
(a) Before applying periodic conditions

(b) After copying the data. Colored distribution functions indicate from which side has been copied

Figure 2.8: Periodic conditions. Colored nodes represent virtual nodes: in blue, solid nodes; in red and green, periodic conditions.

the inlet will be highly unstable. This is because one deals with a layer with many fixed parameters, while the flow tends to be highly mutable. Strong turbulence propagates its effects closer and closer to the inlet, and this process enhances the differences between neighboring nodes, which ultimately causes the simulation to diverge. Furthermore, even if we could avoid this instability, it would take the flow a long distance to evolve from the constant, laminar inlet, up to the fully turbulent flow. That requires very large lattices in order to find the correct steady turbulence sufficiently far from the inlet.

The second method is the one that we will explain in detail in this section. This is even simpler to implement and avoids the major problems of the inlet velocity. It consists of using periodic conditions, such that the flow (and its associated distribution functions) that exits the end of the channel is exactly the same that is being fed from the opposite side (Figure 2.8). This avoids the generation of discontinuities at the edges and also minimizes the longitudinal finite size effects, resembling more the case of an infinite system. As long as correlations in the longitudinal direction of the channel die out in a scale that is sufficiently smaller than the channel length, periodic boundary conditions will accurately reproduce the conditions of a steady infinite flow. The drawback is that one cannot specify the incoming flow with full freedom, in particular in order to study the transient evolution of specific initial conditions.

An important point must still be addressed to keep a stationary flow. If we just implement the periodic boundary conditions by matching the fields in the two

extrema of the channel, viscous dissipation will progressively eliminate the flow. Clearly, in order to sustain a constant flow one must apply an external force that counterbalances the friction force from the lateral walls. The solution is as easy as imposing a force term at each fluid element, as explicitly written in the rightmost term of equation (2.45). That force term represents the overall pressure gradient imposed on the system by fixing the total pressure drop between the ends of the channel.

To elucidate the value of the force term required for a certain flow, we have used two methods that have been proven appropriate. The use of one or the other depends on the precise specification of the quantities that are imposed to be constant by construction, and those that may fluctuate around an average value. It is worth remarking that, due to the inherent instability and variability of the turbulent flow, the total friction force from the walls in real experiments is likely to fluctuate in time. Then, one option aims at achieving a constant flux by imposing a fluctuating external force. That means that, in this case, the force term $\mathbf{a}$ applied to the lattice sites will change at every time step. In this case we should exactly supply the loss of momentum of the fluid due to the friction with the walls $\mathbf{F_w}$, as seen in Equation (2.65). The idea would be to distribute the force that opposes friction $(-F_w)$ among all nodes in the lattice N_{nodes} as

$$\mathbf{a} = \frac{-F_w}{\rho_0 \, N_{\mathrm{nodes}}} \hat{\imath} \, , \tag{2.66}$$

where $\hat{\imath}$ is the unitary vector in the direction of the flow, and F_w stands for the component of $\mathbf{F_w}$ in the same direction.

The alternative strategy is to admit a total flux that is not strictly constant but fluctuates around a fixed mean value, while the total external force remains strictly constant. The two conditions (constant flux or constant force) correspond to similar physical conditions, and are equivalent for sufficiently long channels.

The way to implement the case of constant force involves imposing a certain frictional Reynolds number Re_*

$$Re_* = \frac{u_* L}{\nu} \, , \tag{2.67}$$

where L is a characteristic size of the flow (like the channel width) and u_* is the mean shear velocity, which is related to the mean wall stress τ_w as

$$u_* = \sqrt{\frac{\tau_w}{\rho}} \, . \tag{2.68}$$

The expression for the external driving force reads

$$\mathbf{F} = \rho\mathbf{a} = -\frac{dP}{dx}\hat{\boldsymbol{\imath}}\,, \tag{2.69}$$

and, as explained by Pattison et al. (2009), we can relate the mean shear velocity to the pressure gradient by means of the force balance

$$\rho u_*^2 = -\frac{L}{4}\frac{dP}{dx}\,. \tag{2.70}$$

Therefore, from Equations (2.69) and (2.70), we obtain

$$\mathbf{a} = \frac{4u_*^2}{L}\hat{\boldsymbol{\imath}} = \frac{4Re_*^2\nu^2}{L^3}\hat{\boldsymbol{\imath}}\,. \tag{2.71}$$

Finally, we can express this result in its nondimensionalized form by using Equation (2.61). We also use the correspondence $L = N_y\delta y$, where N_y stands for the number of lattice nodes along the length L,

$$\hat{\mathbf{a}} = \frac{Re_*^2(2\tau - 1)^2}{9N_y^3}\hat{\boldsymbol{\imath}}\,. \tag{2.72}$$

2.2.7   Initial Conditions

When choosing the initial conditions, it is convenient to take them as close as possible to the stationary state, to minimize the computation time for the relaxation of the initial transient. The simplest case is to impose a constant, homogeneous velocity, corresponding to the mean velocity of the final flow. This possibility avoids already the need to accelerate/decelerate the flow, which would introduce (unphysical) transients of the algorithm. A simple improvement is to impose the inhomogeneous mean profile for the corresponding geometry, which is usually known to a good approximation. Since smooth profiles may be (nearly) metastable, it is convenient to introduce random, symmetry breaking perturbations to speed up the growth of the instabilities leading to turbulence. However, one must be very cautious to introduce physically consistent random fluctuations, that is, such that they satisfy the boundary conditions and in particular that preserve the incompressibility condition.

2.2.8   Sub-Grid Scale (SGS) filtering.

The main computational difficulty of highly turbulent flows is the need to account simultaneously for a broad range of scales, from eddies of the system size, to the

small ones fixed by the scale of viscous dissipation. Solving such flows in three-dimensional systems is in the limit of the current supercomputing power. As an illustrative example, let us consider the experiment that we will study in this thesis using Lattice-Boltzmann methods, a square-section channel of 10 cm wide and 80 cm long, where we have a flow with a Reynolds number of around $Re = 10000$. The Kolmogorov scale λ_k is the magnitude that specifies the size of the smallest scale of turbulence, and is given by

$$\lambda_k = LRe^{-3/4} \ . \tag{2.73}$$

In our case study we have $\lambda_k = 0.1$ mm. That means that, in principle, in order to fully resolve spatially all details of this turbulent flow, we should have a grid of at least 1000x1000x8000 nodes, that is, 8×10^9 nodes, a number that is clearly out of question. In fact, with the speed of the computers that we have used, that would require 220 years of calculation, or equivalently, 1000 computers calculating non-stop for 82 days, in order to simulate only one second of the experiment.

One must obviously devise alternative strategies to circumvent this problem. An important point is to realize that the dissipation only occurs at the smallest scales, while the energy is transferred from larger to smaller scales without significant dissipation. This implies that the effect of the smallest scales is mainly to dissipate the kinetic energy injected at larger scales, but they do not have a significant impact on the dynamics at those larger scales. Exploiting this observation, what one can do is to add some kind of function that roughly dissipates the energy of all the scales smaller than the lattice size in the simulation. In this way we prevent the emergence of instabilities produced by the unresolved fluctuations of the flow at those smaller scales. That is what we know as sub-grid scale filtering.

Smagorinsky Coefficient

The most common method of SGS filtering is the so-called Smagorinsky Coefficient, that was presented by Smagorinsky (1963) and implemented in the LBGK model by Hou et al. (1994). This method is based on the calculation of the local effective viscosity that would dissipate the sub-grid effects generated at each local point. This means that we have a different effective viscosity at each node of the lattice, and at each time step, corresponding to the sum of the real physical viscosity ν_0 of the fluid plus the so-called eddy viscosity ν_t

$$\nu_t = C_s \Delta^2 \bar{S} \ , \tag{2.74}$$

$$\nu_{\text{total}} = \nu_0 + \nu_t = \nu_0 + C_s \Delta^2 \bar{S} \ , \tag{2.75}$$

where $C_s = 0.0144$ [Pattison et al. (2009)] is the Smagorinsky constant, which must be adjusted empirically, Δ is the scale of the minimum effects that we are able to numerically reproduce ($\Delta = \delta x$) and $S_{a,b}$ is the large scale strain tensor of the incompressible fluid, defined by

$$S_{a,b} = \frac{1}{2}\left(\frac{\partial u_a}{\partial x_b} + \frac{\partial u_b}{\partial x_a}\right) \qquad (2.76)$$

$$\bar{S} = \sqrt{\left(\sum_{a,b} 2S_{a,b}S_{a,b}\right)} . \qquad (2.77)$$

We can calculate this tensor from the non-equilibrium part of the distribution functions $f_i^{neq} = (f_i - f_i^{eq})$ by means of the expression

$$S_{a,b} = \sum_i (f_i^{neq})(e_{ia}e_{ib} - c_s^2\delta_{a,b}) , \qquad (2.78)$$

where $\delta_{a,b}$ is the Kroeneker delta. For a further improved version of the model, applied to the Generalized Lattice Boltzmann model with multiple relaxation times, readers can address to [Jafari and Rahnama (2011)].

An important issue is that the anisotropic turbulence near the walls tends to decrease its effective scales as we get closer to the them [van Driest (1956)]. Therefore, taking a constant value for Δ when calculating the eddy viscosity may produce an excessive damping of the flow in that critical area of the boundary conditions [Premnath et al. (2009)]. The most popular way of solving this is by using the Van Driest damping function, which converts Δ in a function that decreases at the proximities of the walls [Pattison et al. (2009)].

Although we have dissipated the turbulent kinetic energy of the sub-grid scales by means of the Smagorinsky coefficient method, there are still additional numerical instabilities that originate in numerical noise which may introduce different artifacts of the simulation and eventually become very destructive. The method proposed in order to eliminate those instabilities consists of filtering the small numeric discrepancies between first neighbor nodes. This smoothing procedure must we done with care in order to preserve mass and momentum conservation. We propose a smoothing of the form

$$f_k^{*(0)} = f_k^{(0)} + \delta\left(f_k^{(1)} + f_k^{(2)} + f_k^{(3)} + ... + f_k^{(n)} - nf_k^{(0)}\right) , \qquad (2.79)$$

where superscript (0) refers to a central node, and the other superscripts (1) to (n), correspond to its first neighbor nodes. For a node in the bulk in a 3D space $n = 6$, while for a node in contact with a wall, $n = 5$. The subscript k indicates that
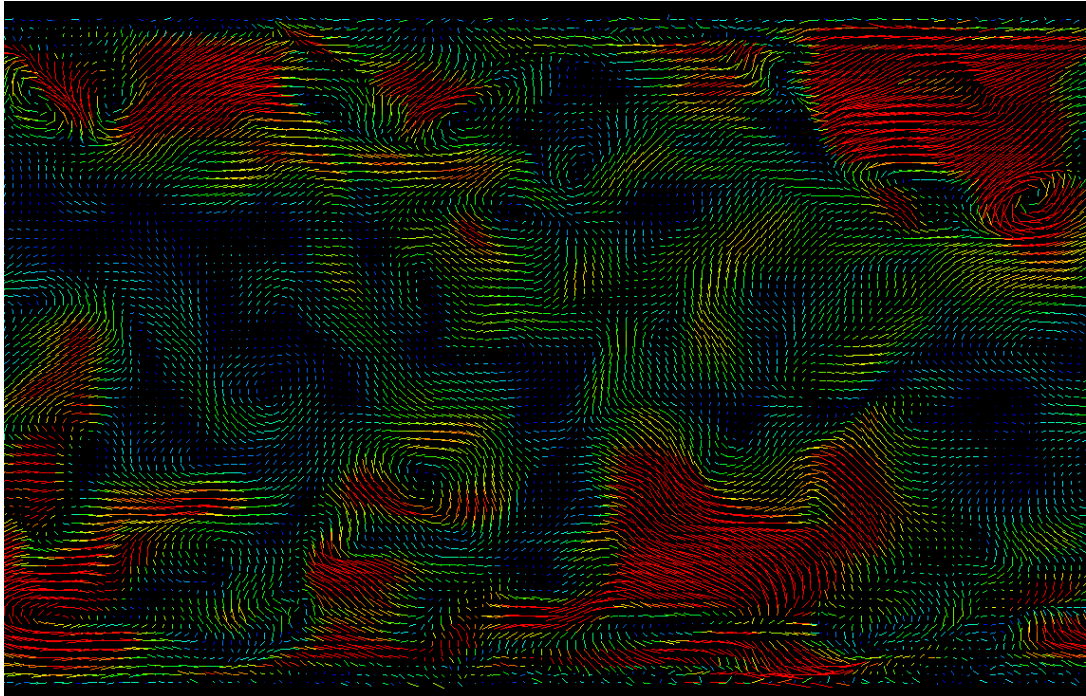
(a) Adequate solution ($\delta = 10^{-4}$)
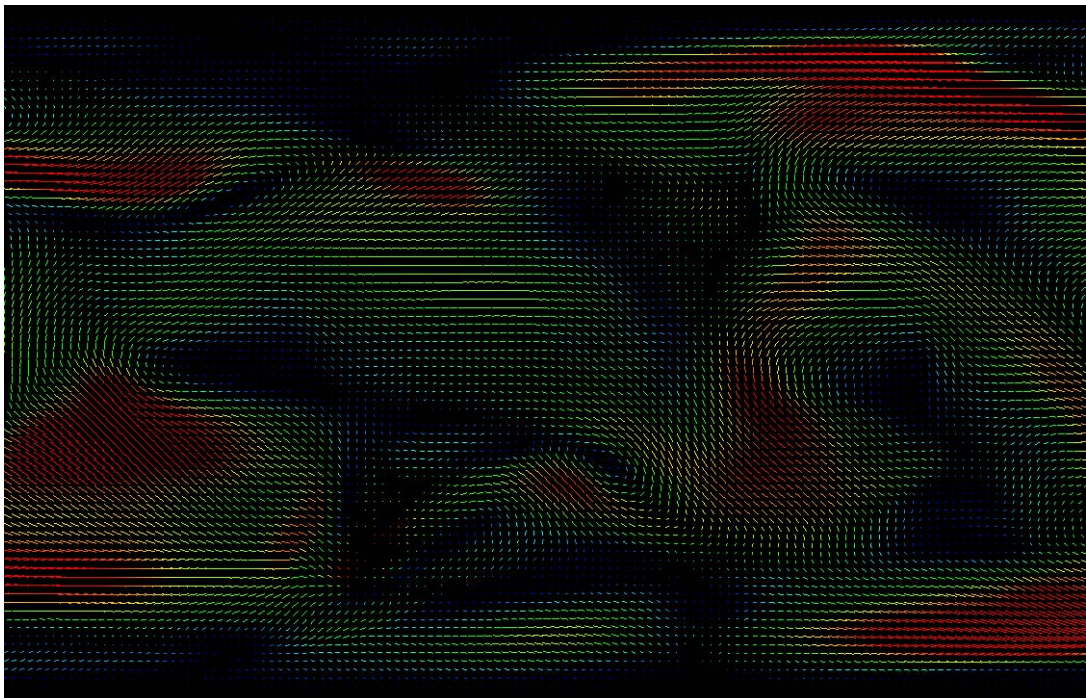
(b) Excess of filtering ($\delta = 10^{-3}$)

Figure 2.9: Effect of the filtering on the central slice of a 3D simulation of a channel with $Re = 10000$. Lines correspond to the fluctuating component of the velocity

(a) Numerical instabilities in absence of filtering ($\delta = 0$)
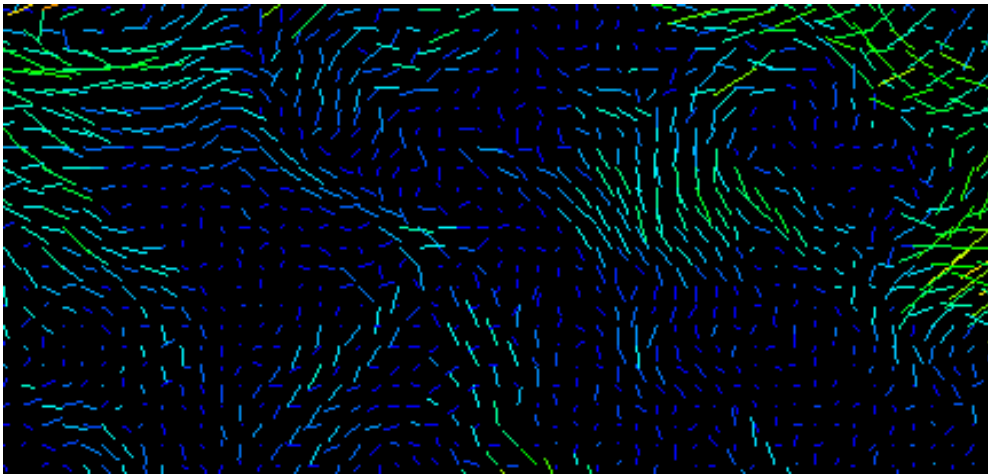

(b) Adequate solution ($\delta = 10^{-4}$)
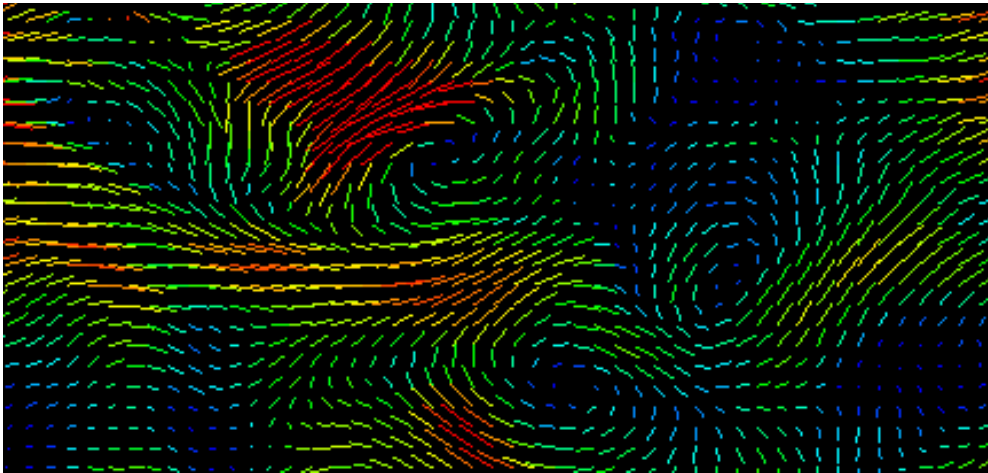

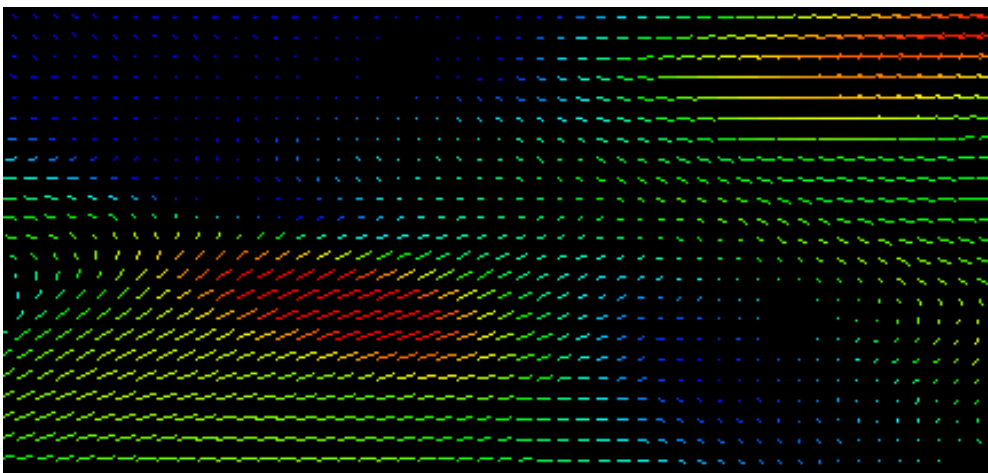**(c)** Excess of filtering ($\delta = 10^{-3}$)

Figure 2.10: Effect of the filtering on the central slice of a 3D simulation of a channel with $Re = 10000$. Lines correspond to the fluctuating component of the velocity
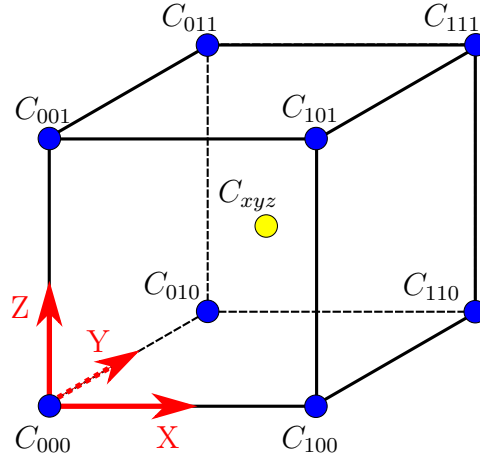
Figure 2.11: Configuration of eight nodes where a certain magnitude C is known. The yellow node stands for the point where we want to know the value of C_{xyz}. The three dimensions have been normalized.

this expression should be applied to all the distribution functions (corresponding to each of the possible velocities) at the present node. Lastly, $\delta << 1$ is a small free parameter which controls the degree of filtering that we are applying. If we take it too small, noise instabilities will set in, as in the case shown in Figure 2.10a. On the other hand, taking δ too big, eliminates the small scale structures, suppressing the level of turbulence (Figure 2.9b) even to point of producing a laminar flow. The adequate value of this filtering parameter must be explored for each particular situation and in general it will depend on the time step, as well as on the node spacing.

2.2.9 Passive Tracers

For the analysis of the experiments in the following section it will be useful to characterize the turbulence with introducing passive tracers, point-like particles that do not affect the flow and follow their streamlines. It is important to notice that the position of these tracers must not be restricted to the discretization of the lattice. The position of a tracer $\mathbf{r_p}$ will be determined by the expression

$$\mathbf{r_p}(t + \delta t) = \mathbf{r_p}(t) + \mathbf{u_f}(\mathbf{r_p}, t)\delta t \ . \tag{2.80}$$

Here, $\mathbf{u_f}$ stands for the velocity of the flow at the position of the tracer at time t, which must be interpolated from the discrete values in the grid, in order to get a description in continuous space. We will use the trilinear interpolation scheme between eight points, which are the nearest eight nodes surrounding the tracer.

In Figure 2.11 we plot the eight lattice nodes that define the interpolation for

a tridimensional configuration. Assuming that we know the value of a certain magnitude C at those points and we want to infer the value C_{xyz} of C at a certain point (x, y, z) between them, we must first interpolate in each dimension

$$\begin{cases} C_{00z} = (1 - z)C_{000} + (z)C_{001} \\ C_{10z} = (1 - z)C_{100} + (z)C_{101} \\ C_{01z} = (1 - z)C_{010} + (z)C_{011} \\ C_{11z} = (1 - z)C_{110} + (z)C_{111} \end{cases} \tag{2.81}$$

$$\begin{cases} C_{0yz} = (1 - y)C_{00z} + (y)C_{01z} \\ C_{1yz} = (1 - y)C_{10z} + (y)C_{11z} \end{cases} \tag{2.82}$$

$$C_{xyz} = (1 - x)C_{0yz} + (x)C_{1yz} \tag{2.83}$$

where the three coordinates have been normalized by lattice spacing δx, as seen in the figure. Then it follows that

$$\begin{aligned} C_{xyz} = \quad & (1-x)(1-y)(1-z)C_{000} \quad + \quad (1-x)(1-y)zC_{001} \quad + \\ & + \quad (1-x)y(1-z)C_{010} \quad + \quad (1-x)yzC_{011} \quad + \\ & + \quad x(1-y)(1-z)C_{100} \quad + \quad x(1-y)zC_{101} \quad + \\ & + \quad xy(1-z)C_{110} \quad + \quad xyzC_{111} \quad . \end{aligned} \tag{2.84}$$

In our case, C will correspond to each of the three components of the velocity (u_x, u_y and u_z).

2.2.10   Further remarks

About D3Q19 and D3Q27

Despite the claims of some authors [d'Humieres et al. (2002)] argue that the D3Q19 and D3Q27 schemes are often more stable than the one used in our simulations (D3Q15), our experience contradict this claims for our case. For some reason that is not fully understood, the two other schemes introduce some resonant instabilities in our simulations, which end up with divergent behavior. On the contrary, our experience is that the D3Q15 is most stable and suitable for our problem.

Chapter 3

Turbulent bubble jets

3.1   Introduction

Efficient control of bubble formation and management in microgravity environments is an important aspect for multiple applications in space technology. From a fundamental point of view, the statistical physics of bubbly turbulent flows in microgravity is also largely unknown, due precisely to the difficulty to achieve good experimental control of the experimental conditions for bubbles. One of the limiting experimental factors is the control of bubble sizes. This is important both for applications, to control the total gas-liquid contact area, and for fundamental characterization and understanding of the interaction of bubbles and turbulence.

Recently a gravity insensitive method has been proposed by Carrera et al. (2008) to generate a train of equally distant bubbles (slug flow) of uniform bubble size. This regime is achieved by means of a capillary T-junction, where constant flows of water and air are respectively injected from the transversal capillary tubes. In this way, bubbles are detached by means of capillary and drag forces, obtaining a bubble generation method insensitive to gravity. The size of the resulting bubbles is roughly the diameter of the capillary tubes (i.e. typically around 1.5mm) although it can be slightly modified. A theory for bubble formation in this setup was already discussed in detail by Carrera et al. (2008) and the experimental characterization of the bubble formation method has been completed in normal gravity by Arias et al. (2009).

Injecting this controlled slug-flow into a quiescent cavity, Carrera et al. (2008) obtained a nearly monodisperse dispersion of bubble suspensions. This high degree of monodispersivity of the bubbles is also well understood within the theoretical framework of their work, stating that when bubbles are injected into the quiescent cavity, the monodispersivity will be maintained to the extent that bubble coalescence is avoided.

Our aim here is to discuss and model the behavior of such bubble jets in microgravity. Carrera et al. (2008) also found that the mean flow associated to such turbulent jets is essentially unaffected by the presence of bubbles, except by a renormalization of the total momentum injected. Therefore, regarding the mean flow, bubbles could be considered as passive tracers of the flow. It was also pointed out, however, that bubbles may in general affect the degree of turbulence, that is the fluctuating component of the velocity, since they cannot be considered as point-like and sufficiently dilute throughout the whole jet, in particular near the inlet of the cavity.

In the present chapter[1] we will study the spatial dispersion and the velocity fluctuations of bubbles within a turbulent jet. Since dispersion depends on the fluctuating components of the turbulent flow, a basic question will be to what extent the picture of bubbles as passive tracers, well established for the mean flow, could also be useful for the characterization of the fluctuating components. As we will show, some statistical aspects of the dispersion process, mainly the resulting spatial distribution of bubble concentration, can be accounted for to a large extent by using a model of passive bubbles. To this aim we will construct a model for bubble dynamics in which the instantaneous bubble velocity is calculated as the addition of the local mean flow plus a stochastic term depending on the local degree of turbulence. For this picture the use of effective turbulence models such as the k-ε model (seen on chapter 2.1.2), which yields an approximate closure of the averaged turbulence, appears as specially suitable. The treatment of the spreading of a passive scalar within a k-ε model has been studied in detail in the literature. In the present case the k-ε model will provide both the mean flow and local quantities representing the small scale diffusivity associated to the turbulence. Our results show that integration of the model, both for individual trajectories and for the concentration field of bubbles, compares well with experiments.

The understanding of the physics of the bubble jets created by this method is a first step towards the aim of producing controlled spatially uniform, monodisperse bubble suspensions in turbulent pipe flows, in microgravity. These will be created and studied experimentally by combination of four of such injectors with externally imposed flows in chapter 4. The capability of preparation of such suspensions opens the door to a large variety of possibilities of interest for practical application but also for a deeper understanding of the two-way interaction between bubbles and turbulence in the absence of buoyancy.

---

[1]Part of this work was published on the International Journal of Transport Phenomena [Bitlloch et al. (2011)].

3.2   General remarks on turbulence

3.2.1   Turbulence characterization

In order to describe the degree of turbulence in a given flow, one must take into account the Reynolds number (Re) which is a non-dimensional number that establishes the ratio between inertial and viscous forces in the fluid. For a flow with a characteristic velocity U_c, size L_c and kinematic viscosity ν, it is usually expressed in the form:

$$Re = \frac{L_c U_c}{\nu} \tag{3.1}$$

Large Reynolds numbers implies a higher predominance of the inertial forces over the viscous effects, which translates into a much more unstable and complex structure of the flow. This is due to the appearance of turbulence, which can be pictured as the superposition of eddies and velocity fluctuations with characteristic length and time scales comprising broad ranges, of several orders of magnitude apart in the case of fully developed turbulence for large values of Re. On the other hand, for small Re, viscous dissipation dominates and stabilizes the dynamics, typically producing laminar flow.

In order to study the relevant magnitudes governing turbulence as well as the properties of its constitutive eddies of various sizes, we introduce the Reynolds number Re_λ for turbulent eddies

$$Re_\lambda \sim \frac{\lambda \, v_\lambda}{\nu} \, , \tag{3.2}$$

with λ being the size of the correspondent eddy, and v_λ its characteristic velocity (accounted as the order of magnitude of the relative velocities between fluid elements in the eddy, not its absolute velocities). In this frame, largest eddies create the fundamental scale of turbulence (i.e. its main structure) and are determined by the shape and dimensions of the receptacle in which the flow is streaming in. Smaller eddies, on the other hand, contain a much smaller amount of kinetic energy and only produce a fine detailed pattern superposed on the fundamental structure created by the larger ones.

Gore and Crowe (1989) found that the size λ_{Max} of the most energetic eddies in the case of a pipe flow is 0.1 times the diameter of the tube d_{pipe}, i.e.

$$\lambda_{\text{Max, pipe}} \simeq 0.1 \, d_{\text{pipe}} \, , \tag{3.3}$$

while in the case of a circular jet (as the ones studied in the present chapter) its

size is 0.039 times the distance to the injection point x, i.e.

$$\lambda_{\text{Max, jet}} \simeq 0.039\,x \tag{3.4}$$

These large scales with $\lambda \sim L_c$ are known as the energy range, because they are the ones containing the major proportion of energy of the turbulence. Also, at those scales we have that $Re_\lambda \gg 1$, therefore the inertial forces are predominant over the viscous effects. Hence, viscosity has a negligible effect into the fluid at this scale and there is no energy dissipation. Richardson (1922) observed that the kinetic energy of the large eddies passes to the smaller ones practically without any dissipation, creating a continuous energy flux from the big to the small scales, until the turbulent kinetic energy is dissipated into heat at the smallest eddies. That dissipation happens when the viscous effects gain significance in relation to the inertial terms, namely when $Re_\lambda \sim 1$ and thus $\lambda_k v_k \sim \nu$. These are known as the Kolmogorov scales of length (λ_k) and velocity (v_k), which determine the minimum scale of turbulence (where its energy is dissipated). With its corresponding time scale $\tau_k = \lambda_k/v_k$, the Kolmogorov scales are defined [Brennen (2005)] as

$$
\begin{cases}
\lambda_k = \left(\dfrac{\nu^3}{\varepsilon}\right)^{1/4} \\[2em]
\tau_k = \sqrt{\dfrac{\nu}{\varepsilon}} \\[2em]
v_k = (\varepsilon\nu)^{1/4}
\end{cases}
\tag{3.5}
$$

These expressions arise from simple dimensional analysis, by knowing that the only magnitudes affecting the smallest eddies are the rate of energy dissipation (ε), the dynamic (μ) or kinematic (ν) viscosity (which control the dissipation), and the fluid density (ρ_l), so its scale should only depend on these parameters. Equations in (3.5) are then the only dimensionally correct combination of ε and ν, and they describe the order of magnitude of the smallest scale of turbulence[2]. Strong viscous effects at this scale makes the fluid flow to be essentially laminar although still time-dependent, being the smallest eddies actually found at a scale 10-20 times larger than the Kolmogorov length [Jiménez (1997)], i.e.

$$\lambda_{\text{min}} \sim 10\,\lambda_k \tag{3.6}$$

---

[2]Note that despite the equations in (3.5) only describe the order of magnitude of the minimum scale of turbulence, they are written as an equality. That only means that these expressions are defined exactly as the Kolmogorov scales, not that they were exactly the parameters of the smallest eddies.

At even smaller scales (i.e., $\lambda < \lambda_k$) we reach the viscous range, in which the flow is fully laminar and all the fluctuations are damped.

Even though the energy is dissipated due to the viscosity at the smallest scales, we can determine the mean dissipation rate ε of the turbulent kinetic energy by means of the quantities which characterize the large eddies, because it is in that scale that the energy is transferred into the turbulence from the mean flow [Landau and Lifshitz (1987); Brennen (2005)]. With simple dimensional analysis, knowing that the energy ε which generates the largest eddies should only depend on the characteristic scales of the mean flow (i.e. U_c, L_c and ρ_l) and that the viscosity does not have any impact at this scale, we reach the expression

$$\varepsilon \sim \frac{U_c^3}{L_c} \ . \tag{3.7}$$

In view of that relation we can rewrite the equations in (3.5) in a more manageable form:

$$\begin{cases} \lambda_k \sim L_c \, Re^{-3/4} \\ \\ \tau_k \sim \dfrac{L_c}{U_c} Re^{-1/2} \ = \ T_c \, Re^{-1/2} \\ \\ v_k \sim U_c \, Re^{-1/4} \end{cases} \tag{3.8}$$

One last dimensional analysis that results very handful is to find the characteristic velocity associated to any scale of turbulence. This follows from the work of Kolmogorov (1941) and Obukhov (1941) on the scaling laws for local turbulence. To make this analysis possible we must focus on the inertial range (i.e. $\lambda \gg \lambda_k$), in order to be able to neglect the viscosity effects, restricted to scales smaller than the mean flow properties (i.e. $L_c \gg \lambda \gg \lambda_k$). In this range and far away from boundary layers of our system, we find ourselves in the frame of fully developed turbulence, in which the structure of turbulence and its velocity fluctuations (relative to the elements of fluid in the same scale) exhibit an homogeneous and isotropic behavior. In this conditions, the characteristic velocity v_λ of a given scale of turbulence of size λ, should only depend on the size λ itself, the energy rate ε transferred between scales, and the density of the fluid ρ_l. The only combination possible of these parameters that is dimensionally correct is:

$$v_\lambda \propto (\varepsilon \lambda)^{1/3} \ . \tag{3.9}$$

Equation (3.9) is the Kolmogorov and Obukhov law, which states that the

velocity variation over a small distance is proportional to the cube root of the distance [Landau and Lifshitz (1987)]. Knowing that the variation of the mean velocity of a flow over a small distance is small compared to its velocity fluctuations, the first one can be neglected and so v_λ can also be seen as the typical velocity of the eddies of size λ. Taking advantage of equation (3.7), we can turn expression (3.9) into

$$v_\lambda \propto U_c \left(\frac{\lambda}{L_c} \right)^{1/3} \,, \tag{3.10}$$

which is often known as the self-similarity relation for fully developed turbulence.

3.2.2   Interaction of bubbles with turbulence

The description of free-slip boundary conditions[3] for fluid spheres in an environment free from surface-active contaminants, was introduced for the first time by Hadamard (1911) and Rybczynski (1911). From their work it arises that the terminal rising velocity W_f of a fluid sphere of diameter d_B in a slowly moving fluid follows the expression [R.Clift et al. (1978)]:

$$W_f = \frac{d_B^2 \, g \, (\rho_f - \rho_g)}{6\mu_f} \left(\frac{\mu_f + \mu_g}{2\mu_f + 3\mu_g} \right) \,. \tag{3.11}$$

In the case of a bubble [Mazzitelli et al. (2003); Brennen (2005)], where $\rho_f \gg \rho_g$ and $\mu_f \gg \mu_g$, this reduces to

$$W_B = 2g\tau_B = \frac{d_B^2 \, g}{12\nu_f} \,, \tag{3.12}$$

$$\tau_B = \frac{d_B^2}{24\nu_f} \,, \tag{3.13}$$

where W_B and τ_B are respectively the terminal rising velocity in still fluid and the bubble relaxation time. This response time indicates how fast is the bubble adapting to the fluctuations of the flow. In the absence of gravity, if $\tau_B > \tau_\lambda$ it indicates that the bubble cannot follow all the fluctuations on the scale λ. This may lead to an increase of dissipation, tending to attenuate turbulence, but in some case it can have the opposite effect through the formation of wakes [Balachandar and Eaton (2010)]. On the opposite scenario, if $\tau_B \ll \tau_k$, the bubble

---

[3]Imposing zero normal velocity and zero shear stress on the bubble interface so that the fluid can slip on it

respond quickly to any perturbation on turbulence and has a lesser impact upon it.

As found by R.Clift et al. (1978) and many other authors, special precautions must be taken in order to prevent the accumulation of surfactants in distilled water. Impurities rapidly settle on the interface of small bubbles, producing an effectively rigid particle response. Thus the No-Slip boundary description of a spherical particle (or bubble) should be applied instead. This solution comes from the work of Stokes (1851), and determines the terminal velocity W_p of a particle of mass m_p in the form:

$$W_p = \frac{d_P^2 \, g}{18 \nu_f} \left(1 - \frac{m_p}{m_f} \right) \ , \tag{3.14}$$

where m_f is the mass of fluid displaced by the particle volume. The corresponding response time τ_p takes the form [Maxey et al. (1996); Brennen (2005)]:

$$\tau_p = \frac{m_c}{3\pi\mu \, d_p} \ , \tag{3.15}$$

where m_c is the effective mass of the particle, corresponding to $m_c = m_p$ for the case of a heavy particle and $m_c = \frac{m_f}{2}$ (i.e., half the mass of the displaced fluid) for the case of a bubble. From that, one directly obtains, for the case of a bubble,

$$\tau_B = \frac{d_B^2}{36 \nu_f} \ , \tag{3.16}$$

which is 1.5 times smaller than the response time for the case of a free-slip interface in equation (3.13). This is because of the increase on the drag force acting on a bubble under no-slip conditions, due to the different interface interactions.

3.3 Experimental description

In order to generate bubbles in microgravity conditions, we use a capillary T-junction, formed by capillary tubes of 1.5 mm diameter. By simultaneously injecting constant flows of water and air through the transversally connected inlets of the T-junction, we generate an air-water slug flow of prescribed bubble size and uniform separation between bubbles (Fig. 3.1). In these conditions, buoyancy forces are negligible in front of the strong capillary and drag forces, being these last the responsible for the detachment of bubbles. Consistently, the T-junction system is insensitive to gravity, producing the same outcome both in microgravity and in normal gravity conditions. The size of the bubbles generated with this procedure is similar to the diameter of the capillary tubes, although it can be slightly tuned. Altogether with the bubble formation frequency and the distance between
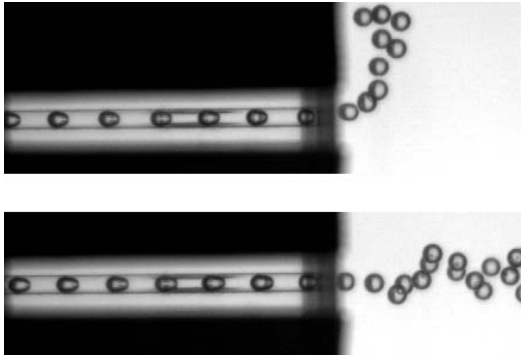
Figure 3.1: Typical slug-flow injected into the experimental cell, with a capillary diameter $d_T = 1.5$ mm. *(Above)*: In normal gravity conditions; *(Below)*: In microgravity.
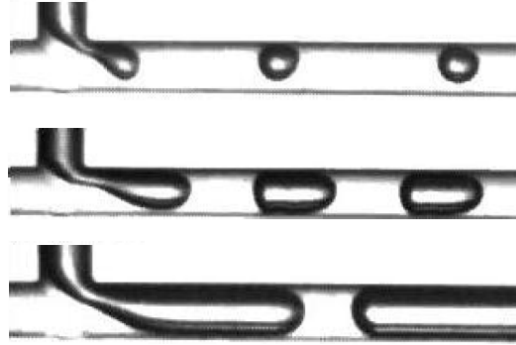

Figure 3.2: Behaviour of a T-junction of capillary diameter $d_T = 1$ mm for different injection parameters. Picture courtesy of Arias (2011)

them, their size can also be modified by adjusting the liquid and gas flows injected into the T-junction, as can be seen in Fig.3.2. Nevertheless it is worth remarking that this T-junction arrangement only produces a clean and well-behaved slug-flow (as it is needed for our studies) for a relatively reduced range of parameters, preventing large modifications in the outgoing bubble size or frequency. A full description of all the flow regimes generated in a T-junction of 1 mm diameter has been exhaustively studied by Arias (2011).

A series of microgravity experiments were conducted a few years ago by Carrera et al. (2008) in the drop tower of ZARM in Bremen, in which this bubble generator was used for the first time for microgravity purposes. They created and injected a uniform slug flow into a quiescent cubic cavity of 100x100x100 mm³, as sketched in Fig. 3.3. In this figure we also show the structure of the mean velocity field obtained from a numerical CFD calculation in the case of a single-phase flow of $Re = 690$ (defined for the injector), by using a realizable k-ε model in the frame of a finite volumes method as described in chapter 2.1.

In absence of buoyancy effects, the injection of the slug flow results in the formation of a turbulent jet which crosses the cavity, and in which bubbles are dispersed in a roughly conical shape (Fig. 3.4). In their paper, Carrera et al. (2008) showed how the experimental mean velocity of bubbles (calculated at different points along the axis and at the boundaries of the cone) fits the analytical solution of a turbulent liquid jet without any dispersed phase. This results imply that the presence of bubbles in the flow does not affect the mean liquid flow, but only the time-dependent fluctuations of the velocity caused by turbulence. The aforementioned analytical solution used for the axial (U_{jet}) and radial (V_{jet}) components of the mean velocity is the one described by Schlichting (1979) for the
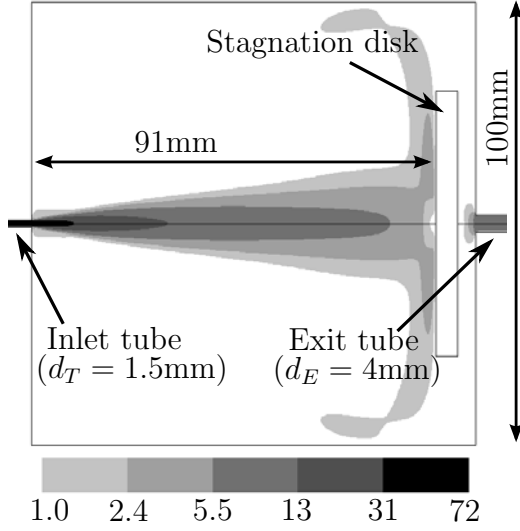
Figure 3.3: Experimental cell schematics with contours of constant velocity (cm/s), as obtained by CFD calculation, for a liquid jet with $Re = 690$.
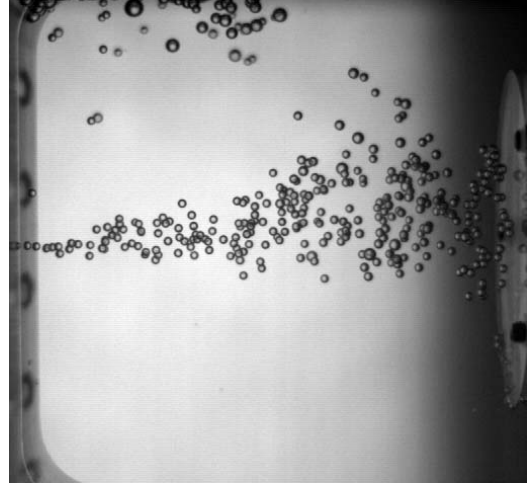

Figure 3.4: Snapshot of a typical experiment of slug bubble injection after 2 seconds of microgravity.

mean stationary flow of a turbulent jet in an infinite cavity:

$$
\begin{cases}
U_{\text{jet}} = \dfrac{3}{8\pi c}\sqrt{\dfrac{J}{\rho_l}}\left(\dfrac{1}{\left(1+\frac{1}{4}\eta^2\right)^2}\right)\left(\dfrac{1}{x}\right) , \\[3ex]
V_{\text{jet}} = \dfrac{1}{4}\sqrt{\dfrac{3J}{\pi\rho_l}}\left(\dfrac{\eta-\frac{1}{4}\eta^3}{\left(1+\frac{1}{4}\eta^2\right)^2}\right)\left(\dfrac{1}{x}\right) , \\[3ex]
\eta = \dfrac{1}{4c}\sqrt{\dfrac{3}{\pi}}\left(\dfrac{r}{x}\right) ,
\end{cases}
\tag{3.17}
$$

where c is an empirical constant adjusted experimentally as $c \simeq 0.0161$, x and r correspond respectively to the axial and radial distances from the injection point in cylindrical coordinates, ρ_l is the density of the fluid and J is the injected momentum rate.

As shown by Carrera et al. (2008), some considerations must be taken into account prior to compare the analytical solution to the experimental results. The first one is that equation (3.17) has been deduced for the case of an injector of nearly zero size (i.e. $d_T \to 0$). This is usually corrected by simply adding a small spatial displacement x_0 to the injection point on the analytical solution. This correction in the axial direction stands for the initial opening of the jet until it reaches the small, but finite, size d_T of our real injector.

The second consideration is that the effective injected momentum rate J must be modified. Although bubbles are passive in relation to the mean flow of the jet, the situation is very different at the injector, where the volume fraction of gas is much higher. The presence of bubbles in the injector increases the velocity of the liquid slugs between them, producing a larger effective injected momentum. Specifically, the mean velocity of the liquid in the capillary tube of section A_T can be expressed in a good approximation[4] as

$$\langle U_T \rangle = \frac{(Q_l + Q_g)}{A_T} \; , \tag{3.18}$$

being respectively Q_l and Q_g the volumetric flow rates of liquid and gas injected into the T-junction. Assuming that the momentum transmitted into the cavity by the gas flow will be negligible due to its small density, the amount of mass injected per unit time will only be determined by the liquid flow (i.e., $\rho_l Q_l$). This considerations lead us directly to the expression of the effective injected momentum:

$$J \; = \; \rho_l Q_l \langle U_T \rangle \; = \; Q_l(Q_l + Q_g)\frac{\rho_l}{A_T} \tag{3.19}$$

It is worth remarking that the effective Reynolds number, defined by the local diameter of the jet, remains constant all along it. This can be easily shown by observing that the opening angle of a turbulent jet remains constant with the distance [Schlichting (1979)], which implies that its width is directly proportional to the distance from the injection point (i.e., $L_c \propto x$), while on the other hand, the flow velocity scale, as seen in equation (3.17), is inversely proportional to the distance (i.e., $U_c \propto \frac{1}{x}$). This causes that the degree of turbulence is maintained through the jet, producing that, while the characteristic eddy velocity is being reduced downstream, its size increases instead[5]. The flow thus is statistically equivalent at different positions downstream, under the appropriate rescaling of time and length. Since the bubble size is essentially unchanged, this implies that the degree of interaction between bubbles and flow will change along the jet. Far downstream, the bubbles must eventually become passive tracers because, beyond a certain distance from the injector, the smallest eddies will become much bigger than bubbles, implying that the latter will be point-like to all effects. On the contrary, the situation is very different at the regions close to the jet inlet, where bubbles are comparable to the jet diameter and to the scale of velocity gradients. In those regions, bubbles will necessarily be active in relation to the liquid flow field.

---

[4]We neglect the small variations of gas volume produced by small changes of pressure that occurs at the entrance of the T-Junction

[5]Because, just as Re remains constant, the Reynolds number associated to eddies Re_λ as defined in equation (3.2) should remain constant as well

The appropriate definition of Reynolds number in order to properly describe the degree of turbulence inside the jet is defined by the characteristic velocity of the momentum injected $U_c = \sqrt{J/(\rho_l A_{\text{jet}})}$, which leads us to:

$$Re = \frac{L_{\text{jet}}}{\nu}\sqrt{\frac{J}{\rho_l A_{\text{jet}}}} = \frac{2}{\nu}\sqrt{\frac{J}{\rho_l \pi}} = \frac{4\sqrt{Q_l(Q_l + Q_g)}}{\pi \nu d_T} \ , \tag{3.20}$$

with d_T the diameter of the T-junction capillary tubes. This will be the definition of Reynolds number used over the present chapter.

For a further insight into the mean flow structure of a turbulent jet, from equation (3.17) we immediately find that:

$$\frac{V_{\text{jet}}}{U_{\text{jet}}} = 2c\sqrt{\frac{\pi}{3}}\left(\eta - \frac{1}{4}\eta^3\right) = \frac{1}{2}\left(\frac{r}{x}\right)\left(1 - \frac{1}{4}\eta^2\right) \ , \tag{3.21}$$

$$U_{\text{axis}} = \frac{3\nu Re}{16 c\sqrt{\pi}}\left(\frac{1}{x}\right) \ . \tag{3.22}$$

Using the typical parameters of jets studied in the present chapter, we find:

$$\begin{cases} U_{\text{axis}}^{(Re=690)} = \left(45.3\ \frac{\text{cm}^2}{s}\right)\frac{1}{x} \\[2ex] U_{\text{axis}}^{(Re=1170)} = \left(76.9\ \frac{\text{cm}^2}{s}\right)\frac{1}{x} \end{cases} \tag{3.23}$$

Reichardt (1942) measured that for a turbulent jet, the radial distance $r_{1/2}$ (defined as the distance where $U_{1/2} \equiv U(r_{1/2}) = \frac{1}{2}U_{\text{axis}}$) follows the relation

$$r_{1/2} = 0.0848\,x \ , \tag{3.24}$$

which was already used in the determination of the empirical constant c on equation (3.17). Using this relation in equation (3.17) we find that $\eta_{1/2} \simeq 1.286$, from which we have that, for any turbulent jet, at a given distance x from the injector:

$$V_{1/2} \simeq \frac{1}{40}U_{1/2} = \frac{1}{80}U_{\text{axis}} \ , \quad \forall x \ . \tag{3.25}$$
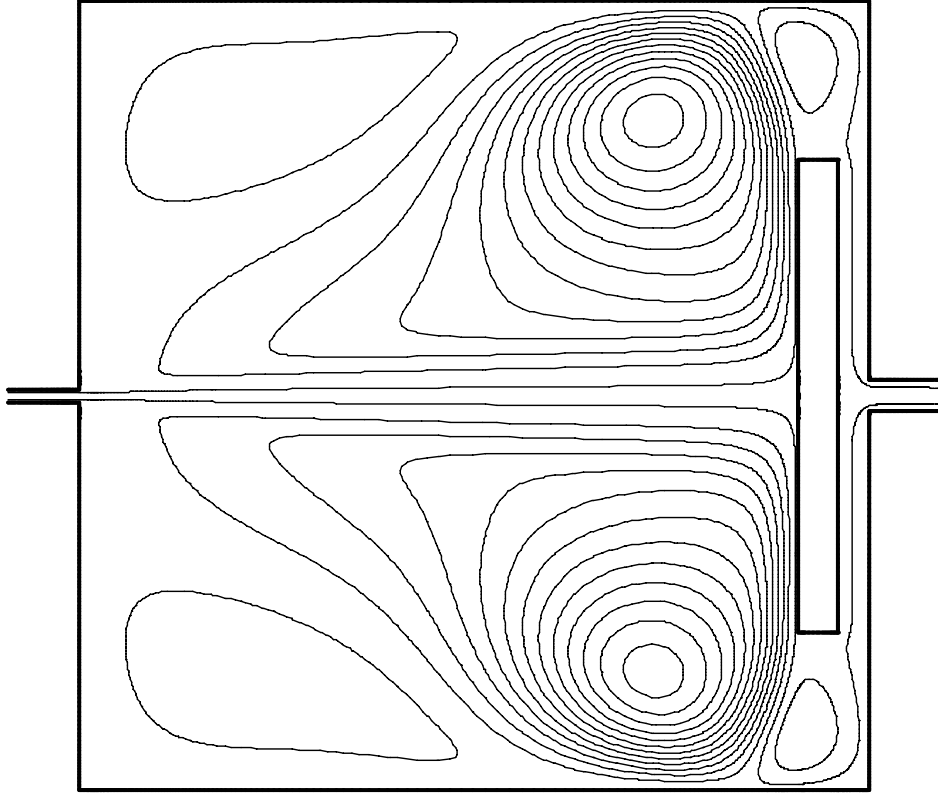
Analogously, at a distance $r_{1/4}$

Figure 3.5: Streamlines of the mean flow in the experimental cell, obtained from a simulation with axial symmetry.

$$
\begin{cases}
U_{1/4} \equiv \frac{1}{4} U_{\text{axis}} \\
V_{1/4} = 0 \\
\eta_{1/4} = 2 \\
r_{1/4} = 0.1318x
\end{cases}
\tag{3.26}
$$

which stands for the angle where the radial velocity V drops to zero. For higher radial distances $(r > r_{1/4})$ the velocity V becomes negative, corresponding to the flow elements that are joining to the jet from far away. In Fig.3.5 we show the streamlines of the mean flow in our experimental cell, where it can be observed the reincorporation of the flow elements into the jet boundaries due to recirculation in the finite cavity.

The angle of a turbulent jet is not defined unambiguously, due to the fluctuations of the boundary between the turbulent inner flow and the laminar outer flow. Nevertheless, for the scaling arguments held in the next section, we will treat the angle described in equation (3.26) as an effective width of the jet.

3.4   Scaling Arguments

From equation (3.26) we find that the jet size[6] increases as $L_c \simeq 2y_{1/4} \simeq 0.2636\,x$, which applied to the Kolmogorov scales in equation (3.8) for the case with $Re = 690$ (being that a typical degree of turbulence in our experiments), brings us directly to the relation

$$\lambda_k \sim L_c\,Re^{-3/4} \simeq 0.26\,x\,Re^{-3/4} \simeq 1.9 \cdot 10^{-3}x \; , \qquad (3.27)$$

and from equation (3.6) it follows that the size of the smallest eddies is

$$\lambda_{\min} \sim 10\lambda_k \sim 1.9 \cdot 10^{-2}x \; . \qquad (3.28)$$

On the other hand, as seen in equation (3.4), the most energetic eddies in a turbulent jet have the size

$$\lambda_{\mathrm{Max}} \simeq 3.9 \cdot 10^{-2}\,x \; , \qquad (3.29)$$

which show roughly one order of magnitude of separation between the size of the largest eddies and that of the smallest scales of turbulence, and no more than a factor 2 between the largest and the smallest eddies. This narrow range of scales is due to the small values of Re used in our experiments, caused by the low injection parameters necessary for a proper and controlled generation of bubbles.

As has been commented earlier, equations (3.28) and (3.29) show a direct dependence on the size of the eddies to the distance x from the injection point. From these expressions we can deduce the point at which the eddies will reach the size of the bubbles

$$\begin{cases} \lambda_{\mathrm{Max}}\,(x = 4 \text{ cm}) \sim d_B \approx 1.5 \text{ mm} \\ \lambda_{\min}\,(x = 8 \text{ cm}) \sim d_B \approx 1.5 \text{ mm} \\ \lambda_k\,(x = 80 \text{ cm}) \sim d_B \approx 1.5 \text{ mm} \end{cases} \qquad (3.30)$$

Analogously, as seen in section 3.2.2, it is also interesting to compare the characteristic times of turbulence with the response time of bubbles in order to better understand their kind of interaction. Downstream the flow, the velocity of eddies slows down while its size keeps increasing, thus its characteristic time must

---

[6]Note that we neglect the initial opening of the jet for simplicity of the scaling arguments, but close to the injector the actual size of the jet should read $L_c \simeq d_T + 0.2636\,x$. That is equivalent to introduce the change of variables for the following expressions of $x' \simeq x + 0.7$cm

increase as well. From equation (3.8) we find

$$T_c^{Re=690} = \frac{L_c}{U_c} \simeq \left(1.01 \cdot 10^{-2} \frac{\text{s}}{\text{cm}^2}\right) x^2 \,, \tag{3.31}$$

$$\tau_k^{Re=690} \sim \frac{T_c}{\sqrt{Re}} \sim \left(3.83 \cdot 10^{-4} \frac{\text{s}}{\text{cm}^2}\right) x^2 \,, \tag{3.32}$$

Knowing that the bubble response time τ_B, as seen in equation (3.16), is constant through the whole jet

$$\tau_B = \frac{d_B^2}{36\nu_l} \simeq 6.25 \cdot 10^{-2} \text{ s} \,, \tag{3.33}$$

we can calculate the distance x at which the time scales of the flow (T_c) and of Kolmogorov (τ_k) increase up to the value of the bubble response time.

$$\begin{cases} T_c(x = 2.5\text{cm}) \simeq \tau_B \approx 6.25 \cdot 10^{-2} \text{ s} \\ \tau_k(x = 13\text{cm}) \sim \tau_B \approx 6.25 \cdot 10^{-2} \text{ s} \end{cases} \tag{3.34}$$

Finally, the last relevant parameter in order to analyze possible interaction between the two phases, is the cross-sectional void fraction ϑ, defined as the fraction of the mean area occupied by gas A_g in a cross-section of the bubble jet $A_{\text{B.J.}}$.

$$\vartheta = \frac{A_g}{A_{\text{B.J.}}} \tag{3.35}$$

Due to the constant flow of gas injected into the experimental cell, we have

$$Q_g = A_g U_{\text{jet}} = \text{constant} \tag{3.36}$$

Knowing that the gas flux has to remain constant through any section of the jet (i.e., $Q_g =$constant) and that, as seen in equation (3.17), $U_{\text{jet}} \propto \frac{1}{x}$, it arises that $A_g \propto x$, from what it follows:

$$\vartheta = \frac{A_g}{A_{\text{B.J.}}} \propto \frac{x}{x^2} = \frac{1}{x} \tag{3.37}$$

In particular, assuming that the mean velocity is roughly constant at each cross-section of the jet ($U_c = \nu Re/L_c$), for our parameter of injection of a bubble jet of $Re = 690$ we find

$$\vartheta = \frac{A_g}{A_{\text{B.J.}}} \sim \frac{Q_g}{U_c A_{\text{B.J.}}} \simeq (0.146 \text{ cm}) \frac{1}{x} \,, \tag{3.38}$$

for which we have used the angle for the bubble jet $r_{\text{B.J.}} \simeq 0.15x$, measured from

the same experiment. It arises from expression (3.38) that the void fraction of the jet in our experimental cell is in the the range between 2% - 9% of gas, depending on the distance to the injection point.

The results on equations (3.30), (3.34) and (3.38) roughly divide the jet into 3 zones, in relation to the kind of influence exerted by bubbles to the flow:

- **Active range:** close to the injector, where $\phi_B \gtrsim \lambda_{\text{Max}}$ and $\tau_B \gtrsim T_c$. Here, the bubble size comprises large velocity gradients of the flow, and bubbles present a relative motion in relation to the highest scales of turbulence (due to the large relaxation time of bubbles). All that should result on bubbles having a strong impact on turbulence in all ranges, damping some of the smaller velocity fluctuations at the same time that they create wakes behind their movement. In our case of study, this would occur for the first 5 centimeters of jet.

- **Small interaction range:** at a medium distance, where $\lambda_{\text{Max}} \gtrsim 2\phi_B \gtrsim \lambda_k$ and $T_c \gtrsim 2\tau_B \gtrsim \tau_k$. Bubbles are able to follow the main structure of the turbulence (produced by the largest scales) which contain the majority of the turbulent energy. Since that energy goes from large scales to smaller ones, the effect of bubbles in this range should not have a major impact into the flow. Bubbles eliminate and generate eddies of their own size or smaller, so they do not interact with the larger scale turbulence, thus only modifying the detailed pattern of the smaller scales. In our case, this behavior occurs approximately in the range $8 \text{ cm} < x < 20 \text{ cm}$.

- **Passive range:** far from the injector, where $\lambda_k \gtrsim \phi_B$ and $\tau_k \gtrsim \tau_B$. Bubbles follow all the turbulence fluctuations and produce a negligible effect at any scale, acting like passive tracers of the flow. Approximately for $x > 80 \text{ cm}$.

Note that our experimental cell has only a length of 10cm, but we have analyzed the three possible ranges of interaction of bubbles in a theoretical frame for much longer jets. Also, from all this previous analysis we should conclude that bubbles should be in principle active and generate some appreciable back reaction to the flow for the majority of our jet length. This effect should appear to be even bigger considering that we can only measure velocities on bubbles, since we do not have any other tracer on the flow. However, it is important to take into account that the overall effect of the presence of bubbles on the statistics of turbulence will depend also on the void fraction. For the typically small values of void fraction, the effect may be quantitatively small. In fact, the results of Carrera et al. (2008) showed that the mean flow does not show a significant influence from the presence of bubbles and, as we will see later at the end of this chapter, the statistical

uncertainty of our measurements does not allow us to detect significant deviations from the numerical results of a liquid jet without bubbles. We attribute this, in first place, to the small void fraction, which drops below the 10% on gas after the first centimeter of jet (once we take into account the initial opening of the jet due to the injector size), and also for the small effect of wakes created behind bubbles at our small Reynolds numbers.

3.5   Stochastic Model

It is customary to decompose the total velocity field of a turbulent flow in two parts, a mean flow component and a fluctuating part. Regarding the first component, it is well known that the spatial structure of the mean flow velocity field of a turbulent single-fluid jet is independent of Re [Schlichting (1979)]. Since the experimental results of Carrera et al. (2008) indicated that the local averaged velocities of bubbles coincide to a good extent to that mean flow, the spreading of the spatial distribution of bubbles must be directly related to the fluctuating part of the flow. In figure 3.5 we can appreciate how the streamlines of the flow that are actually being injected into the cell only suffer a slight opening (of no more than twice its initial separation d_T) after the full length of the jet. It is easy to see how the larger width of the jet is determined by its external layers, that incorporate streamlines from the recirculating flow. In addition, turbulence provides a mechanism that mixes all those layers of mean flow, allowing the dispersion of bubbles through them. Hence, we need to make use of the local characteristics of turbulence in order to properly describe the dispersion of bubbles through the transversal layers of the flow and, at the same time, to confine them inside the boundaries of the jet, preventing them from freely disperse through the whole experimental cell, which would be unrealistic.

To describe both the mean flow and its velocity fluctuations we make use of a finite-volume scheme with a realizable k-ε model of turbulence, as described in chapter 2.1. Within this scheme, we will associate a local diffusivity to bubbles that is inherited from the diffusivity of the kinetic energy of the turbulent component of the flow in the absence of bubbles. The main assumption is thus that bubbles are also passive with respect to the fluctuating component of the flow. As seen earlier, this assumption is correct in principle sufficiently far downstream, where the bubble suspension becomes more and more dilute and the bubble size becomes negligible compared to the scales of the flow, but it may be questionable close to the inlet.

Since bubbles are not point-like and the number of them is relatively small, the aim of the model is to formulate an equation for the probability distribution

of finding a bubble at a certain location. The model does not intend to be a good description of the individual trajectories of bubbles, which are far from diffusive at small scales of the flow due to strong spatial and temporal correlations of the carrying flow. This implies, for instance, that the model will be inappropriate to describe properties related to the geometry of the bubble trajectories themselves or the correlations between them, such as the probability of bubble encounters and consequently of possible coalescence. Despite this shortcoming of the model, the assumption of a local diffusivity of the probability of finding bubbles may be reasonably justified to describe the spatial distribution of an ensemble of realizations, provided that coalescence events are rare.

To formulate the model we assume the dynamics of bubbles to be that of a biased random walk. We write explicitly the instantaneous velocity of a bubble $\mathbf{u}_B$ as a stochastic differential equation (Langevin equation) of the form:

$$\mathbf{u}_B(t) = \mathbf{U}(\mathbf{s}(t)) + \mathbf{u}'(t), \tag{3.39}$$

where $\mathbf{U}(\mathbf{s}(t))$ is the local mean fluid velocity at the position $\mathbf{s}(t)$ of the bubble and $\mathbf{u}'(t)$ is a fluctuating term of zero mean. This fluctuating term is responsible for the diffusivity of bubbles, therefore it should depend on the local properties of the turbulent flow. As mentioned above, we relate this diffusivity to that of the kinetic energy of the turbulent component of the flow without bubbles. Then, both terms of this decomposition (mean and fluctuating velocities) can be obtained from the integration of a k-ε model. In particular, writing the fluctuating term as a Gaussian zero-mean white noise with correlation:

$$\langle \mathbf{u}'(t_1)\mathbf{u}'(t_2) \rangle = 2D_p \delta(t_1 - t_2) \ . \tag{3.40}$$

The noise intensity D_p is taken as proportional to the diffusivity of the turbulent kinetic energy k^2/ε in the context of the k-ε model:

$$D_p = \frac{\mu_t}{\rho_l \sigma_p} = \frac{C_\mu}{\sigma_p} \frac{k^2}{\varepsilon}, \tag{3.41}$$

where $C_\mu = 0.09$ according to the standard model, and σ_p is in principle a fitting parameter that connects the diffusivity of P to the eddy viscosity μ_t. The prediction of this model regarding the spatial structure of the bubble jet does not seem very sensitive to the parameter σ_p, so we take $\sigma_p = 1$ as in the transport equation of k (i.e., $\sigma_k = 1$), considering that both diffusivities must be similar, being both equally originated by the eddy mixing [Versteeg and Malalasekera (1995)].

The Langevin equation (3.39) can be numerically integrated by standard methods, with the result of individual trajectories of single independent bubbles. Ex-
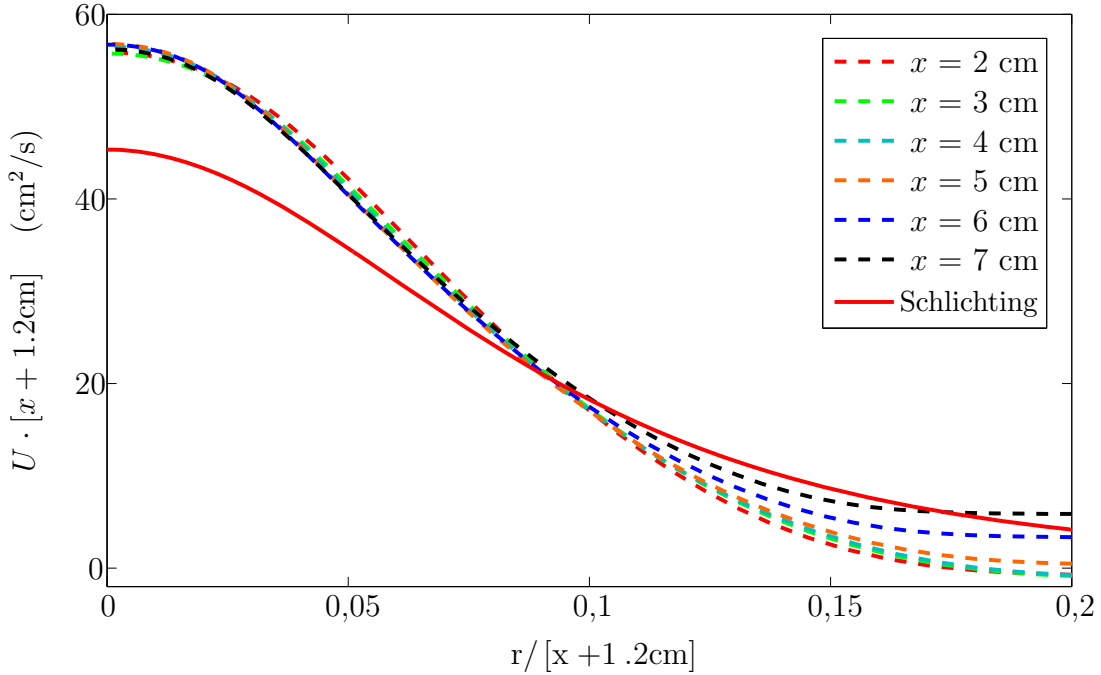
Figure 3.6: Collapse of many curves of $U \cdot (x + x_0)$ for a jet with $Re = 690$. Dashed lines show the simulation results at various transversal sections of the jet. Solid line corresponds to Schlichting's analytical solution presented on equation (3.17)

 amples of such integration are shown in the next section. Within this scheme one may easily determine the probability density $P(\mathbf{s}, t)$ of finding a bubble in a certain position at any instant of time. This distribution coincides with the concentration of an ensemble of independent bubbles, and is given by the so-called Fokker-Planck equation associated to the stochastic differential equation (3.39). This equation has the form:

$$\frac{\partial P(\mathbf{s}, t)}{\partial t} + \nabla \cdot (\mathbf{U}P) = \nabla \cdot [D_p \nabla P]. \tag{3.42}$$

In this framework, the concentration of bubbles, proportional to the probability distribution P, diffuses as a passive scalar advected with the mean flow velocity $\mathbf{U}(\mathbf{s}, t)$, but with a diffusion coefficient $D_p(\mathbf{s}, t)$ which depends on the local properties of the turbulence through the field k^2/ε.

3.6   Spatial structure of bubble jets

Our numerical computations have been carried out with the help of the commercial software FLUENT. In Fig. 3.3 and 3.5 we show the structure of the mean velocity field for the turbulent jet as computed within the k-ε model. In these figures it is easy to see how the finite size characteristics of the experimental cell seems to play
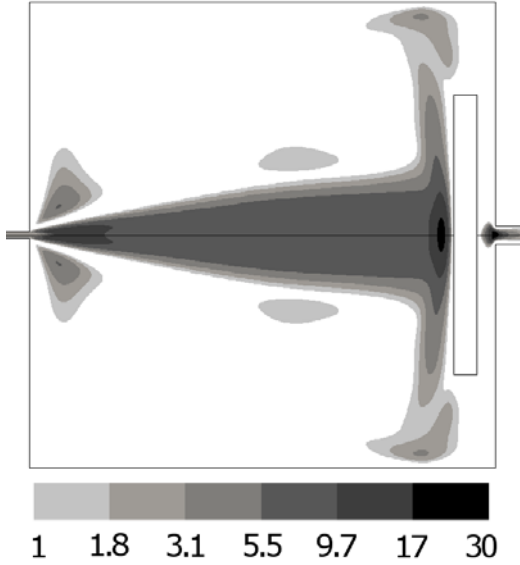
Figure 3.7: Contours of constant k^2/ε (10^{-1} cm^2/s), as obtained by CFD calculations.

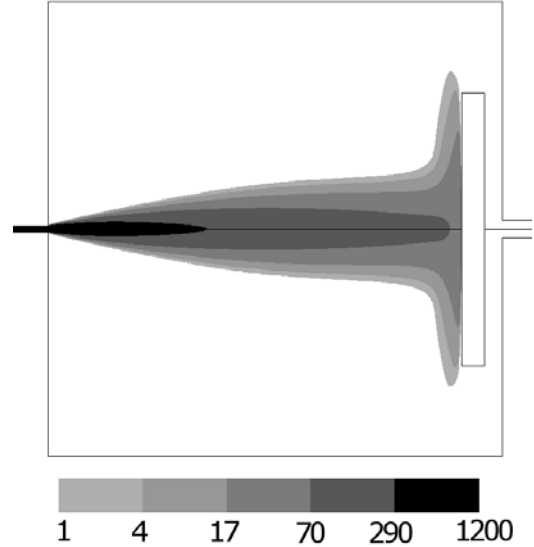**Figure 3.8:** Contours of constant bubble concentration in an arbitrary scale, corresponding to a local diffusivity proportional to k^2/ε, as obtained by integration of the Fokker Planck equation by using the CFD results.

an important role in the flow, specially in the areas with strong recirculation and near the stagnation disk, where the Schlichting solution presented in equation (3.17) might not portray a suitable description. In Fig. 3.6 we compare the results obtained from the numerical integration of the model with those provided by the Schlichting solution. We can observe how the numerical solution of the jet presents a sharper opening angle than the case of the analytical solution for an infinite system, which produces in the first one a higher central velocity for the same injected momentum. Despite this discrepancy in the opening angle, the jet maintains its velocity decay proportional to $\frac{1}{x}$, as well as its dependence with the ratio $\frac{r}{x}$, which is maintained for the internal layers of the jet up to $\frac{r}{x} \simeq 0.10$. Outside this boundaries, the recirculation due to the finite size conditions become more significant and, accordingly, its corresponding lines split in the figure.

To visualize the degree of inhomogeneity in our model regarding the diffusivity of bubbles, we plot in Fig. 3.7 the quantity k^2/ε, which is in principle proportional to the effective local diffusion coefficient of bubbles. The local diffusivity is remarkably homogeneous in a certain central area and abruptly drops on the sides, defining relatively clear-cut jet boundaries. This drop in diffusivity is larger than one order of magnitude in a relatively narrow layer. Therefore it explains the small sensitivity of the results to small changes in σ_p on the determination of the

diffusion coefficient D_P, since bubbles disperse through the whole central region, delimited by this narrow boundary layer. For larger variations of σ_p (of around one order of magnitude) we reach the extreme behaviors possible for any scalar transport equation. In the case with $\sigma_p \gtrsim 10$ the advection term predominates over diffusion, producing a negligible dispersion of P over the various layers of the jet, hence it remains following the central streamlines of the mean flow, predicting a very underestimate opening angle of the bubble jet. On the contrary, for $\sigma_p \lesssim 0.1$, diffusion predominates over advection, resulting in an overestimation of the opening angle and unrealistic results near the injector, product of an extreme diffusivity.

In Fig. 3.8 we show the resulting bubble concentration contours, obtained from the numerical integration of equation (3.42). As indicated earlier, bubble spreading is limited by the jet boundaries, and the resulting spatial distributions are similar to those of experiments. Remarkably, this is not the case if a homogeneous diffusivity is used (instead of one locally depending on k^2/ε). The use of a single value of diffusivity for the whole system results in a distribution of bubbles that either opens a very small angle (consistent with a scalar transport dominated by advection), or spreads out of the limits of the jet following an unrealistic behavior (corresponding to a transport dominated by diffusion), depending on the value taken for the diffusivity. An example of bubble distribution P in the case of constant diffusivity is shown in Fig. 3.9. We therefore conclude that, within the k-ε model, an inhomogeneous diffusivity is essential to capture the qualitative shape of the spatial distribution of bubbles.

In order to be able to compare the 2D, projected snapshots of the experiment with the cylindrically symmetric simulations, we have to integrate the numerical results over the projected dimension, transversally to the plane of the pictures. Doing that for different slices of the cell, we obtain a series of profiles that represent the concentration of bubbles at various distances from the injection point. A direct comparison with a snapshot of the experiment such as that in Fig. 3.4 is not adequate since the number of bubbles is relatively small while the prediction involves an ensemble average of realizations. A simple way to visually compare the prediction with the data is to superpose a series of successive snapshots of an experiment, to delimit the region that is eventually visited by bubbles. This is shown in Fig. 3.11. We have also drawn the 2D-projected concentration profiles given by the numerical integration of the model in four different sections of the experiment. This qualitative comparison shows a good agreement with the experiment as far as the dependence of the jet width is concerned. The actual density profiles cannot be directly compared with a gray scale of the bubble superposition because this is the result of a single experiment and because the high degree of screening of bubbles along the visual line. The regions with a significant
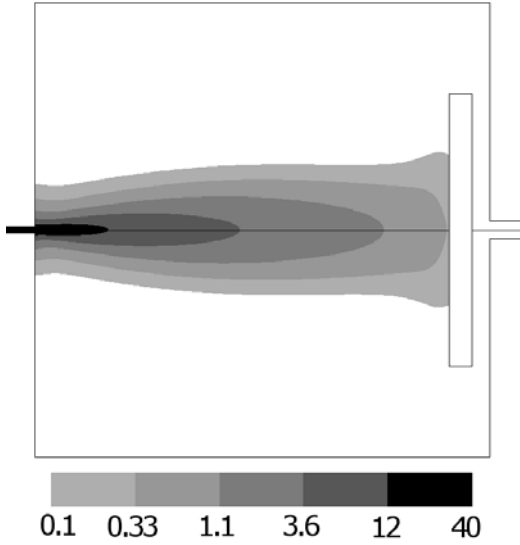
Figure 3.9: Contours of constant bubble concentration in an arbitrary scale, corresponding to a homogeneous bubble diffusivity, as obtained by integration of the Fokker Planck equation. Unrealistic degree of diffusion is present close to the injector.
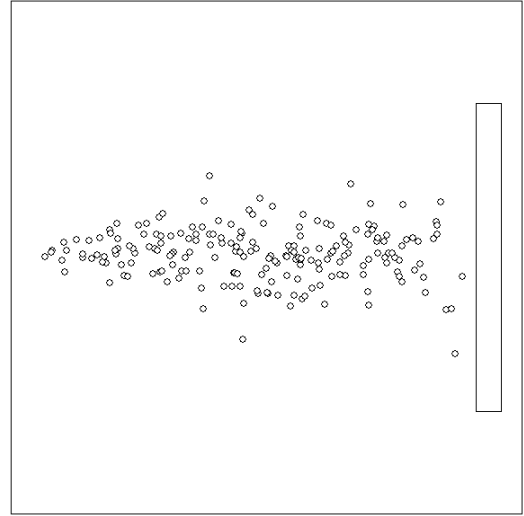

Figure 3.10: Simulation of the Langevin dynamics coupled to the k-ε model of turbulence, of bubbles injected periodically at the inlet. The snapshot is statistically similar to that of Fig. 3.4

density predicted by the theory are coincident with the limits of the bubble jet observed, except in the last profile, which is close to the stagnation disk and has an enhanced bubble dispersion. Note also that the experimental jet is slightly deformed, deviating upwards in the figure. This is a spurious effect due to the preparation of the experiment which is done in normal gravity with a pre-jet of bubbles breaking the cylindrical symmetry in the initial condition of the carrying flow. The bubbles injected in normal gravity prior to the drop release can be seen in the upper part of the picture.

As a final qualitative test of the physical picture, we have reconstructed a bubble jet from trajectories consistent with our probabilistic model. That is, we have evolved an ensemble of bubbles injected periodically at the inlet and undergoing a biased random walk given by the Langevin equation (3.39). Then the local mean velocity is obtained from the stationary mean flow field solution given by FLUENT within the k-ε model, and the fluctuating term is calculated as a white noise as described by equations (3.40) and (3.41), with the local diffusion coefficient given by the same model. We use a simple Euler scheme to solve the Langevin equation for each bubble, and the computation of the stochastic term at each step follows a standard algorithm to ensure that the ensemble average will coincide with that predicted by the corresponding Fokker-Planck equation
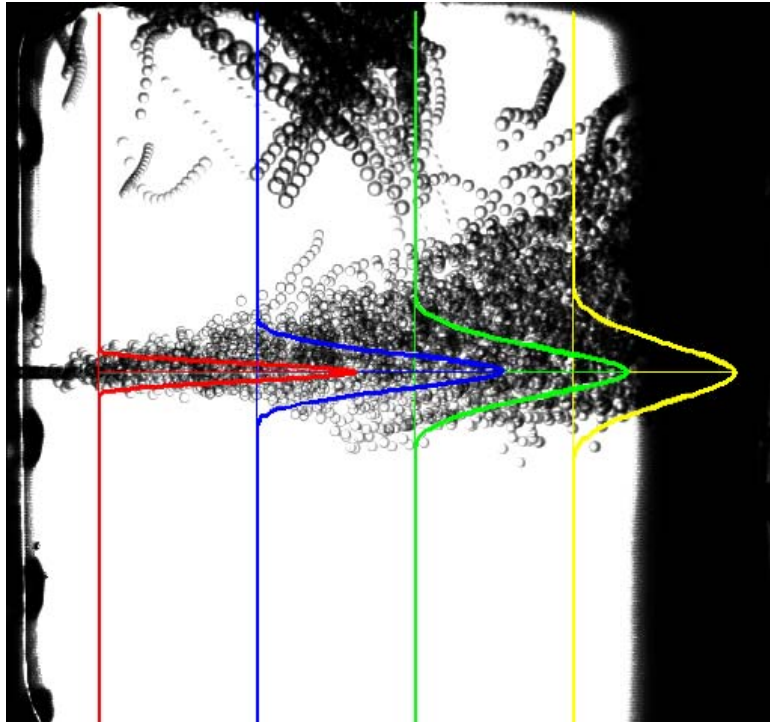
Figure 3.11: Superposition of a series of experimental snapshots, compared to the 2D-projected concentration profiles. The values of concentration are plotted in an arbitrary scale along the x-axis, with the zero of each profile at the position of the corresponding section of the flow. See the discussion in the text.

[Gardiner (2009)]. The method is just a means to generate individual realizations of the system including the trajectories of all individual bubbles, consistently with the assumption that bubbles are not interacting with each other and do not affect the carrying flow. Although the real trajectories within a turbulent flow at the scale of our experiment cannot be considered as given by such a simple diffusion process, in particular at small scales and short times, the model can nevertheless yield an accurate approximation to the statistics of bubble positions at a given time. As an illustration of the behavior predicted by our model, in Fig. 3.10 we plot a representative example of such a simulation showing reasonable qualitative agreement with a snapshot of a typical bubble jet as that shown in Fig. 3.4.

3.7   Experimental results on the jet structure

In order to measure the position and velocity of each bubble during the experiments, we processed all the images taken by the high speed video camera, so that an automatic particle tracking software was able to identify the paths described
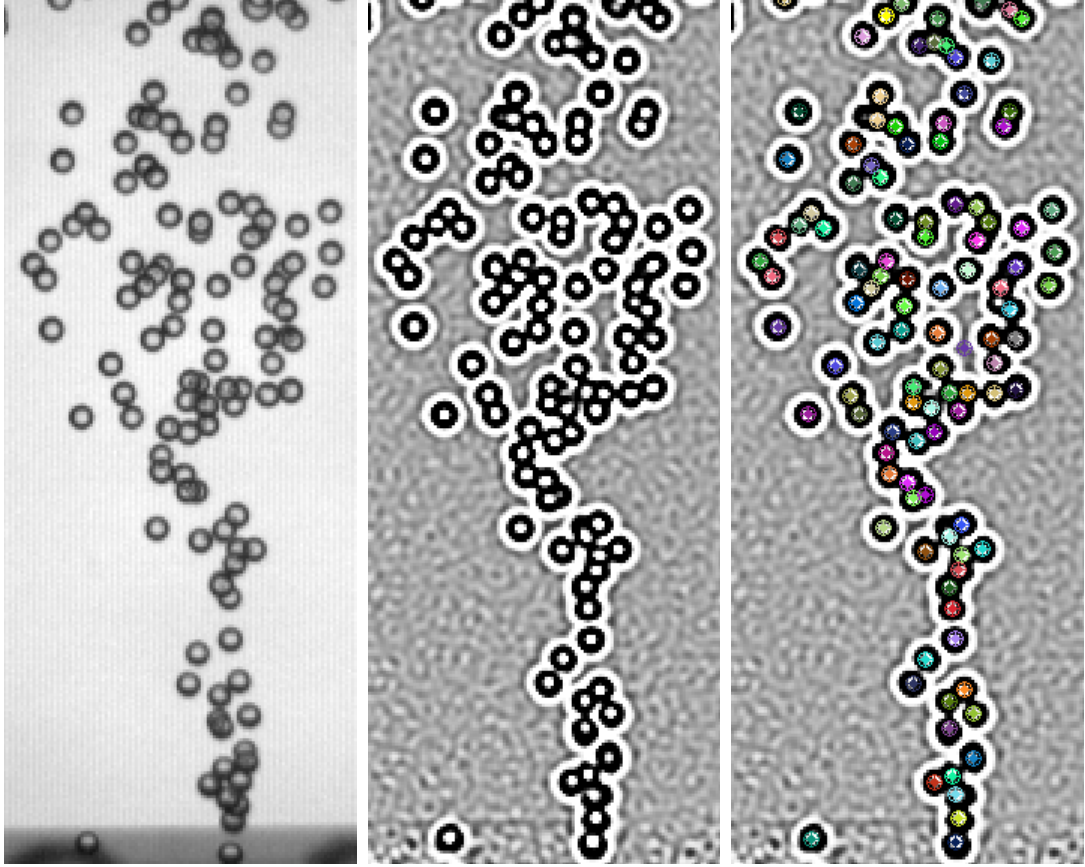
Figure 3.12: Tracking of the bubbles in the jet. *(Left):* Original snapshot taken by the video camera. *(Center):* Image processed. *(Right):* Automatic identification of the bubbles, being each colored circle a different track recognized by the software.

by all the bubbles. To this aim, first it has been necessary to homogenize the background of all the frames by subtracting, to each of them, a picture taken by the same camera in the absence of bubbles. After the background correction, we have used a standard filter to highlight the interphase of each bubble. Finally, it has been possible to identify the trajectories of all the bubbles by tracking the white area strongly highlighted in their central part, which is surrounded and separated from the rest of bubbles by a clear interphase. This is exemplified in Figure 3.12.

We have analyzed the position and instantaneous velocity of all bubbles for the most characteristic and well behaved experiments, corresponding to the cases with $Re = 690$ (with parameters of injection Q_l=41 ml/min, and Q_g=16 ml/min) and $Re = 1170$ (with Q_l=74 ml/min, and Q_g=18 ml/min). More details on the experimental setup can be found in [Carrera et al. (2008)]

Since the experimental data is taken from 2D snapshots where our real 3D

configuration has been projected, some of the information is lost in the process. In the first place, the component of the velocity of bubbles in the direction z, perpendicular to the plane of the snapshot, cannot be measured. This is not a major issue since the main component of the velocity is u_x, in the axial direction x. In addition to this, the properties of the flow in the directions y and z should be statistically equivalent. The actual problem is that we cannot identify the depth z at which any bubble is placed, therefore when we conduct a statistical analysis of bubble velocities, we are inevitably mixing velocities that were in fact at different layers of the jet.

In order to compare the mean superficial density of bubbles ρ_b from the experimental snapshots with that from the numerical results, we integrate the probability density of bubbles P over the visual dimension z in the form

$$\rho_b(x,y) = C_b \int_{-\infty}^{\infty} P(x,y,z) \, dz \, , \tag{3.43}$$

as we have done before for the numerical profiles in Fig. 3.11. Since P has been calculated in an arbitrary scale (we have not fixed the frequency of injection of bubbles), we introduce C_b as a constant to fix the density scale in the simulations in order to fit the experimental results. In Fig. 3.13 we compare the experimental results with the numerical predictions of ρ_b for different sections of the jet. The experimental values have been obtained by measuring the mean number of bubbles on small areas of the snapshots, averaged over the whole duration of the microgravity conditions. The constant C_b in equation (3.43) has been fixed by imposing the same mean number of bubbles on the section at $x = 3$ for both numerical and experimental results. This number of bubbles is obtained by calculating the area below the curves in Fig. 3.13 at that distance.

As we have commented earlier, the protocol to generate a uniform slug flow requires to start injecting bubbles some time prior to the microgravity conditions. This is done in order to avoid the large transients produced until a homogeneous generation of bubbles is achieved, which would cause a further reduction of our already small experimental time in microgravity conditions. The downside of this procedure is that the gas injected during normal gravity conditions is accelerated due to buoyancy forces and drags some of the liquid on its trajectory, producing a residual liquid flow. Although buoyancy forces disappear immediately at the start of the microgravity conditions, a transient of this residual flow remains that breaks the cylindrical symmetry of the jet, giving it a slight inclination upwards. This can be observed in the small lateral shift of the experimental measures in Fig. 3.13. Also the opening angle of the bubble jet seems to be slightly smaller in the simulations, as it can be observed in the figure at high distances from the injection point (i.e., $x = 5$cm and $x = 7$cm), arguably produced by the real effect
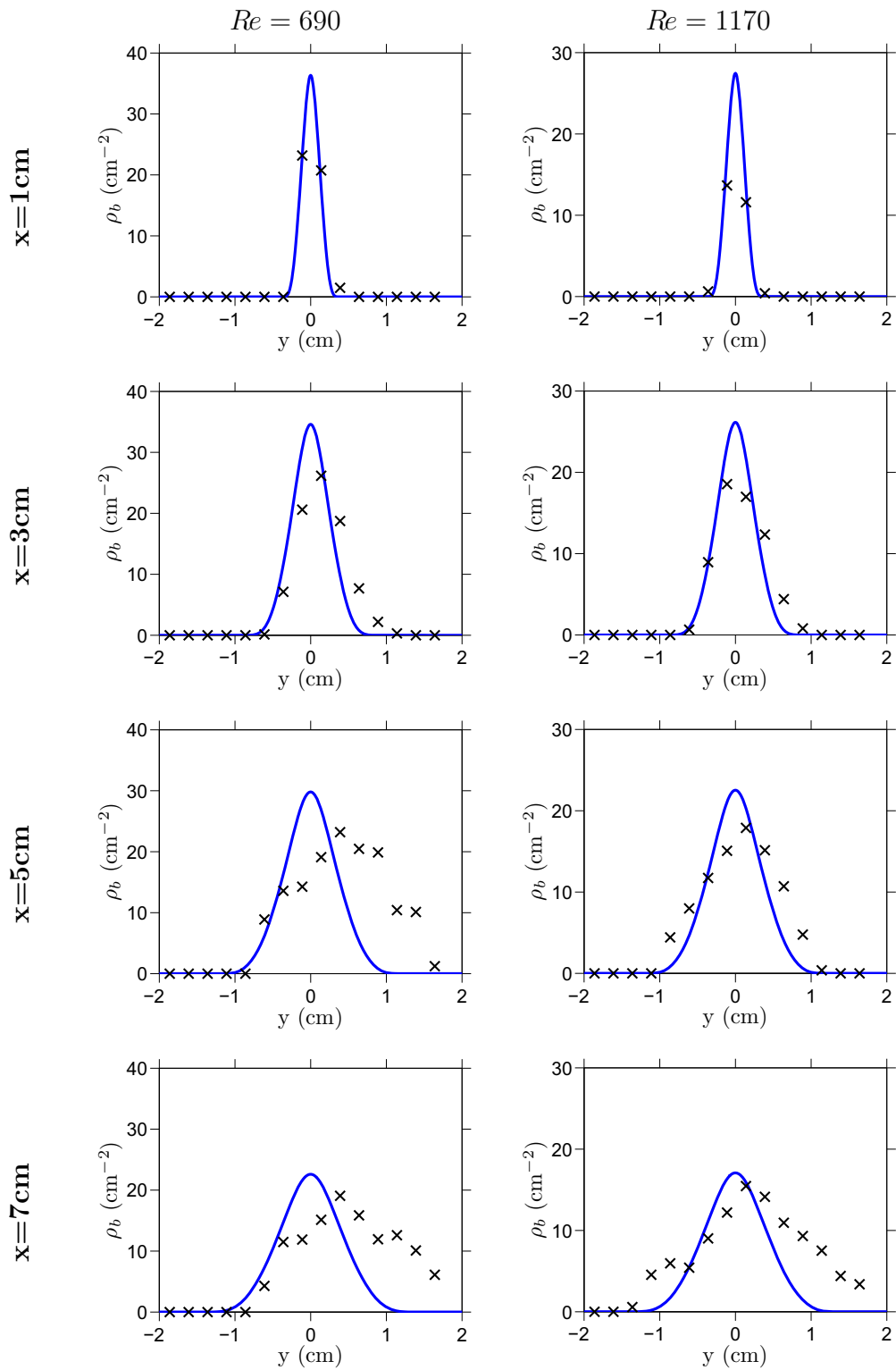
Figure 3.13: Superficial density of bubbles at various sections of a jet ($x = 1$cm, 3cm, 5cm and 7cm) for the cases of jets with $Re = 690$ and $Re = 1170$. Solid lines correspond to simulations and crosses to experimental results
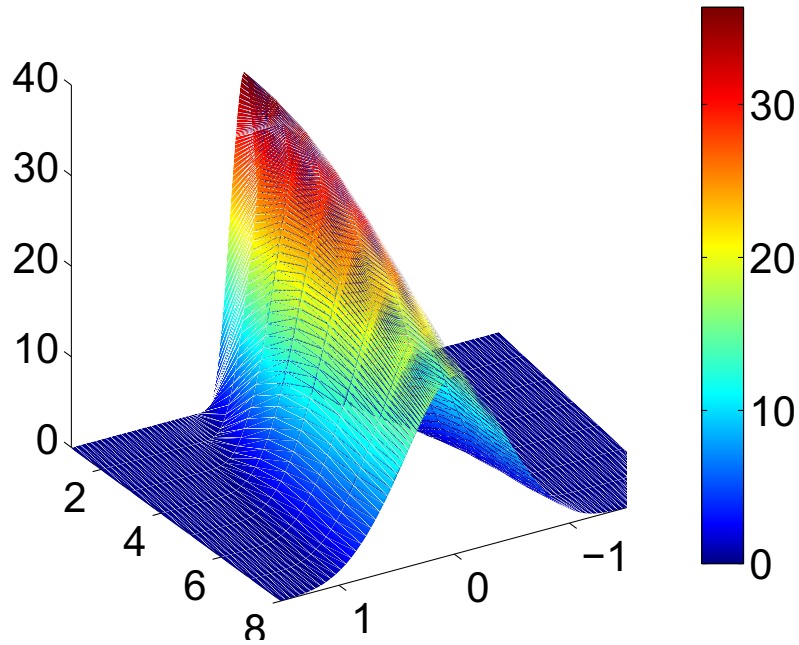
Figure 3.14: Superficial density of bubbles ρ_b (cm^{-2}) obtained from a simulation with $Re = 690$, for all points on the projected xy plane

Figure 3.15: Superficial density of bubbles ρ_b (cm^{-2}) obtained experimentally in the case of $Re = 690$, for all points on the projected xy plane

of the finite size conditions of our experimental cell. Within the above disclaimers and taking into account that the statistics of the data is necessarily limited because of the restricted access to the microgravity conditions, the experimental data fit reasonably well with the numer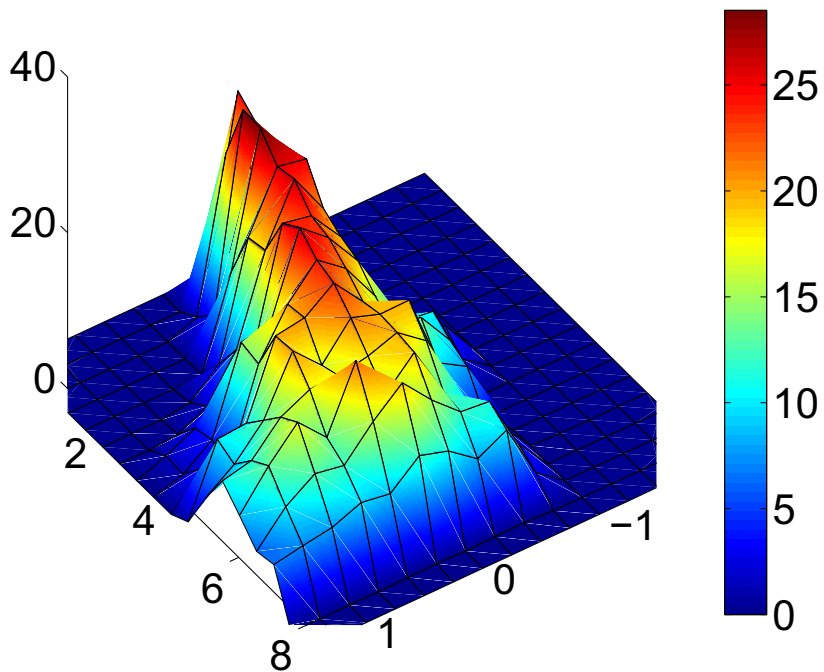ical prediction of our model, in particular in the intermediate range of distance to the inlet, when the prediction of the model is most accurate. At the end of the jet, the cumulative effect of the symmetry-breaking spurious flow associated to the normal-gravity preparation of the initial condition is most pronounced.

In Figs.3.14 and 3.15 we show a 3D representation of the superficial density of bubbles ρ_b, but in this case for any point of the projected xy plane, corresponding to all the points where the data can be measured from the experimental snapshots.

The next step is to study the statistics of velocities and velocity fluctuations of bubbles in the jet. As before, since we cannot know the z coordinate of the bubbles position, we need to integrate the numerical predictions over that dimension. In this case, one must take into account that not all planes at different depths have the same effect on the statistics, since layers where we have more bubbles will present a more significant impact on the statistics. Accordingly, in order to compare the experimental velocity profiles $\langle u_x^{\text{exp}} \rangle$ with the numerical results obtained by CFD calculations $\langle u_x^{\text{sim}} \rangle$, it is necessary to introduce this projection effect into the simulation outcome. The way of achieving this is by integrating the velocity of the flow $u_x(x, y, z)$ over the visual dimension z with the help of a weight factor $P^{\star}(x, y, z)$ which stands for the proportion of bubbles at each point. $P^{\star}$ corresponds to the probability density of bubbles $P(x, y, z)$ normalized over the visual dimension z in the form:

$$P^{\star}(x, y, z) \equiv \frac{P(x, y, z)}{\displaystyle\int_{-\infty}^{\infty} P(x, y, z) \, dz} \, , \tag{3.44}$$

$$\int_{-\infty}^{\infty} P^{\star}(x, y, z) \, dz = 1 \, . \tag{3.45}$$

Then, the projected mean velocities of the flow, given by the simulations are

$$\left\langle u_x^{\text{sim}} \right\rangle = \left\langle \int_{-\infty}^{\infty} dz \, P^{\star}(x, y, z) \, u_x(x, y, z, t) \right\rangle \, , \tag{3.46}$$

which, under permutation of the order of the dimensional integration and the statistical mean "$\langle \ \rangle$", yields

$$\left\langle u_x^{\text{sim}} \right\rangle = \int_{-\infty}^{\infty} dz \, P^{\star}(x, y, z) \, \left\langle u_x(x, y, z, t) \right\rangle \tag{3.47}$$

Similarly to the analysis in equation (2.5) in chapter 2.1.1, velocity u_x can be expressed as the sum of a mean velocity U_x plus a fluctuating part u'_x with zero mean that describe the degree of fluctuations over time.

$$u_x(x, y, z, t) = U_x(x, y, z) + u'_x(x, y, z, t) \tag{3.48}$$

$$\langle u_x(x, y, z, t) \rangle = U_x(x, y, z) + \langle u'_x(x, y, z, t) \rangle = U_x(x, y, z) \tag{3.49}$$

Applied to equation (3.47) we finally obtain:

$$\langle u_x^{\text{sim}} \rangle = \int_{-\infty}^{\infty} dz \ P^\star(x, y, z) \ U_x(x, y, z) \tag{3.50}$$

Due to the inherent uncertainty on the actual Reynolds number injected in the experiments, which may slightly fluctuate and deviate from the nominal value in a rather uncontrolled way, we have left an overall factor on the velocity scale of the simulations as an adjustable parameter. Since the structure of the jet should be equivalent for small injection variations, we scaled the velocity results of the simulations so that the maximum velocity $\langle u_x^{\text{sim}} \rangle$ in the section $x = 3$cm coincide with the measured experiments, i.e.,

$$\langle u_x^{\text{sim}}(x = 3\text{cm}) \rangle_{\text{Max}} = \langle u_x^{\text{exp}}(x = 3\text{cm}) \rangle_{\text{Max}} \ . \tag{3.51}$$

For the case with $Re = 690$ the simulated velocities have been scaled by a factor 0.69, and the ones of the case with $Re = 1170$ by a factor 0.79. The same factor has been applied to all measured observables corresponding to the same experiment. In Fig. 3.16 we compare the numerical results with the experimental data from our measurements.

For the study of the magnitude of the velocity fluctuations σ_{sim} we will have to follow a similar procedure, but we have no free parameter left for the fitting. This time, for a matter of simplicity of notation, we will not show the dependencies of each variable. In the study of the velocity fluctuations in our projected images, it is important to distinguish between the intrinsic fluctuations due to turbulence with respect to the local mean flow, from the apparent velocity variations along the visual direction already contained in the mean flow, which will already give a finite contribution even if the flow is laminar. Starting from the definition of variance

$$\left(\sigma_x^{\text{sim}}\right)^2 \equiv \left\langle \left(u_x^{\text{sim}}\right)^2 \right\rangle - \left\langle u_x^{\text{sim}} \right\rangle^2 \ , \tag{3.52}$$

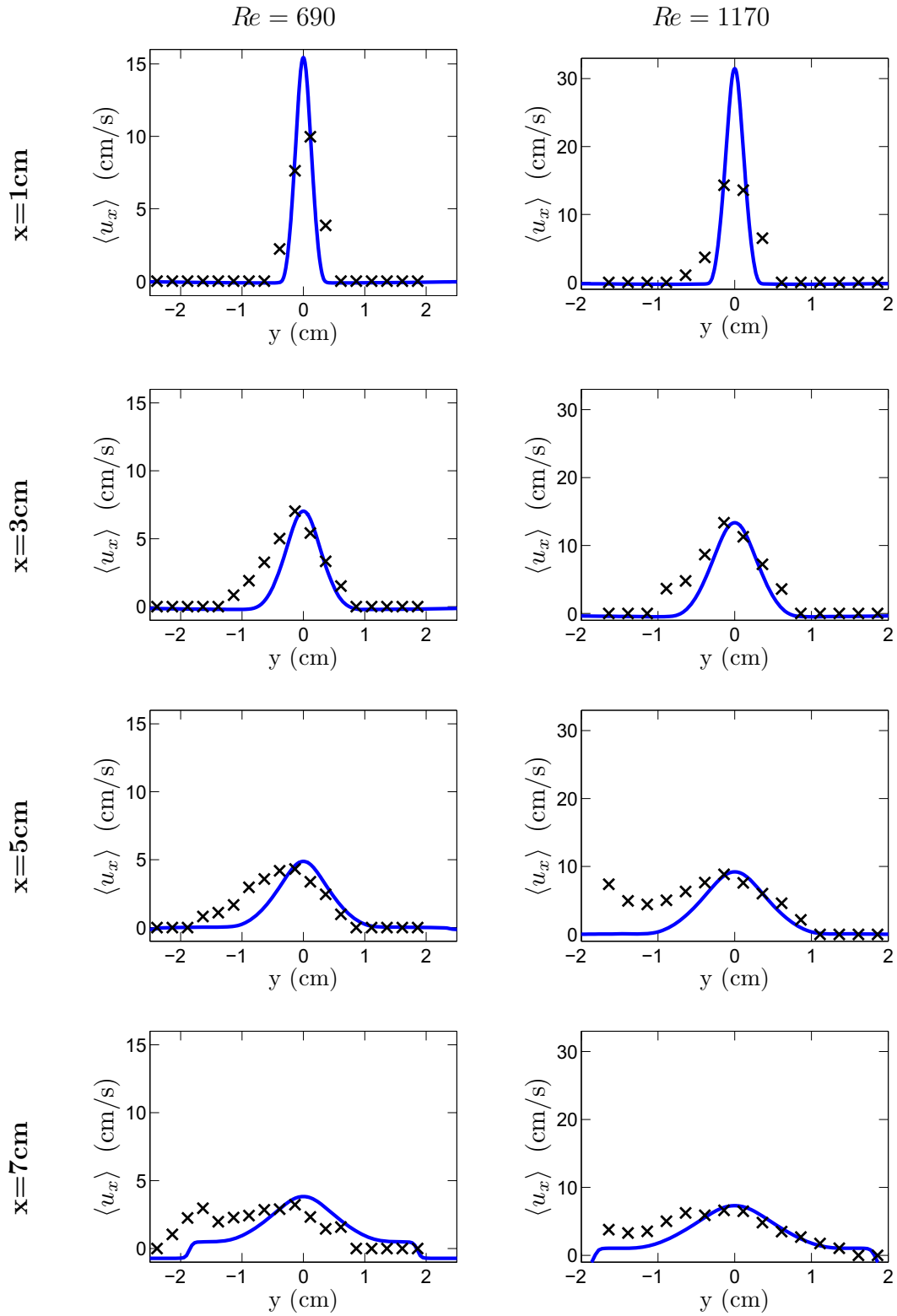and using the relations previously seen in equations (3.46) and (3.47), we imme-

Figure 3.16: Mean axial velocity at various sections of a jet (x = 1cm, 3cm, 5cm and 7cm) for the cases of jets of $Re = 690$ and $Re = 1170$. Solid lines correspond to simulations $\langle u_x^{\mathrm{sim}} \rangle$ and crosses to experimental results $\langle u_x^{\mathrm{exp}} \rangle$

diately find

$$
\begin{aligned}
\left(\sigma_x^{\mathrm{sim}}\right)^2 &= \left\langle \int_{-\infty}^{\infty} dz\, P^\star\, u_x^2 \right\rangle - \left\langle \int_{-\infty}^{\infty} dz\, P^\star\, u_x \right\rangle^2 \\
&= \int_{-\infty}^{\infty} dz\, P^\star\, \left\langle U_x^2 + 2 U_x u_x' + u_x'^2 \right\rangle - \left(\int_{-\infty}^{\infty} dz\, P^\star\, \left\langle U_x + u_x' \right\rangle \right)^2 \qquad (3.53) \\
&= \int_{-\infty}^{\infty} dz\, P^\star\, \left(U_x^2 + \left\langle u_x'^2 \right\rangle \right) - \left(\int_{-\infty}^{\infty} dz\, P^\star\, U_x \right)^2 .
\end{aligned}
$$

As seen in section 2.1.2, we define the kinetic energy of turbulence k on equation (2.10) as

$$
k = \frac{1}{2} \left(\left\langle u_x'^2 \right\rangle + \left\langle u_y'^2 \right\rangle + \left\langle u_z'^2 \right\rangle \right) . \qquad (3.54)
$$

Using an assumption of isotropic turbulence, we obtain:

$$
\left\langle u_x'^2 \right\rangle = \left\langle u_y'^2 \right\rangle = \left\langle u_z'^2 \right\rangle , \qquad (3.55)
$$

$$
k = \frac{3}{2} \left\langle u_x'^2 \right\rangle , \qquad (3.56)
$$

which, when introduced into equation (3.53) and after rearranging, allow us to express the magnitude of the velocity fluctuations of bubbles σ_x^{sim} as:

$$
\left(\sigma_x^{\mathrm{sim}}\right)^2 = \int_{-\infty}^{\infty} dz\, P^\star\, U_x^2 - \left(\int_{-\infty}^{\infty} dz\, P^\star\, U_x \right)^2 + \frac{2}{3} \int_{-\infty}^{\infty} dz\, P^\star\, k . \qquad (3.57)
$$

This equation can actually be expressed as:

$$
\left(\sigma_x^{\mathrm{sim}}\right)^2 = \sigma_0^2 + \sigma_k^2 , \qquad (3.58)
$$

$$
\sigma_0^2 = \left(\int_{-\infty}^{\infty} dy\, P^\star\, U_x^2 \right) - \left(\int_{-\infty}^{\infty} dy\, P^\star\, U_x \right)^2 , \qquad (3.59)
$$

$$
\sigma_k^2 = \frac{2}{3} \int_{-\infty}^{\infty} dz\, P^\star\, k . \qquad (3.60)
$$

In these expressions, σ_0 stands for the magnitude of the apparent fluctuations due to the 3D structure of the jet, already present for the a mean flow and which arise from the comparison of mean velocities at layers of different depth along the visual line. On the other hand, σ_k stands for the projection of the intrinsic fluctuations of the velocity at the different layers of the jet, those due to turbulence.

In Fig. 3.17 we compare the velocity fluctuations of the experimental data with the numerical predictions calculated with equation (3.57), with no additional fitting parameter, since the velocity scale has already been fitted using the velocity

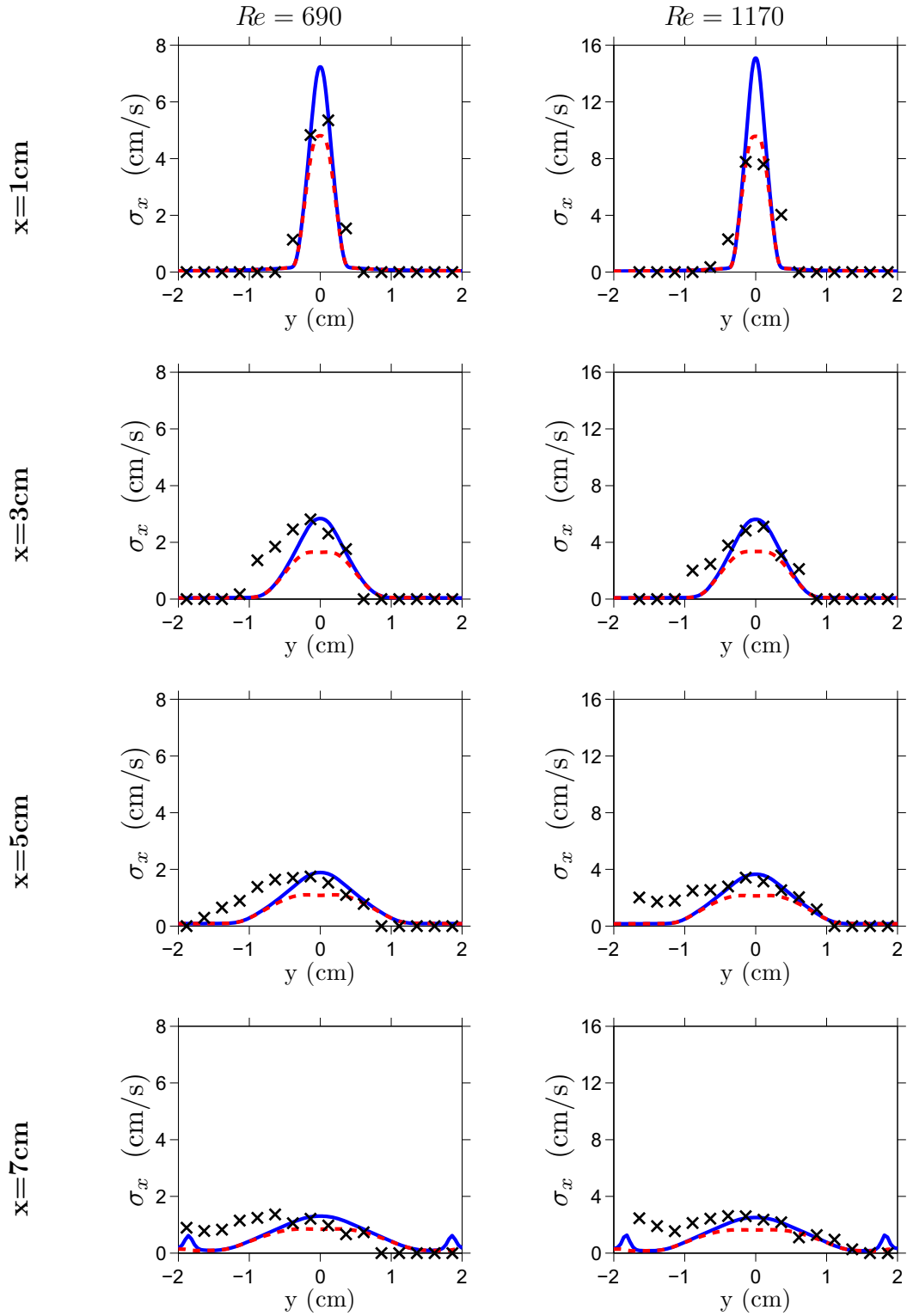**Figure 3.17:** Velocity fluctuations at various sections of a jet (x=1cm, 3cm, 5cm and 7cm) for $Re = 690$ and $Re = 1170$. Solid lines correspond to simulations σ_x^{sim} and crosses to experimental results σ_x^{exp}. Dashed red lines correspond to σ_k, defined on Eq. (3.60)

measurements. Dashed lines show the value of σ_k as defined in equation (3.60), to illustrate the magnitude of the intrinsic velocity fluctuations due to turbulence in relation to the apparent ones. As for the measurements on the bubble spatial dispersion, for both the measurements of mean values and dispersion of bubbles velocities, the prediction of the k-ε model is also reasonably accurate, within the inherent uncertainties of the experimental data.

3.8   Discussion and conclusions

We have presented a stochastic model that captures the essential statistics of bubble spatial dispersion in turbulent bubble jets formed by injection of capillary slug flows. The model is based on a simplified description of the turbulent flow within the realizable k-ε scheme. Even with the simplifications of the model, the treatment of bubbles as passive tracers with a local diffusivity associated to the k-ε model seems to capture reasonably well the ensemble dynamics of the bubbles. Numerical results obtained with our model compare well with experiments. On the other hand, we show that the simpler alternative of using a homogeneous bubble diffusivity would give results whose qualitative features would differ dramatically from experiments.

Simple scaling analysis comparing the bubble size and the scales of turbulence in this system indicate that the interaction between bubbles and its effect upon the carrying flow cannot be neglected in the regions relatively close to the inlet. However, our analysis shows that, even though potentially important, to the degree of approximation that is consistent with the inherent uncertainty of the experiments, such interactions can be statistically neglected in the cases of the overall spatial distribution of bubbles, their mean velocity and the root-mean-square of their velocity fluctuations.

Simulations seem to predict slightly smaller opening angles of the bubble jet at large distances from the injection point. It is not clear if this could be attributed to an extra overspreading of bubbles due to the stagnation disk or some other spurious effect of the injection of bubbles in the stage prior to microgravity. In any case, one should take into account that the boundary of the turbulent jet cannot be well described within the frame of a k-ε model, because the latter implies a smooth variation of the properties k and ε, while in reality the transition is an abrupt change from turbulent ($k > 0$) to laminar ($k = 0$) that fluctuates over time. The average effect on the bubble dispersion and velocity statistics displayed by bubbles near the jet boundary is likely to be missed by this simple model. A detailed simulation of the evolution of the fine structure of turbulence would be
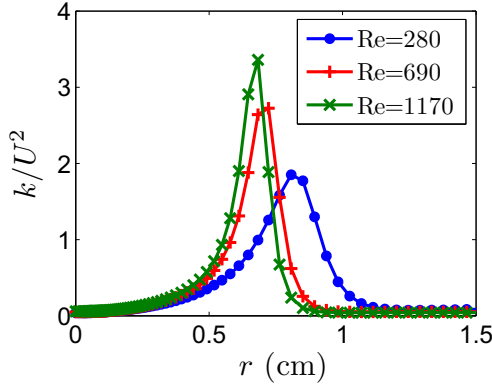
Figure 3.18: Profiles of k/U^2 in function of the radial distance, at x=3cm
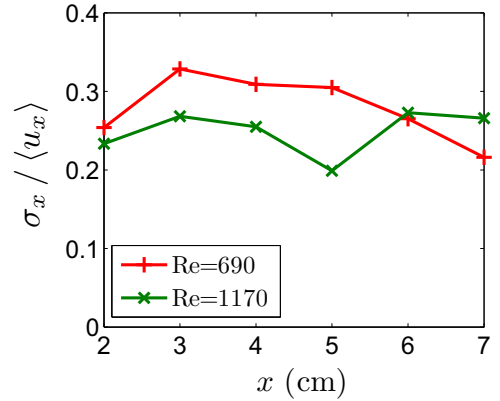
Figure 3.19: Experimental measures of relative velocity fluctuations at the edges of the bubble jet

necessary in order to improve the description and be able to draw the eddies that give shape to the boundary of the turbulent jet.

In fact, when looking at the diffusion coefficient k^2/ε in Fig. 3.7 we find a fast decay of this magnitude in a narrow distance, but this is still a smooth spatial variation and, even more important, constant in time. It is not surprising to find deviations from the prediction of the model in the experimental observation made on the margins of the jet.

One way of interpreting the position of the boundaries of the jet is by considering that all the turbulence properties become negligible after they decay past to a certain threshold value. In Fig. 3.18 we show the relative fluctuations of the flow for three simulations with different degrees of turbulence. If we argue that the flow becomes laminar when the relative fluctuations of the flow (k/U^2) drop below a certain value, then we can see on the figure a tendency to increase the radial distance of the boundary layer (i.e., the angle of the turbulent jet) when decreasing the Reynolds number. We find the same tendency if we define the boundary of the bubble jet at some intrinsic property of the curve, for instance its inflexion point. In fact, in this case we also find that the relative fluctuations of the velocity at this position (which describes the margin of the jet) increases with the Reynolds number.

However, Carrera et al. (2008) measured the opposite result, finding that the bubble jet (measured really close to the injector) increases with Re until it saturates to a fixed value for $Re \approx 700$. In Fig. 3.19 we show the relative fluctuations of the bubble velocities measured experimentally on the bubbles at the margins of the bubble jet. The bubbles taken in order to find these statistics have been carefully selected one by one, in an effort to minimize the effect of averaging bubbles at different depths on the visual direction z. The figure show a weak decreasing

tendency of the relative velocity fluctuations of bubbles at the boundaries when increasing the Reynolds number, which is also contrary to the numerical simulations of the k-ε model. That shows the limitations of this model to describe that kind of details of the flow, and for that purposes it would be necessary the use of more elaborated CFD simulations, able to describe the details of the turbulent structure, a problem that goes much beyond the scope of the present study.

A more accurate description of the system should also aim at a more realistic modeling of the bubble trajectories. Diffusive trajectories are indeed too erratic on small scales and overestimate significantly the probability of bubble encounters. Introducing a more realistic tracking of the flow trajectories, even if still as passive tracers, should take into account statistical correlations of the flow which would clearly modify the statistics of bubble encounters. This point has remarkable practical relevance because reducing the degree of bubble coalescence is important to keep the monodispersivity of the suspension, and ultimately the control of the surface-to-volume ratio. Our jets do exhibit a remarkably low degree of bubble coalescence, a point that was already discussed by Carrera et al. (2008). A full description of the dynamics of suspensions of spherical bubbles, including bubble-bubble interactions and bubble-flow interactions could be approached with large scale Lattice-Boltzmann simulations, in the spirit of the work of Yin et al. (2006). In the case of bubble jets, however, the non-homogeneous conditions along the jet makes this analysis very demanding. It is particularly difficult to incorporate correctly the physics of the two-phase flow right at the exit of the injector, where bubbles may significantly deform due to the strong slowing-down as they enter the cavity, and the variations of the flow field are strong at the scale of bubbles. There the problem is that of turbulent multiply connected free-boundary problem of great numerical difficulty. In the following chapter, we address a simpler situation, with more homogeneous turbulent conditions and bubbles that remain essentially spherical. There a Lattice-Boltzmann approach will be used to characterize the flow trajectories.

Chapter 4

Bubble suspensions in turbulent duct flows

4.1 Introduction

Homogeneous bubbly flows with controlled bubble size have been largely studied in the past in the case of normal gravity conditions [Kytömaa (1987); Tryggvason et al. (2006); Mazzitelli et al. (2003)]. However, there is a lack of experimental data or bibliography for this kind of flows in microgravity. This is mainly due to the large cost of microgravity experimentation, which constrains and slows the scientific progress in reduced-gravity research. Furthermore, the technological challenge to generate bubbles of uniform size without the help of buoyancy forces have been an added difficulty. Colin et al. (2001) studied the distribution of bubbles of 0.92 mm of diameter in a turbulent pipe of 4 cm diameter. They generated them by injecting gas from an hypodermic needle of 0.15 mm diameter into a box where a very low rate of liquid co-flow detached the bubble. Nevertheless, although this procedure allows to generate bubbles with a very precise and controlled size, it also creates them at a low rate, which does not allow the type of study of interaction between ensembles of bubbles and turbulence that we aim at here.

Similarly, in the domain of microfluidics there are well known mechanisms to generate perfectly monodisperse bubbles that would perform adequately in microgravity (see for example [Gordillo et al. (2004)]). However, the low void fraction of gas injected with these procedures makes them also insufficient for the technological challenges that motivated our investigations, like life support systems and environmental control for life in space. Even if a sufficiently large rate of microbubbles of around 100μm could be achieved, they would essentially be point-like with respect of the scales of turbulence and their influence on the
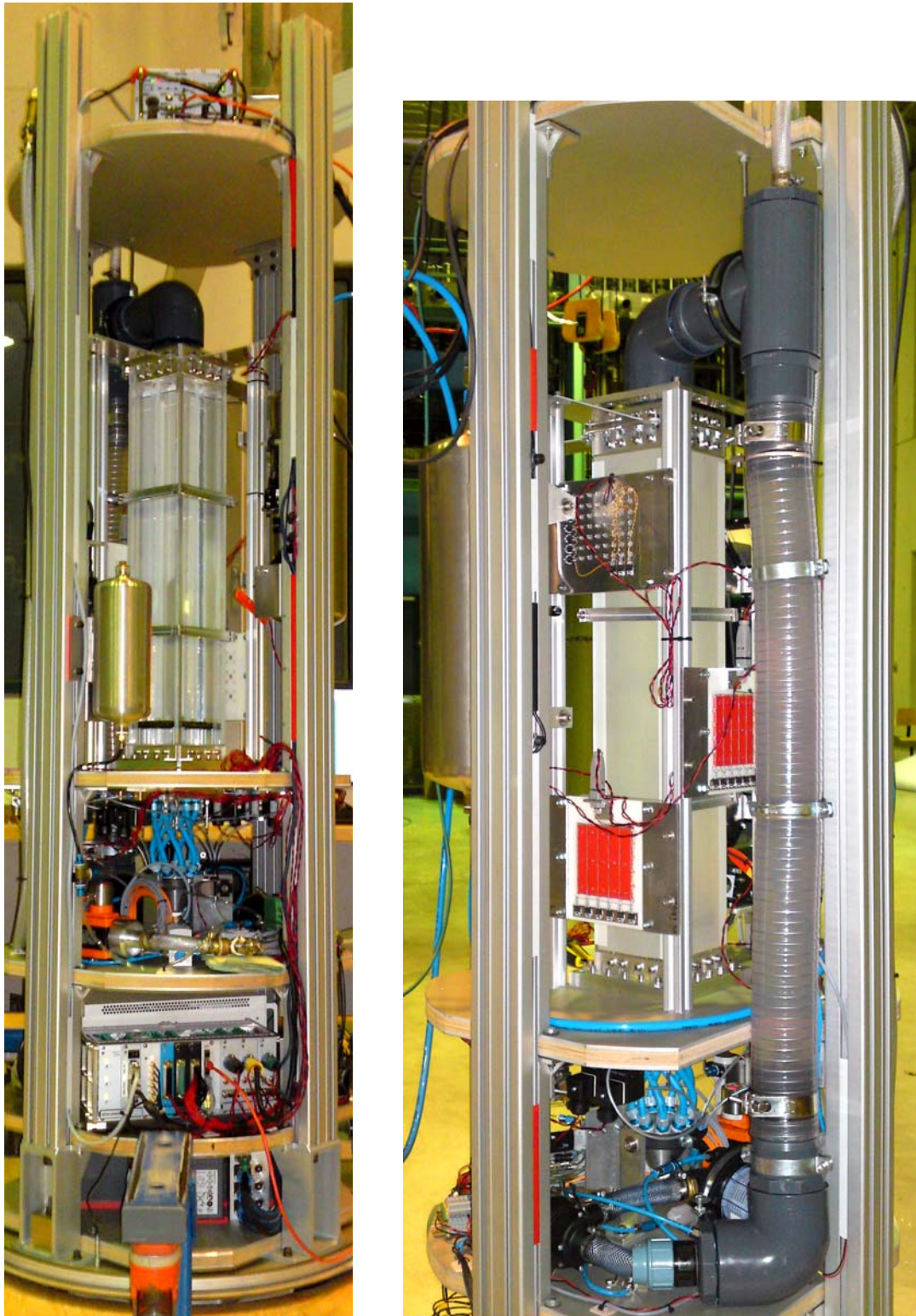
Figure 4.1: Front and back view of the experimental setup

flow would in principle be negligible, so the fundamental interest of turbulent suspensions would also be missed. Hence aim at having bigger bubbles in order to study some significant interactions between them and turbulence.

In this chapter we will present a series of experiments that were conducted in the ZARM Drop Tower (Figure 4.1). The aim is to achieve, for the first time, a homogeneous suspension of monodisperse bubbles of prescribed size, carried by a turbulent co-flow, as a simple model system where interaction between bubbles and turbulence in the absence of buoyancy may be studied experimentally and compared to numerical simulations. The experiment was designed to control separately the bubble size (in the range of mm), the bubble density (in the range of few percents of void fraction, to allow for particle tracking techniques and to avoid coalescence) and the degree of turbulence of the carrying flow (in the range of $Re \sim 10^3 - 10^4$). For suspensions of air in water, these parameters imply sufficiently small Weber number to ensure that bubbles were essentially non deformable (spherical), an important simplification of the problem. They also imply that the bubble size is larger than the Kolmogorov length, to allow for nontrivial effects on the flow, and at the same time smaller than the largest eddies. The small void fraction also ensures that the bubble mean separation is comparable to the most energetic eddies, thus favoring efficient spatial dispersion while avoiding coalescence phenomena. To this aim we designed a combination of 4 independent T-Junctions with capillary diameters $d_T = 1.6$ mm to generate uniform slug flows, and inject them into a vertical duct of 800 mm long and square section of 100x100 mm^2. These dimensions were fixed by the physical conditions of the experiment together with the available time of microgravity of 4.71 seconds of the ZARM Drop Tower. In this channel, a turbulent co-flow drags and disperses the bubbles from their point of injection. Bubbles typically travel distances comparable to the duct length during the duration of microgravity conditions. Unlike the bubble jets of chapter 3, in this setup the degree of turbulence of the carrying flow is independent of the injection parameters that define the conditions of bubble generation. The latter can now be used to modulate to some extent the rate of bubble formation and their size. Our setup cannot reach large void fraction of bubbles under the nominal conditions of performance of our T-junctions. The natural way to extend our setup in that direction would be to increase the number of injectors.

Images taken from high speed video cameras allow us to study the bubble trajectories in space and their instantaneous velocities during the microgravity experiments. In addition to the study of steady flow conditions, an interesting aspect of this setup is that it allows us to study the decay of the so-called pseudo-turbulence. This term designates the turbulence created by the inherent instability of the flow, generated by ensembles of bubbles rising under normal gravity conditions. Our experimental protocol starts with the creation of such flow, that
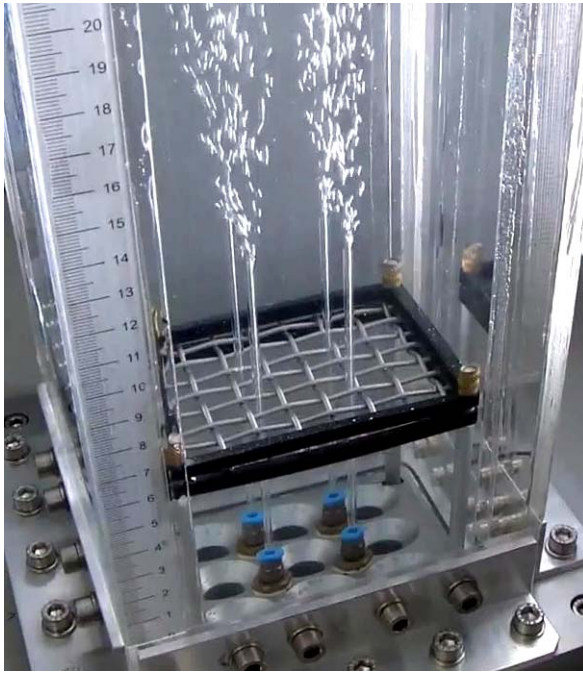
Figure 4.2: Base of the experimental channel while injecting bubbles from the 4 injectors

Figure 4.3: Manifold to split the main liquid flow into 9 lines

induces some degree of turbulence even in the absence of a carrying co-flow. In microgravity, instead, bubbles will only rise due to the drag of the co-flow, so the flow created by the pseudo-turbulence prior to the start of the microgravity conditions will have to decay in a finite time. We can thus characterize the decay of this pseudo-turbulence.

An important focus of interest of the experiment is the study the velocity fluctuations of bubbles for different degrees of turbulence (essentially for two different Reynolds numbers) and compare the results with numerical Lattice-Boltzmann simulations of the turbulent flow. Finally we will briefly address the statistics of trajectories, to gain insights on the mixing properties of the flow and the probability of bubble encounters. In particular we will compare the characteristic times of separation between pairs of bubbles on the experiments with pairs of passive tracers in the Lattice-Boltzmann simulations.

4.2   Experimental setup

4.2.1   General description

The main practical objective of the project is to achieve for the first time, a controlled homogeneous distribution of monodisperse bubbles within a turbulent flow.

To this aim we use a vertical duct of square section and dimensions 800x100x100 mm^3. At the base of the channel we inject the carrying co-flow from 9 evenly-spaced inlets that surround the 4 bubble injectors (Figure 4.2). Each bubble injector consists of a T-junction (as the ones described in the previous chapter) with capillary tubes of $d_T = 1.6$ mm which connects to a glass tube of the same inner size, allowing to inject the slug flow directly into the channel at a distance of 150 mm from the base. In this way we grant to the co-flow of some initial space to let it reach a more homogeneous and developed structure of its turbulent flow before it interacts with the bubble jets. In order to accelerate and homogenize the development of the co-flow turbulence, this flows through a wire mesh with square holes of 10x10 mm^2, which corresponds to the characteristic scale of the most energetic eddies in steady conditions in such a duct.

The flow provided by the main water pump is split into 9 lines (one for each inlet in the duct) by using the manifold shown on Figure 4.3. Due to space restrictions inside the drop capsule (Figure 4.4), the main water tube suffers of a sharp 90º bending just before connecting it to the manifold, which produce uneven pressure distribution in the manifold. We corrected this effect by introducing a screw-ring on each outgoing line of the manifold and manually adjusting their tightening on each tube in order to obtain an even flow distribution through all lines. Not correcting this effect would produce longer spatial transients in the duct before the stationary distribution of the flow were reached, and could even produce the occurrence of recirculation flows.

For the generation of bubbles, a second water pump has been used. The flow from there has been distributed into four lines, each one connected to one T-Junction. Similarly, the gas flow has been controlled with a pressure regulator and, after distributing it into the corresponding four lines with another manifold, have also been connected to the T-junctions. In order to obtain a controlled small gas flow for each line, it has been added one precision orifice (of typically 0.0012 in $\simeq 30.5\,\mu$m) at each air line just before the T-junction. These serve to soften large gas pressure variations into small flow changes, providing really controlled gas flows as well as a useful way to decouple the gas lines, achieving a good and independent performance of the four bubble generators.

4.2.2 Pressure compensation system

As seen in chapter 3.3, T-junctions produce the same outcome independently of the degree of gravity due to the negligible effect of the buoyancy forces upon the process of bubble formation and detachment. Nevertheless, in our actual vertical configuration with the injectors located below the large mass of water filling the duct, the sudden loss of hydrostatic pressure when the microgravity conditions
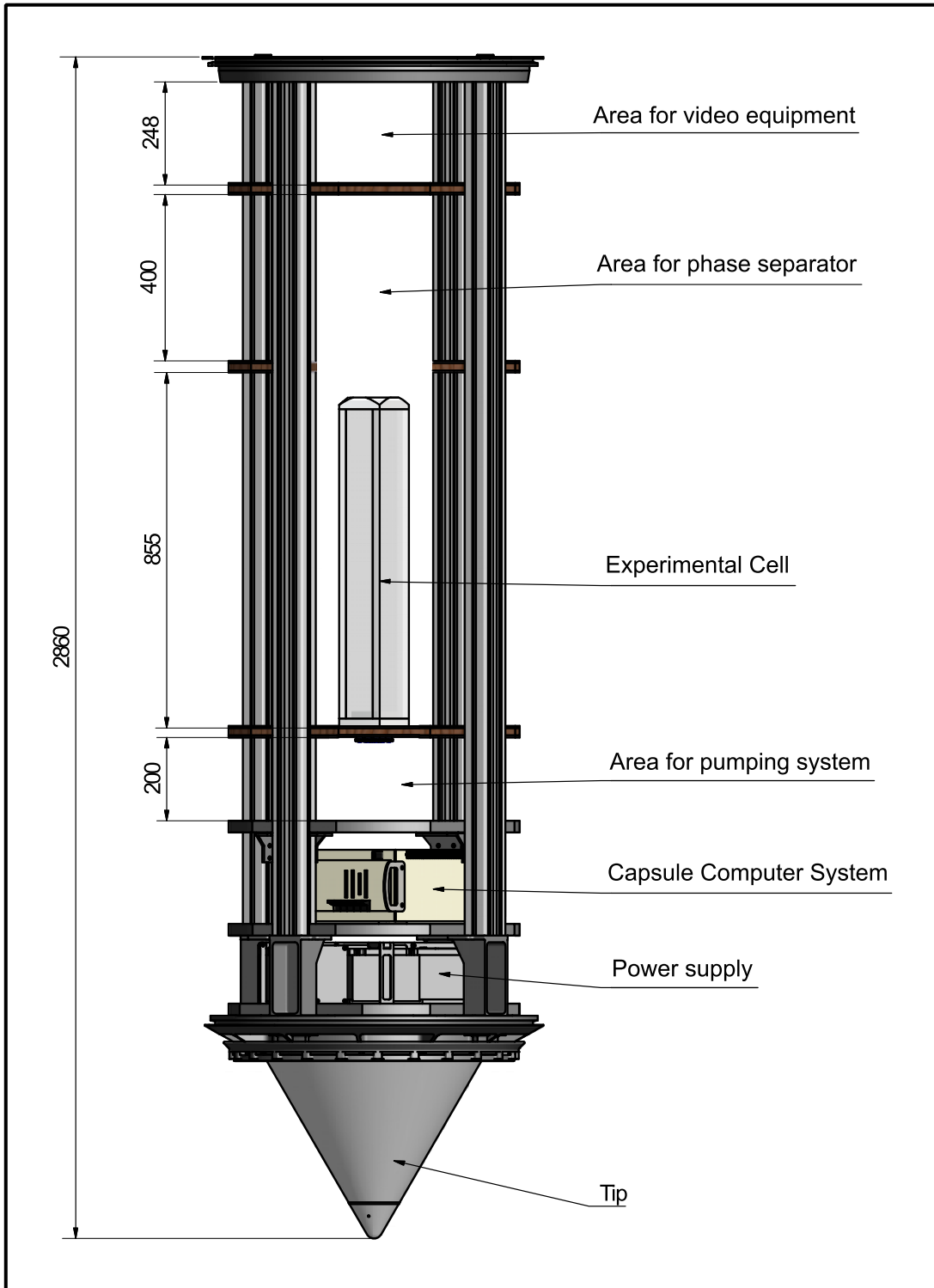
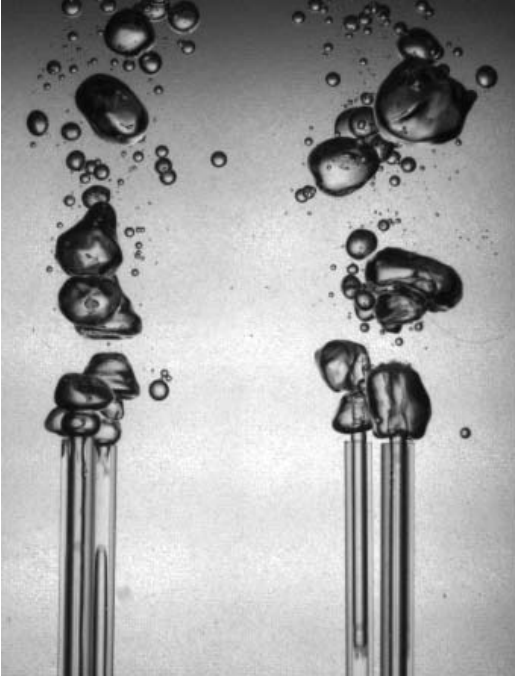**Figure 4.4:** Schematics of the drop capsule

Figure 4.5: Excessive release of pressure due to the loss of hydrostatic pressure. Snapshot taken 0.2 s after the start of microgravity.
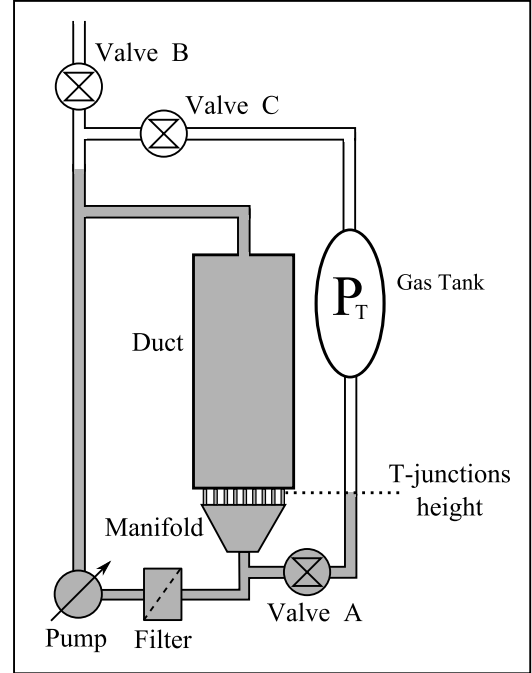
Figure 4.6: Schematics for the co-flow liquid line with the pressure compensation system. Gray areas represent elements filled with water while white ones are filled with air.

switch on, will produce a large instantaneous change in the operating conditions in the T, inducing a transient in its performance that may have a non negligible relaxation time, and that may have a significant effect on the very early stages of the experiment.

The working pressure P of each T-junction in normal gravity conditions is

$$P = P_0 + \rho g h + dP , \qquad (4.1)$$

where P_0 is the reference pressure (i.e., the ambient pressure, supposing that the system is open at the top of the capsule), $\rho g h$ is the hydrostatic term (with h the height of the water column between the points where we measure P and P_0), and finally dP is the extra pressure needed in the capillary tube of the T-junction in order to detach one bubble. When microgravity starts, bubble generators experience the loss of hydrostatic pressure, instantaneously obtaining a new working pressure (P')

$$P' = P_0 + dP , \qquad (4.2)$$

while the gas pressure on its capillary tubes still is $P > P'$. That produces a transient in which the injectors release the excess of gas (Figure 4.5) until they

reach the new working pressure P'.

The method that we have used in order to minimize this effect consists in maintaining constant the working pressure of the T-junction (i.e., $P'' = P$) by increasing the pressure in the whole system during the microgravity conditions. Being P'' the new working pressure during microgravity,

$$P'' = P_0'' + dP \ , \tag{4.3}$$

the new reference pressure P_0'' should be

$$P_0'' = P_0 + \rho g h \tag{4.4}$$

In Figure 4.6 we show the schematics of the main water line for the injection of the co-flow into the experimental channel. The gas tank and the three valves are used in order to compensate the pressure loss in the T-junction during microgravity. The procedure used to this aim is the following:

1. On ground, with valves "A" and "B" open, we regulate the pressure P_T in the gas tank until the water column below it reaches the same height at which the T-junctions are placed. By doing that, we are setting all the air in the tank (and in its connecting tubes) at the same pressure than in the T-Junctions.

2. After adjusting the pressure in the gas tank, valve "A" is closed. From that point on, we can keep working in normal gravity conditions, but only valve "B" should remain open during this period.

3. At the start of microgravity, we close valve "B" and open valve "C" instead. In that way P_T becomes the new reference pressure P_0'' while the hydrostatic pressure disappears. Notice that we have kept valve "A" closed in order to prevent possible co-flow deviations through the gas tank that could happen if valves "A" and "C" were simultaneously open.

4.3   Turbulent duct flow

4.3.1   Analytical characterization

Through the present chapter we will describe the degree of turbulence in a duct flow by means of the Reynolds number, defined as

$$Re = \frac{U_c L_c}{\nu} \ , \tag{4.5}$$

with ν the kinematic viscosity of water, U_c the characteristic velocity of the flow (its mean velocity) and L_c the characteristic size of the system (the width of a transversal section of the channel, i.e. $L_c = 100$ mm). Even though the degree of turbulence in the range of Reynolds numbers studied is only moderate, it is convenient, as a theoretical reference, to consider the values of the relevant scaling parameters of turbulence by using the expressions introduced in chapter 3.2 for fully developed turbulence. We also use the self-similarity relation (3.10) applied to the size of the most energetic eddies λ_{Max} to find their characteristic time τ_{Max}. For the typical flow parameters used in our experiments, corresponding to $Re = 6000$ and $Re = 13000$ we find:

Re	λ_k	$\lambda_{\min}$	λ_{Max}	τ_k	τ_{Max}	T_c
6000	0.15 mm	1.5 mm	10 mm	22 ms	360 ms	1700 ms
13000	0.08 mm	0.8 mm	10 mm	7 ms	170 ms	770 ms

Table 4.1: Scales of turbulence in a duct flow, being λ_k and τ_k the Kolmogorov scales, $\lambda_{\min}$ the size of the smallest eddies, λ_{Max} and τ_{Max} the scales of the most energetic eddies and finally $T_c = \frac{L_c}{U_c}$ the characteristic time of the flow.

Furthermore, as seen on equation (3.16), we find that the response time τ_B of the typical bubbles injected into the channel is

$$\tau_B = \frac{d_B^2}{36\nu} \simeq \begin{cases} 70 \text{ ms}, & \text{for } d_B = 1.6 \text{ mm} \\ 170 \text{ ms}, & \text{for } d_B = 2.5 \text{ mm} \end{cases} \tag{4.6}$$

Comparing the scales of turbulence in Table 4.1 with those associated to bubbles, seen in equation (4.6), we find that $\lambda_{\min} \lesssim d_B \lesssim \lambda_{\text{Max}}$ and $\tau_k \lesssim \tau_B \lesssim \tau_{\text{Max}}$, implying that bubbles may be expected to exhibit an active behavior in relation to the smallest structure of turbulence and, at the same time, not produce major alterations on the main flow or on the most energetic pattern of turbulence.

In addition to this, the typical void fraction ϑ of gas injected into the channel

$$\vartheta = \frac{4Q_g}{4Q_l + Q_{\text{co-flow}}} \leqslant 0.5\% , \tag{4.7}$$

is quite small, pointing in the direction of a limited impact of bubbles into the main structure of turbulence. This value is even smaller for the initial bubbles, which have been injected during normal gravity conditions and for which buoyancy forces have increased the distance between them.

4.3.2   Lattice-Boltzmann simulations

In order to characterize the structure and properties of a turbulent flow through
a duct of square section we have performed 3D Lattice-Boltzmann simulations
as described in chapter 2.2. The channel has been discretized into a uniform
grid of 320x80x80 liquid nodes, representing a portion of 400x100x100 mm^3 of
the duct, with periodic conditions at its ends. Our code have been parallelized
and run in the *Mare Nostrum* supercomputer at the *Barcelona Supercomputing
Center* (calculating typically with a set of 256 processors) and in a cluster of 16
processors at the *Department of Applied Physics* of the *Polytechnic University of
Catalonia* (UPC). An overall estimation of the total CPU time used, accounting
for checking and optimization of the parallelized code as well as for its subsequent
simulations, has been of around 80,000 hours.

Pattison et al. (2009) studied this kind of flow using the generalized lattice
Boltzmann equation in a uniform grid of 432x74x74 nodes for the case of a fric-
tional Reynolds number $Re_* = 300$. They compared their results to experimental
measures as well as to simulations of other authors made using Direct Numerical
Simulations methods and Large-Eddy Simulations based on the filtered Navier
Stokes Equations. In order to check our code, we ran simulations for the same
conditions as Pattison et al. (2009)[1] and found that the results coincide reasonably
well, except for small asymmetries product of insufficient temporal averaging. We
also ran a simulation with $Re = 12700$ in order to compare it with our experimen-
tal measures as well as to be able to contrast two different degrees of turbulence.

In Figure 4.7 we compare the computed flow in a transversal section of the
duct for the cases with Reynolds numbers of 3800 and 12700. Lines represent the
fluctuating component of the flow velocity ($\mathbf{u}' = \mathbf{u} - \mathbf{U}$). Length and color of the
lines show the magnitude of each vector in an arbitrary scale. In Figure 4.8 the
same comparison is made for the longitudinal section of the flow placed at midway
between walls in the z direction. In both figures, for higher Reynolds numbers a
finer and more detailed structure of turbulence may be appreciated, that includes
smaller eddies. Also, a higher degree of turbulence near the walls, in relation to
the central area of the duct, can be appreciated in all cases.

---

[1]Imposing the forced term as described by Pattison et al. (2009) to reach $Re_* = 300$ we found
that this flow corresponds to $Re = 3800$. Similarly, when imposing $Re_* = 950$, we obtained a
flow with $Re = 12700$, which is close enough to the value of our experimental measures in the
case of maximal co-flow injection.
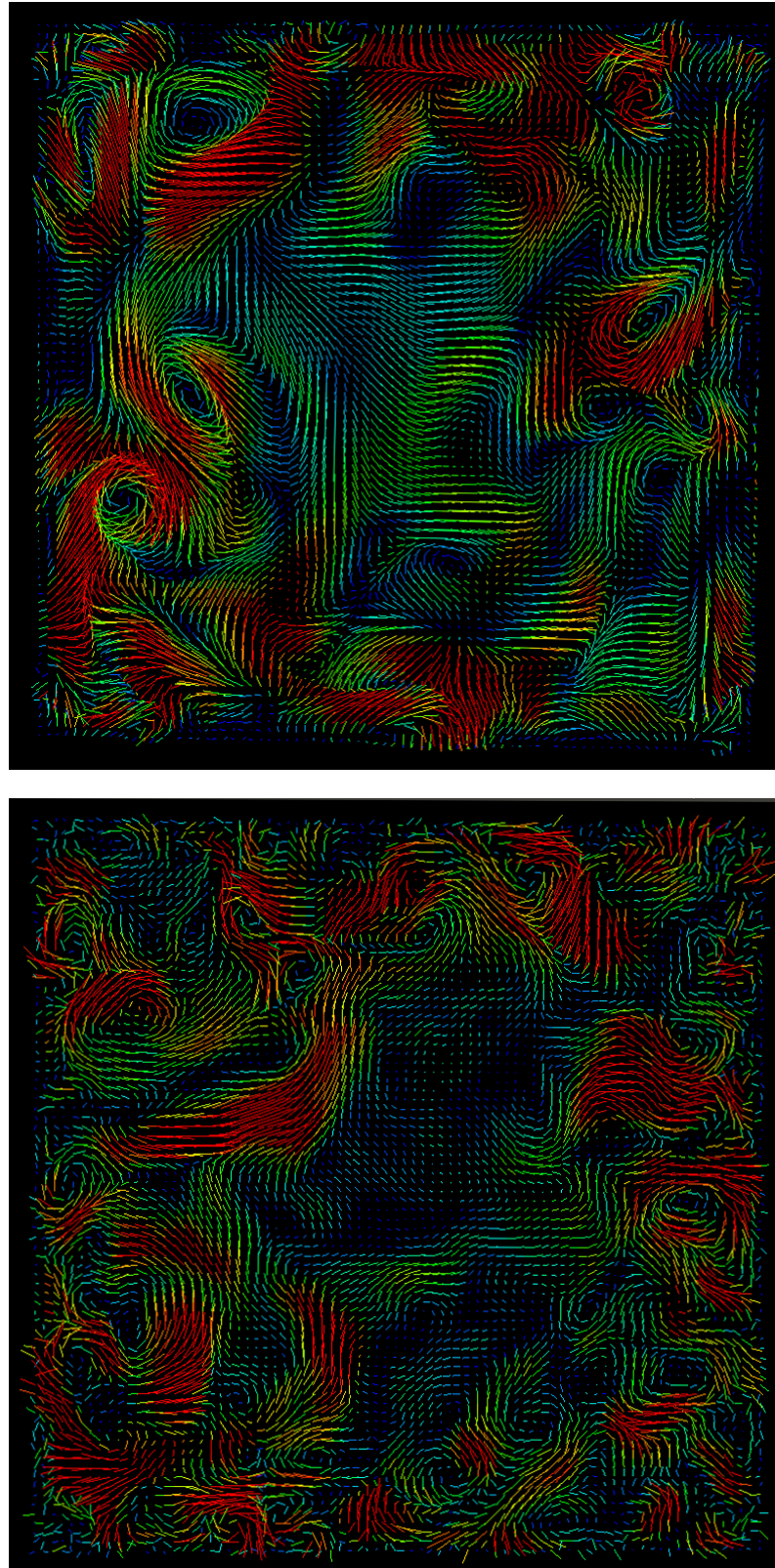
Figure 4.7: Transversal sections of the turbulent flow. Lines represent the fluctuating component of the flow velocity $\mathbf{u}'$. *(Above): Re=3800. (Below): Re=12700.*
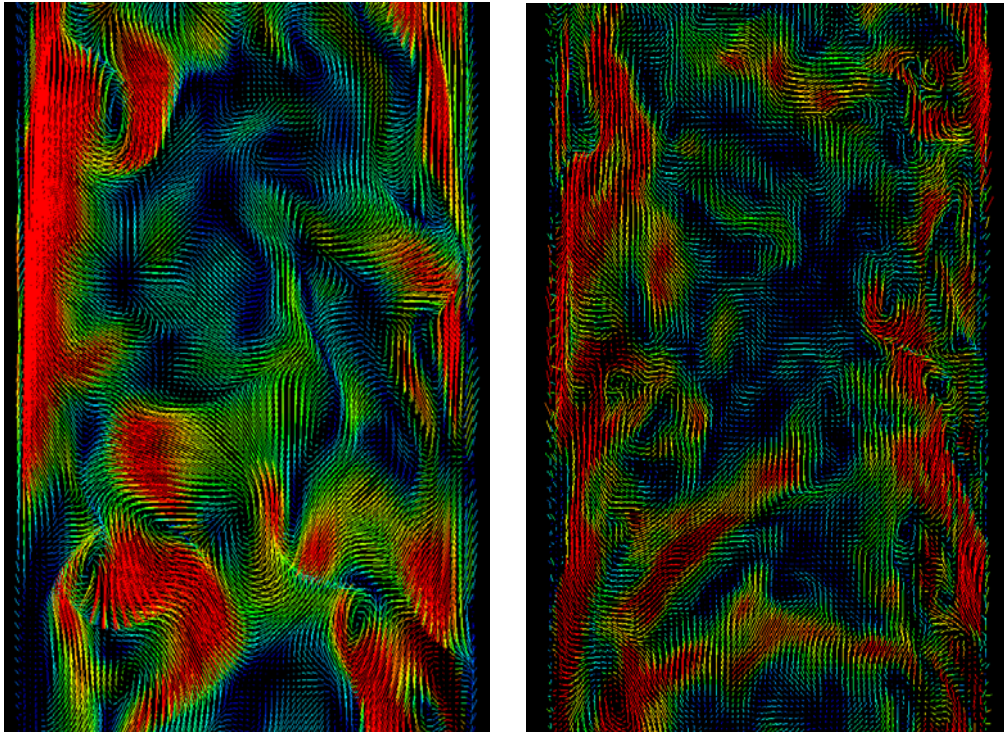
Figure 4.8: Velocity fluctuations $\mathbf{u}'$ on a longitudinal section of the duct flow at $z = 0.5L_c$. Flow goes upwards. *(Left): Re=3800. (Right): Re=12700.*
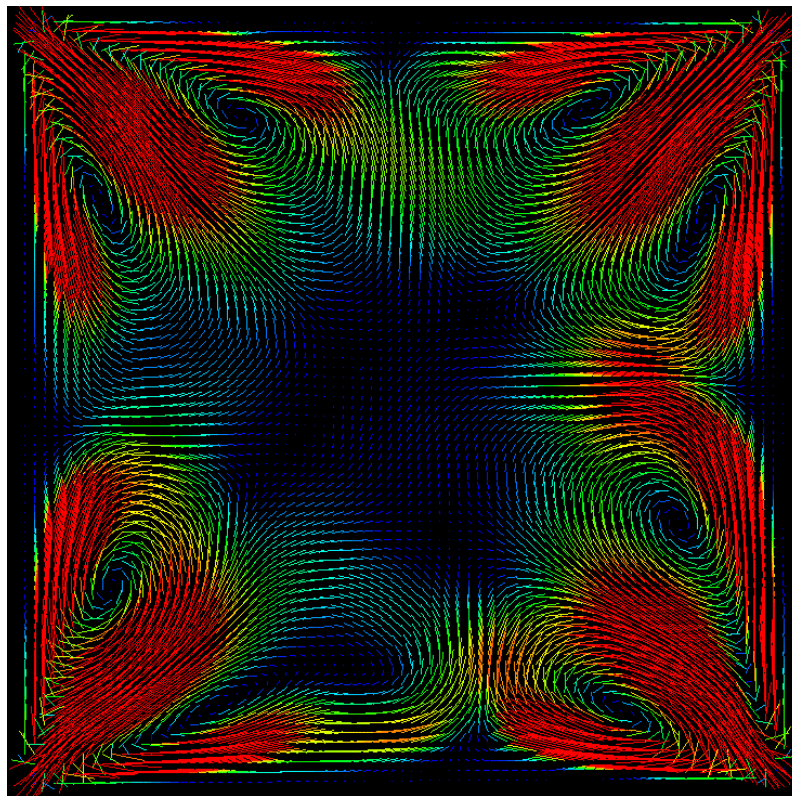

Figure 4.9: Mean secondary flows on a transversal section of the duct for $Re = 3800$
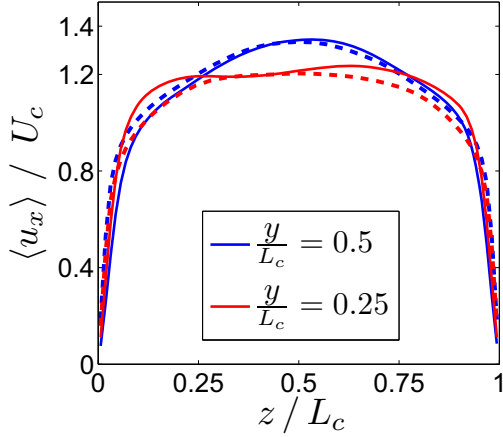
Figure 4.10: Profiles of mean velocity component $\langle u_x \rangle$ at different sections y/L_c. Solid lines correspond to $Re = 3800$ while dashed ones stand for $Re = 12700$
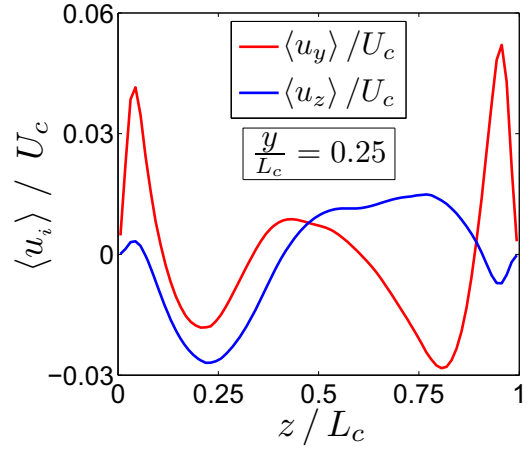
Figure 4.11: Profiles of mean velocity components $\langle u_y \rangle$ and $\langle u_z \rangle$ for $Re = 3800$ at the section $y/L_c = 0.25$

As measured by many authors (see for example [Melling and Whitelaw (1976)]), and in contrast to the case of pipe flow with a circular section, turbulent flow in a square duct generates a weak remnant mean flow contained in the square transversal plane of the flow, with pairs of symmetric vortices on each of the four edges of the channel. Those are called secondary flows, as they have a magnitude significantly smaller than the main longitudinal flow, and emerge only after careful time averaging of the transversal flow. Their structure is such that flow approaches the edges from the bisector of the right angle between walls, then it follows the wall (moving really close to it) until it approaches the bisector of the wall, where it returns to the central part of the section. In Figure 4.9 we show the mean secondary flows obtained in our computations for the case of $Re = 3800$. Lines represent the flow vector $(0, U_y, U_z)$, being the length and color of the lines, the magnitude of the vector in an arbitrary scale. Results have been obtained from averaging over the whole length of the simulation, and over a period of 400,000 iterations (corresponding to 500 s of simulated time for the parameters of our experimental duct) after the simulation had reached the stationary regime. Given the difficulty of observing such secondary flows, they constitute a good test of the numerical simulation.

Analogously, we have done a statistical analysis for the computation with $Re = 12700$, averaging over a period of 300,000 iterations (corresponding, in our case, to 110 s of simulated time) after reaching the stationary solution of the flow. Comparing the numerical results obtained from both simulations in Figure 4.10 we find that the dimensionless profiles of velocity remain essentially unaltered by the change in the degree of turbulence in the flow. This is in agreement with the
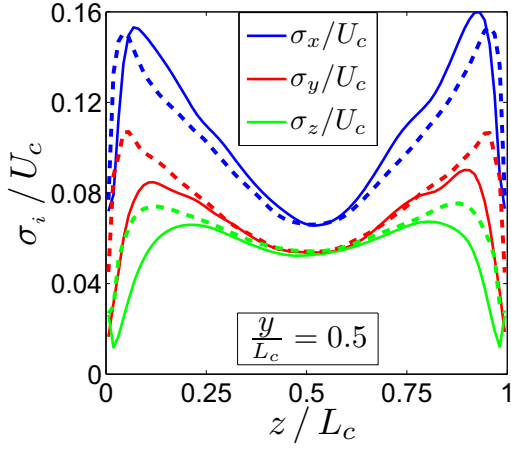
Figure 4.12: Profiles of velocity fluctuations σ_i, at the section $y/L_c = 0.5$. Solid lines correspond to $Re = 3800$ while dashed ones stand for $Re = 12700$

Figure 4.13: Profiles of velocity fluctuations σ_i, at the section $y/L_c = 0.25$. Solid lines correspond to $Re = 3800$ while dashed ones stand for $Re = 12700$
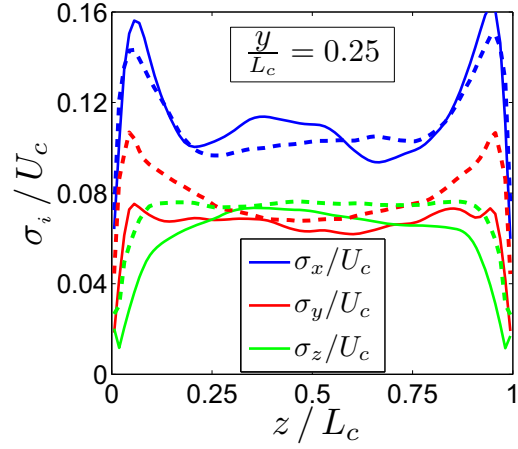
scaling picture of turbulence described in chapter 3.2, to the extent that the main structure of the flow is determined by the largest scales of turbulence, while the smaller ones define the scale of dissipation. The increase of the Reynolds number produces the decrease of the smallest scales of turbulence, resulting in the addition of more scales of velocity fluctuations that alter the fine detailed properties of the flow, while the large scale structure remains unaffected.

In Figure 4.11 we show the secondary components of the mean flow velocity for one of the simulations. It is easy to attribute the origin of the apparent asymmetries to the secondary flows of Figure 4.9, which would still require further statistical averaging to achieve convergence. Nevertheless, the figure is still interesting in order to realize the order of magnitude of the intensity of the secondary flows in relation to the main flow.

As a last overview of the properties of the computed flow, we study now the profiles of its relative velocity fluctuations. We define σ_i as the root-mean-square of the velocity fluctuations of the component i of the flow:

$$
\begin{cases}
\sigma_x = \sqrt{\langle u_x'^2 \rangle} = \sqrt{\langle u_x^2 \rangle - \langle u_x \rangle^2} \\[2mm]
\sigma_y = \sqrt{\langle u_y'^2 \rangle} = \sqrt{\langle u_y^2 \rangle - \langle u_y \rangle^2} \\[2mm]
\sigma_z = \sqrt{\langle u_z'^2 \rangle} = \sqrt{\langle u_z^2 \rangle - \langle u_z \rangle^2}
\end{cases}
\tag{4.8}
$$

In Figures 4.12 and 4.13 we show these profiles taken at depths $\frac{y}{L_c} = 0.5$ and 0.25, respectively. In both cases we compare the relative fluctuations on each
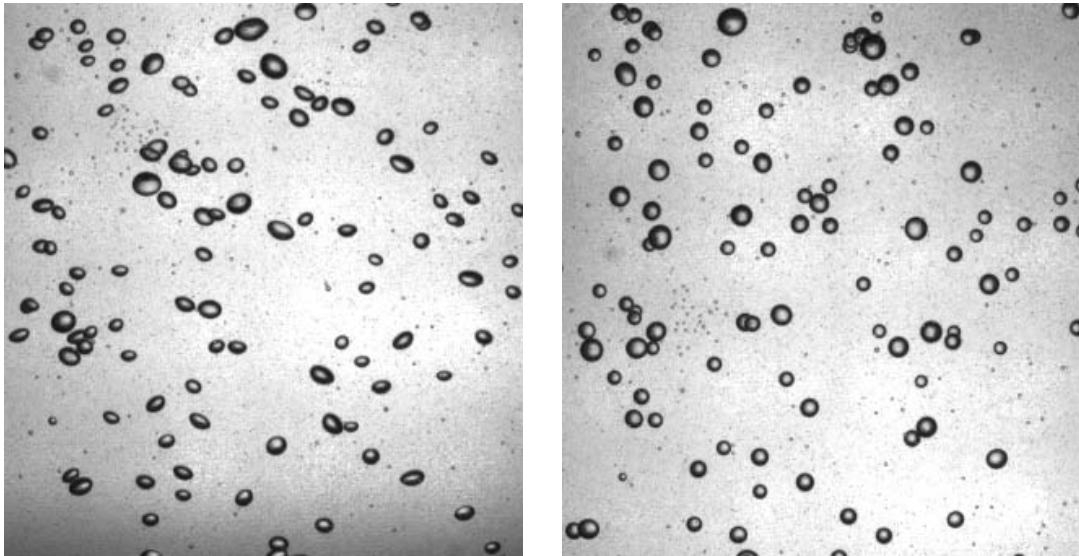
Figure 4.14: Snapshots of the same ensemble of bubbles in deionized water. *(Left):* Elongated bubbles in 1*g*. *(Right):* Spherical bubbles in μ*g*, 0.2 s after the other picture.

direction and for different degrees of turbulence. It can be seen that changing the Reynolds number has no significant effect upon the relative velocity fluctuations, which is consistent with the scaling arguments.

4.4 Experimental results

4.4.1 Qualitative description

When we inject bubbles during normal gravity conditions, they are strongly accelerated by buoyancy forces and rise through the channel following either helical or zig-zag trajectories [Wichterle et al. (2009)]. In their path, they drag the liquid on their surroundings, inducing velocity fluctuations that can be either dissipated by viscosity or strongly enhanced by cooperative interaction between collections of bubbles, up to scales of movement much larger than the size of the bubble, creating what is known as pseudo-turbulence [Mazzitelli and Lohse (2009)].

In our experimental setup we have recorded the experiments using 4 high speed video cameras: one capturing the bubble injectors, another filming the area roughly at the center of the duct, and two more at the end of the channel, recording it from two perpendicular directions. In Figure 4.14 we show two snapshots of an experiment performed with de-ionizated water where the slight deformability of bubbles of our typical size in the presence of buoyancy forces can be appreciated. These deformability has also a relevant role in the vicinity of the injectors, where bubbles suffer strong oscillations of their interphases due to the sudden

deceleration that they experience and to the large gradients of flow velocity affecting them in that region. From previous experience with similar injectors and in other microgravity environments, such as parabolic flights, it seems that such oscillations enhance significantly the rate of bubble coalescence right at the cavity inlet, a complex phenomenon that could have several origins, including possibly the resonances between the bubble oscillatory modes and the frequency of bubble formation, which may be of the same order. We will not pursue this effect in detail here, and we will rather focus our analysis in the case of bubbles of filtered air in water with some degree of saline concentration. Specifically, and in order to have large amount of water under the same solutal conditions, we used commercial mineral water[2]. The presence of a minimal amount of solute in the liquid has several important effects: it increases the surface tension, making the bubbles more spherical; it produces a no-slip boundary condition at the gas-liquid interface; and it significantly decreases the probability of coalescence when bubbles collide.

The vertical injection of bubbles from our four glass tubes creates four roughly cylindrical columns of rising bubbles that interact strongly and follow complex oscillatory rising paths. The strong buoyancy forces and the pseudo-turbulence generated in the neighborhood of the bubbles, confine them in these columns regardless of the degree of turbulence inherent in the duct co-flow. However, once the buoyancy is switched off, bubbles quickly decelerate and relax to the local liquid flow velocity within their viscous relaxation time. In a similar time scale, the flow becomes more homogeneous and bubbles spread to fill the whole channel. Even though some remnants of the pseudo-turbulence may have longer relaxation times, the time scale of the experiment is sufficient to observe the emergence of a steady regime dominated by the co-flow.

A substantial increase of the density of bubbles is observed when those that have been first injected at the beginning of microgravity phase of the experiment reach the area of observation of the different cameras. That is because bubbles injected during normal gravity conditions, despite being generated at the same frequency by the T-junctions, acquire a finite velocity with respect to the carrying flow, due to buoyancy forces, implying that mean separation between bubbles is larger. On the contrary, bubbles injected in microgravity disperse to a density only dependent on the injection parameters, as previously seen in equation (4.7).

In Figures 4.15 and 4.16 we show some representative snapshots of the characteristic situations described above, for two bubble sizes: $d_B = 1.6$ mm and 2.5 mm, respectively. For both figures, cases a and b compare the performance of the injectors in normal gravity and in microgravity. Case c shows the distribution of

---

[2]Ionic content in mg/l are: Na^+ (16.4), K^+ (2.4), Mg^{2+} (51.4), Ca^{2+} (184.5), Cl^- (45.7), SO_4^{2-} (411.2) and HCO_3^- (278.5)
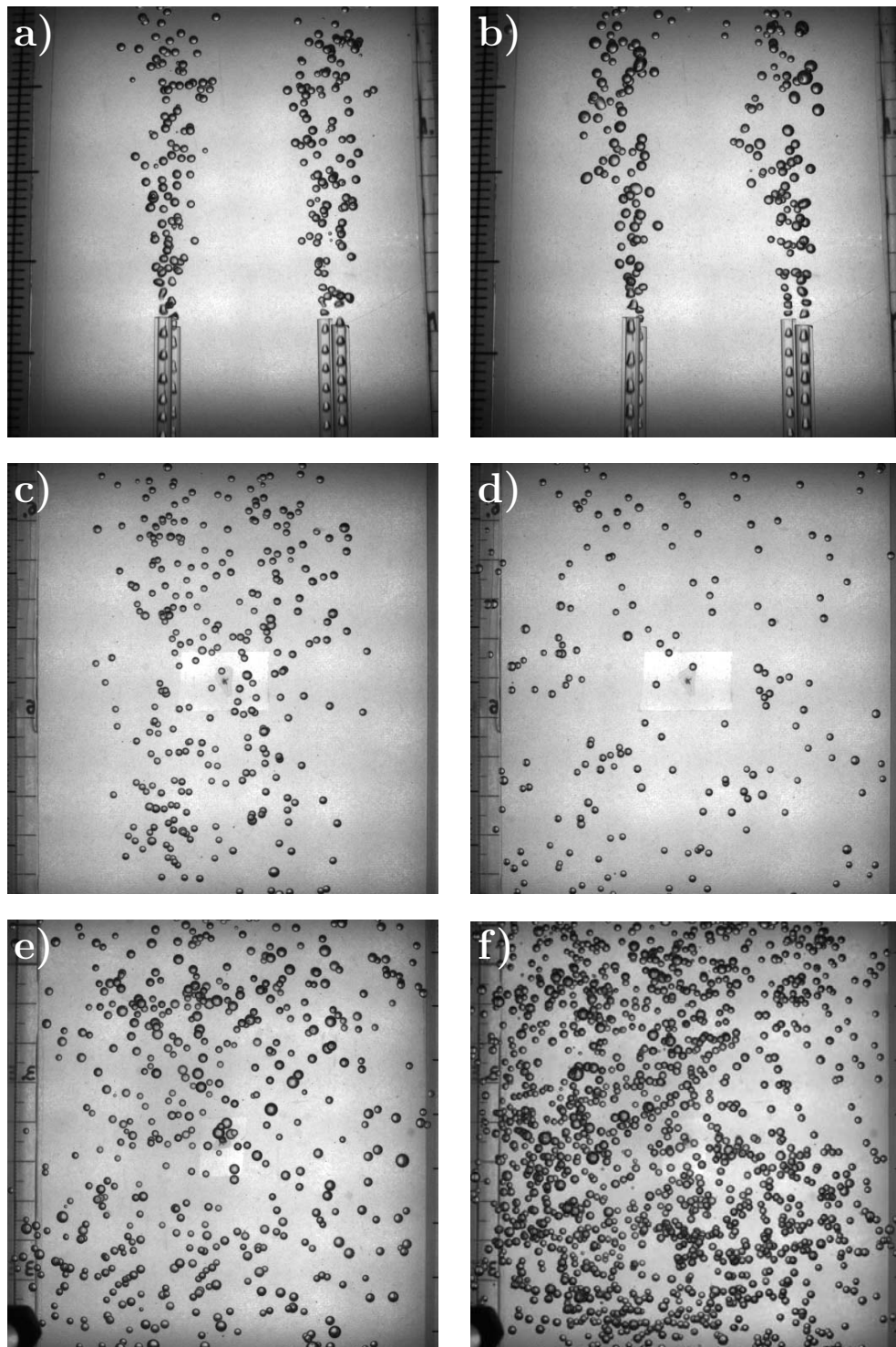
Figure 4.15: Snapshots for experiments with $Q_l = 70 \frac{\text{ml}}{\text{min}}$ and $Q_g = 46 \frac{\text{ml}}{\text{min}}$ ($d_B \simeq$ 1.6mm) from each injector. Cases *(a)-(e)* correspond to $Re = 13000$, while *(f)* is for $Re = 6000$. *(a):* Injection in 1g. *(b):* Injection in μg. *(c):* Bubbles in 1g. *(d):* Bubble suspension in μg of bubbles injected during 1g conditions. *(e)&(f):* Bubble suspension of bubbles already injected in μg conditions
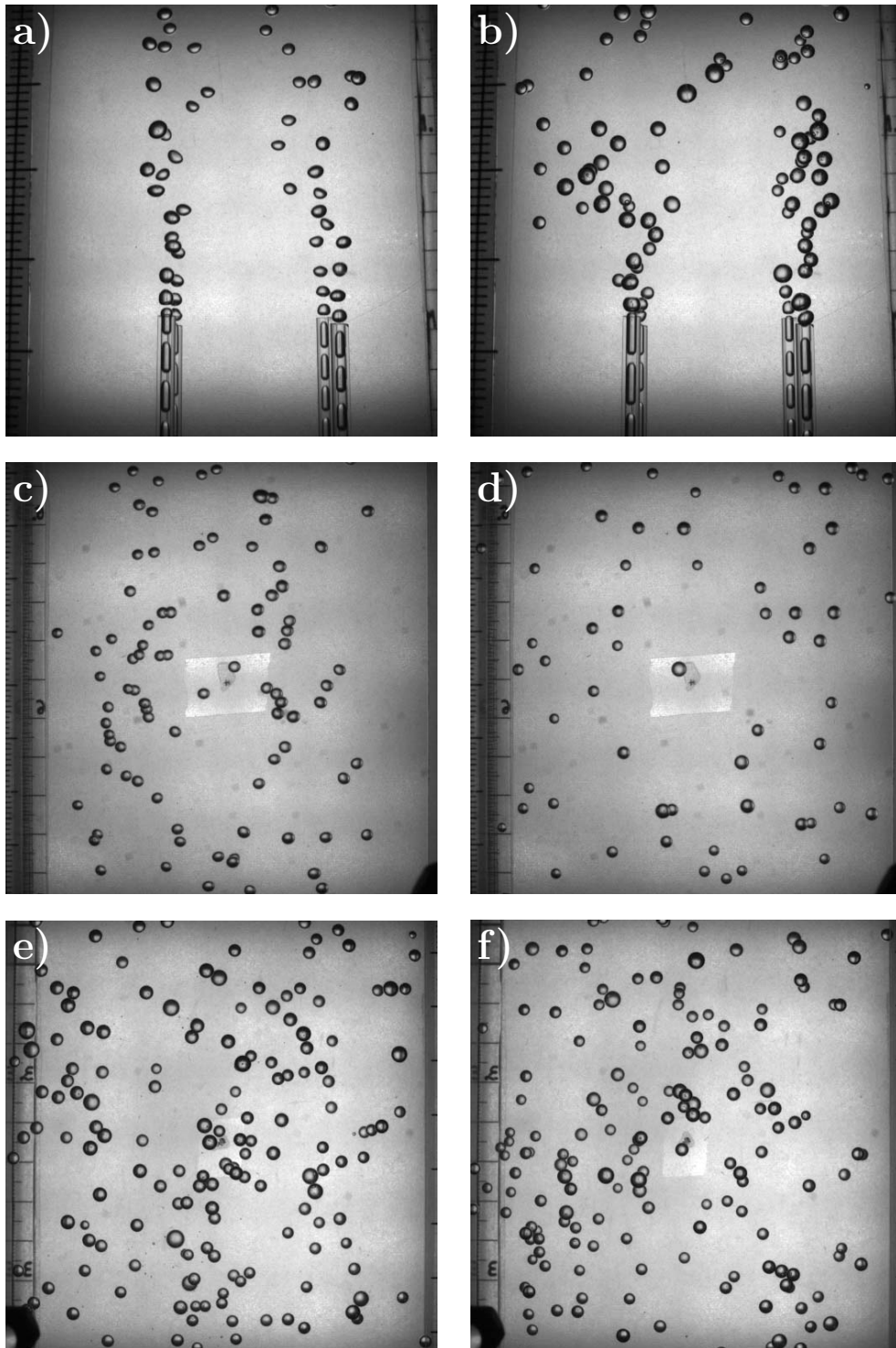
Figure 4.16: Snapshots for experiments with $Q_l = 18\frac{\text{ml}}{\text{min}}$ and $Q_g = 46\frac{\text{ml}}{\text{min}}$ ($d_B \simeq$ 2.5mm) from each injector. Cases *(a)-(e)* correspond to $Re = 13000$, while *(f)* is for $Re = 6000$. *(a):* Injection in 1g. *(b):* Injection in μg. *(c):* Bubbles in 1g. *(d):* Bubble suspension in μg of bubbles injected during 1g conditions. *(e):&(f):* Bubble suspension of bubbles already injected in μg conditions

#	Q_l (ml/min)	Q_g (ml/min)	$Q_{\text{co-flow}}$ (l/min)
D1	75	34	35
D2	30	16	35
D3	70	51	80
D4	70	51	35
D5	37	19	80
D6	70	46	35
D7	70	65	77
D8	70	46	81
D9	18	46	81
D10	70	46	81
D11	18	46	81

Table 4.2: Parameters of injection correspondent to the experimental drops used for the data analysis in the present work. Q_l and Q_g stand, respectively, for the liquid and gas flow rate injected at each one of the four equivalent T-junctions. Q_{coflow} is the total liquid flow rate through the nine inlets

bubbles in normal gravity conditions. Despite that they have risen a distance of nearly 60 cm within a turbulent flow, it is easy to see how they still remain confined at the central part of the duct due to the buoyancy forces. Case *d* shows the distribution of bubbles at the same distance in microgravity conditions, after the spreading of bubbles takes place. Finally, cases *e* and *f* show the higher density of bubbles achieved when those that have been injected in microgravity reach the observation areas. Density is even bigger in *f*, due to its slower co-flow.

4.4.2 Statistical analysis

As we did in the previous chapter, we process the images taken from the video cameras to highlight the bubbles interphase and then we use a Particle Tracking software to identify the paths described by all the bubbles in the recordings. The injection parameters for the cases analyzed are listed on Table 4.2.

For experiments of isolated bubbles it would be possible in principle to reconstruct their three-dimensional trajectory from the data extracted of the pair of video cameras that simultaneously film at perpendicular planes of the duct. In practice, however, this is not possible in our case due to the large number of bubbles, implying a high degree of screening and the inherent difficulty of matching the bubble identities in corresponding snapshots. Therefore, as in the previous chapter, we are not able to measure the components of position and velocity over the visual direction z, perpendicular to the pictures. In the data analysis it is thus necessary to take into account that local fields at positions (x, y) are in fact
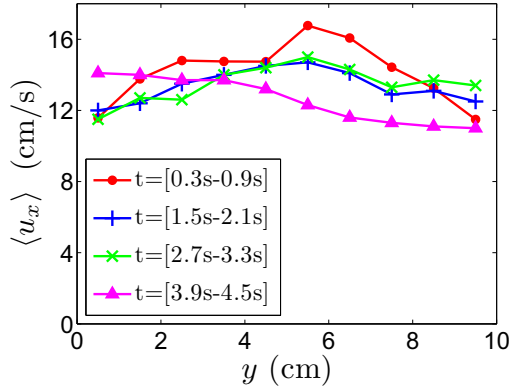
Figure 4.17: Profiles of mean velocity of bubbles $\langle u_x \rangle$ at various times of the experiment for a single realization (D8) with $Re = 13000$
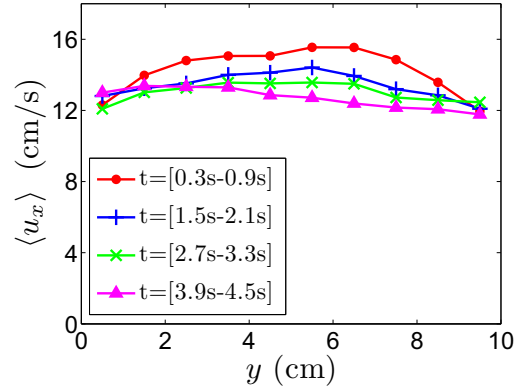
Figure 4.18: Profiles of mean velocity of bubbles $\langle u_x \rangle$ averaged over the measures of 4 different cameras of two equivalent experiments (D8+D10) at $Re = 13000$, at various times of the experiment
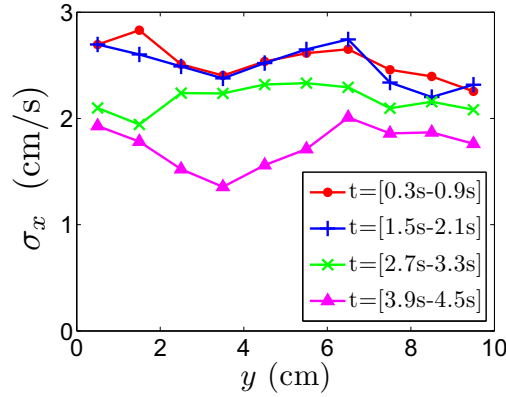
Figure 4.19: Profiles of velocity fluctuations σ_x of bubbles averaged over the measures of 4 different cameras of two equivalent experiments (D8+D10) at $Re = 13000$, at various times of the experiment

averaging properties in regions that may be significantly different, like regions far or near the sidewalls.

For the following figures we have performed a statistical analysis of the bubble velocity in the duct. We have averaged their velocity on each point over temporal intervals of 0.6 s (being $t = 0$ the beginning of microgravity). In addition to this, we have also averaged over the direction of the main flow (x), assuming it to be homogeneous for the relatively small distance contained in the observation field of one video camera (around 10 cm).

In Figure 4.17 the profiles of mean velocity of bubbles are displayed for a typical realization with $Re = 13000$ and bubble size $d_T = 1.6$ mm. The irregularities

shown in those profiles are due to the poor statistics (for the obvious reasons of limited access to microgravity conditions) of the experimental averaging and provides a grasp of the large velocity fluctuations taking place in a given realization of the flow, corresponding to the relatively high degree of turbulence. In order to obtain the regular profiles of mean velocity, we average the results over four equivalent realizations with the same characteristics. The resulting profiles of mean velocity and root-mean-square of velocity fluctuations are shown on Figures 4.18 and 4.19, respectively. In both figures it can be appreciated a decrease in time of their magnitudes, which is due to the decay of pseudo-turbulence, a first rough characterization of the temporal evolution associated to the relaxation of the flow dragged by buoyancy forces prior to microgravity.

Due to the unavoidable averaging over the visual direction, and given also the unavoidable limited replicability of an experiment with the large fluctuations inherent to the turbulence, it makes no sense to try to obtain averaged information on a local basis. Therefore we will compare the different cases by averaging out the spatial information into a single parameter for each profile. This averaging will be appropriately weighted using information from the same experiments as follows,

$$\bar{u}_i = \frac{\sum\limits_{k} \langle u_i(y_k) \rangle \; n(y_k)}{\sum\limits_{k} n(y_k)} \;, \tag{4.9}$$

$$\bar{\sigma}_i = \frac{\sum\limits_{k} \sigma_i(y_k) \; n(y_k)}{\sum\limits_{k} n(y_k)} \;, \tag{4.10}$$

where $n(y)$ stands for the mean number of bubbles on each point of the y direction for a given temporal period, and y_k is the position in the y direction of the k-th element of the profile. This averaging will reduce each profile into one characteristic parameter of the flow while granting prevalence of the information from the areas with larger number of bubbles, which are statistically more significant. This reduces the impact of the contributions closer to the sidewalls, while focussing on the central areas of the duct, where the flow is really mixed and fairly uniform and homogeneous. Note that we have used the mean density of bubbles instead of using the total number of velocity measurements since the latter are highly correlated in a single trajectory of a given bubble.

In Figure 4.20 we compare the results obtained over the averaging of multiple equivalent realizations with $Re = 13000$ for two different sizes of bubbles, but maintaining constant the injected gas void fraction. Results show no noticeable difference on the relative velocity dispersion for both sizes of bubbles, suggesting

Figure 4.20: Relative velocity fluctuations for bubbles of size $d_B = 1.6$mm and 2.5mm. Each line has been averaged over the mesures of 4 cameras from two equivalent experiments at $Re = 13000$
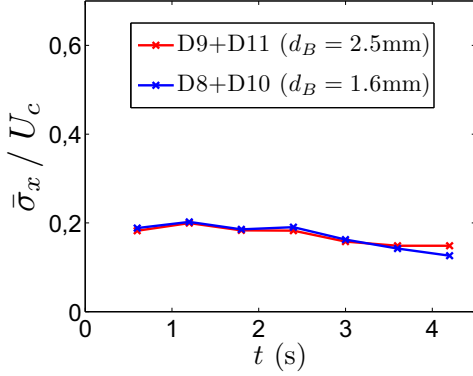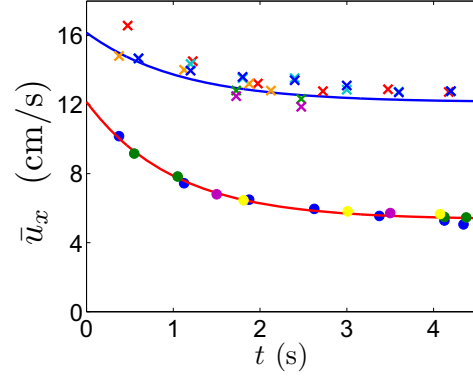
Figure 4.21: Evolution in time of the mean velocity of bubbles $\bar{u}_x$. Each color correspond to a different single experiment (see the legend in Fig 4.22).

that bubble size does not seem to play a significant role in this characterization of turbulence in our range of parameters.

In Figure 4.21 we represent the averaged velocity of bubbles as a function of time for several realizations with various injection parameters, being each color a label for each different experiment. Circles stand for cases with co-flows of $Re = 6000$ while crosses correspond to $Re = 13000$. Experimental values have been fitted to an exponential decay of the form

$$\bar{u}_x = \bar{u}_{x0} + Ae^{-t/\tau} \, , \tag{4.11}$$

where $\bar{u}_{x0}$ is the mean velocity of the stationary flow, A stands for the added mean flow from pseudo-turbulence at $t = 0$ and τ is an effective relaxation time of pseudo-turbulence. Our fitted values read:

$$\begin{cases} \bar{u}_x^{(Re=6000)} = & \left(5.3 + 6.8e^{-t/1.01\text{s}}\right) \frac{\text{cm}}{\text{s}} \\[2mm] \bar{u}_x^{(Re=13000)} = & \left(12.1 + 4.0e^{-t/1.09\text{s}}\right) \frac{\text{cm}}{\text{s}} \end{cases} \tag{4.12}$$

In equation (4.12) we see that, in both cases, the decay of pseudo-turbulence has a relaxation time $\tau \simeq 1$s. that is essentially independent from the Reynolds number of the carrying flow. It is interesting to recall that the response time τ_B of a bubble, as seen on Eq. (4.6), depends on its size but it is $\tau_B < 0.2$ s for all the injection parameters studied in our experiments. That indicates that the remnants of pseudo-turbulence persist for a relatively long time after the relaxation of all bubbles to their local flow velocity.

Figure 4.22: Relative velocity fluctuations for several different experiments. Circles correspond at cases with $Re = 6000$, crosses are for $Re = 13000$. *(Left):* Fluctuations on the direction of the main flow. *(Right):* Fluctuations transversal to the main flow.
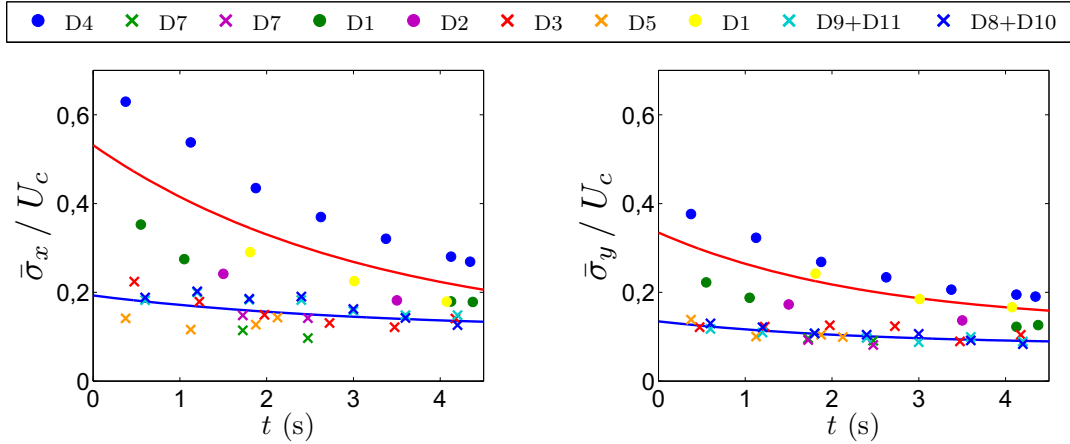
In Figure 4.22 we plot our results on the relative fluctuations of velocity, normalized to the characteristic velocity U_c of the co-flow (i.e., its mean velocity, as measured by a flow-meter placed right after the pump). Each color denotes a specific experiment as in the previous figure. A first remarkable observation is that the experiments with smaller Reynolds numbers have a larger value of the relative velocity fluctuations. Note that this not only contradicts simple scaling arguments but in particular our explicit Lattice-Boltzmann numerical results for the specific geometry and the Reynolds numbers of the experiments, as discussed in Figures 4.12 and 4.13, where we saw that, without bubbles, the magnitude of the relative velocity fluctuations is essentially independent of Re. This result seems to be indicative of an active effect of bubbles. Note also that the increase of relative velocity fluctuations with decreasing Re is consistent with a similar observation for the case of bubble jets, right at the margins of the jets, as discussed in Fig. 3.19, at the end of the previous chapter. It is worth remarking that since we are measuring velocities on bubbles while we have no tracer of the actual liquid flow, it is not possible to assert an actual modification of the statistics of the carrying flow due to the presence of bubbles. Strictly speaking we only observe that bubbles do not seem to be tracing the carrying flow.

A detailed analysis show that for all the experiments with $Re = 6000$ (circles), fluctuations decay with a similar characteristic time and seem to relax to the same asymptotic value, even though the initial value of the velocity dispersion varies largely from experiment to experiment. We have not found any correlation of this initial dispersion with the injection parameters of bubbles. Without the possibility to repeat further the experiments, at this point we can only attribute this effect to an inherent variability of the preparation of the initial condition,

which cannot be fully controlled. For cases with $Re = 13000$ (crosses), unlike for small Reynolds numbers, pseudo-turbulence seems to have a minor effect into the velocity fluctuations. The fitting curves in the figures has been added to guide the eye through the evolution of the cloud of points. To define them, we have first fitted a relaxation time τ (which is the parameter that seems more robust) for each direction of a characteristic experiment, and then we have imposed these values of τ in the fitting of the rest of the data. The resulting curves are:

$$\left\{ \begin{array}{ll} \bar{\sigma}_x^{(Re=6000)} = & \left(0.10 + 0.43 e^{-t/3.2\text{s}}\right) U_c \\[2mm] \bar{\sigma}_x^{(Re=13000)} = & \left(0.11 + 0.08 e^{-t/3.2\text{s}}\right) U_c \end{array} \right. \tag{4.13}$$

$$\left\{ \begin{array}{ll} \bar{\sigma}_y^{(Re=6000)} = & \left(0.13 + 0.21 e^{-t/2.4\text{s}}\right) U_c \\[2mm] \bar{\sigma}_y^{(Re=13000)} = & \left(0.08 + 0.05 e^{-t/2.4\text{s}}\right) U_c \end{array} \right. \tag{4.14}$$

From these fittings it is interesting to observe the resulting relaxation times of $\tau = 3.2$ s and 2.4s, respectively. These are significantly larger than the values found for the relaxation of the mean velocity ($\tau = 1.0$ s) in Eq.(4.12). This suggests that velocity fluctuations of the pseudo-turbulence effectively decay to the co-flow values in a slower time scale than the mean velocity.

Finally, even though the asymptotic value of the relative fluctuations is subject to relatively larger uncertainty than the time scales, it seems that the fluctuations of the transversal y-components show a significant dependence of the relative fluctuations on the Reynolds number, along the lines of the overall tendency to decrease for increasing Re. For the longitudinal components, however, the fitted asymptotic value does not exhibit any conclusive tendency in this respect.

4.4.3 Statistics of bubble pairs

As a last insight on the dynamics of bubble suspensions in a turbulent flow, we will study the behavior of pairs of bubbles and compare them to numerical predictions obtained in simulations. To this aim, we have introduced a large amount of point-like passive tracers on our Lattice-Boltzmann simulations as described in chapter 2.2.9. We have placed them in a regular initial configuration at relative distances of 1.25 mm and we have studied the statistical evolution of the averaged distance between pairs of tracers, as a function of time.

In Figure 4.23 we show a transversal coordinate as a function of time, and the projection on the transversal section of four trajectories described by tracers located initially on a close neighborhood. It can be observed that the tracers
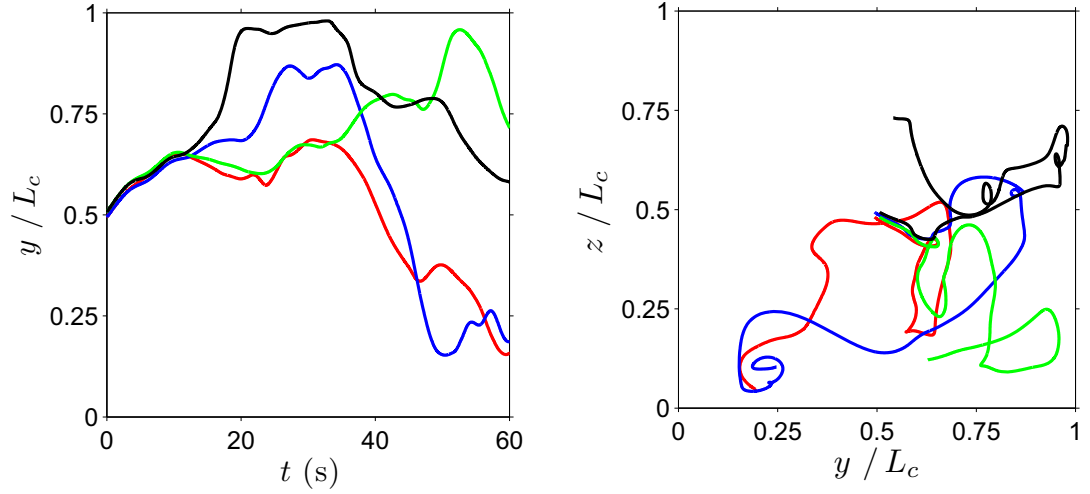
Figure 4.23: Transversal trajectories described by 4 passive tracers initially separated a distance of 1.25mm of each other in a flow with $Re = 3800$

remain close to each other for a certain finite time and then they strongly diverge from each other.

Experimental measurements have been taken from the trajectories of bubbles previously captured with particle tracking methods. Those located at a distance smaller than 2 mm of another bubble (measured from their centers), have been considered a pair and have been used to calculate the averaged temporal evolution of their separation. In Figure 4.24 we display the evolution of the mean distance between pairs of bubbles at different temporal ranges of the microgravity experiments. It is important to recall that pseudo-turbulence is decaying during the experiment, affecting the measured magnitudes. Noisy signals at the final part of the lines denote a lack of sufficient statistics, caused by the high degree of screening between bubbles in the videos, which makes impossible to follow the trajectory of a bubble for a long period of time. Thus, as time increases, we are losing the track of more bubble pairs and by consequently we get poorer statistics.

In Figure 4.25 we plot the mean separation of bubble pairs, measured after the first second of microgravity. Each line corresponds to a different set of injection parameters. Dark blue line has been averaged over the measures of four video cameras from two equivalent experiments. We find that the measurements for equivalent degrees of turbulence share a similar slope once they have reached the linear regime, defining an effective rate of separation.

In Figure 4.25, dashed lines correspond to the linear fittings:
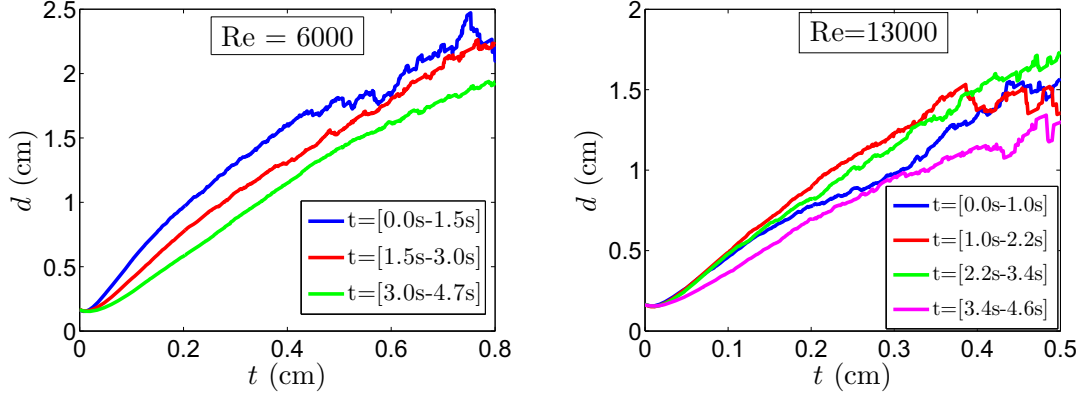
Figure 4.24: Mean separation of pairs of bubbles. Each line correspond to a temporal range of the experiment in microgravity. *(Left):* Single experiment (D4) with $Re = 6000$. *(Right):* Single experiment (D8) with $Re = 13000$.
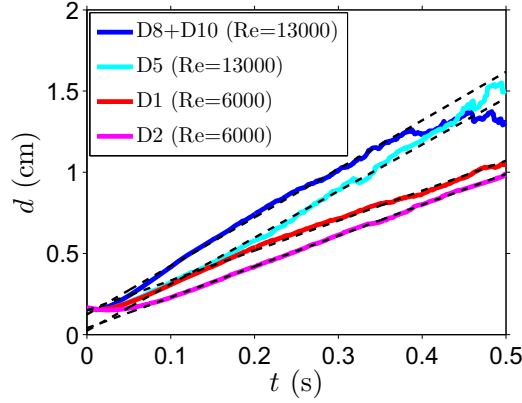
Figure 4.25: Mean separation of pairs of bubbles for different parameters of injection. Results have been taken after the first second of microgravity. Dashed lines are fittings of the correspondent data

$$
\begin{cases}
d^{(Re=6000)} = & \left(1.90\frac{\text{cm}}{\text{s}}\right)t + 0.04\text{cm} \\[2mm]
d^{(Re=6000)} = & \left(1.84\frac{\text{cm}}{\text{s}}\right)t + 0.15\text{cm} \\[2mm]
d^{(Re=13000)} = & \left(2.85\frac{\text{cm}}{\text{s}}\right)t + 0.02\text{cm} \\[2mm]
d^{(Re=13000)} = & \left(2.99\frac{\text{cm}}{\text{s}}\right)t + 0.12\text{cm}
\end{cases}
\tag{4.15}
$$

A clear dependence with Reynolds number can be observed on the rate of separation obtained in the fittings. For an increase of Re by a factor $\simeq 2.2$, the separation rate is increased by a factor $\simeq 1.6$.

At this point it is important to call the attention upon the fact that the pairs of bubbles defined from experimental images are in most cases just apparent, due
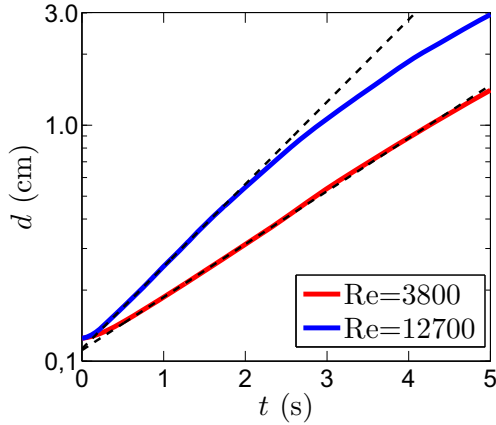
Figure 4.26: Mean separation between real pairs of tracers. Distances on logarithmic scale. Fittings in dashed lines.
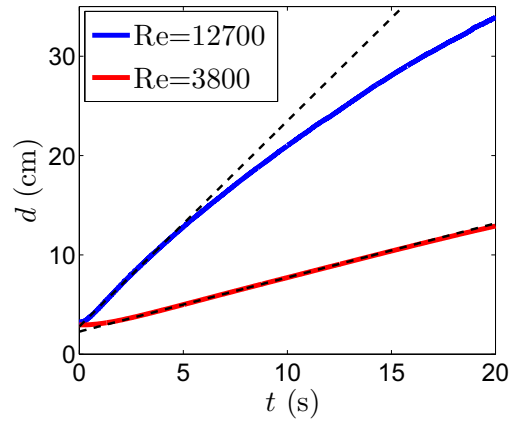
Figure 4.27: Mean separation between apparent pairs of tracers (i.e., initial $\Delta y_0 > 1.6$mm). Fittings in dashed lines.

to the lack of information about the depth along the visual direction z. A large majority of them will be separated distances much larger than the bubble size and thus following rather independent trajectories. If we consider that a pair of bubbles is real when their initial separation Δz_0 in the visual direction is lower than 1.5 mm, for a homogeneous distribution of bubbles in our duct of width $L_y = 100$mm we obtain a proportion of about 3% of real pairs, against 97% of apparent ones. One could think of different strategies to differentiate the two populations of pairs, with the help of a detailed statistical study of tracers in the simulations. However, due to the small statistical significance of the real pairs, the lack of more experiments to increase the amount of data makes any of such attempts virtually hopeless.

In Figure 4.26 we show the evolution of the mean separation between real pairs of tracers, obtained from our simulations for two different degrees of turbulence. The first noticeable observation is that real pairs of tracers, unlike our experimental measures, have an average separation that grows closer to exponentially in time. This rate is defined by an exponent $\mathscr{L}$, which we may assimilate to an effective Lyapunov exponent, that controls the average rate of exponential separation $\delta(t) = \delta(0)e^{\mathscr{L}t}$ of infinitesimally close trajectories in a chaotic dynamical system [Salazar and Collins (2009)]. Fits in Figure 4.26 correspond to:

$$
\begin{cases}
d^{(Re=3800)} = & (0.11\text{cm}) \, e^{\left(0.52 \text{ s}^{-1}\right)t} \\
d^{(Re=12700)} = & (0.11\text{cm}) \, e^{\left(0.80 \text{ s}^{-1}\right)t}
\end{cases}
\tag{4.16}
$$

which adjust nicely to simulations until the finite size effects of the duct section become important and slow down the growth, as can be observed in the figure,
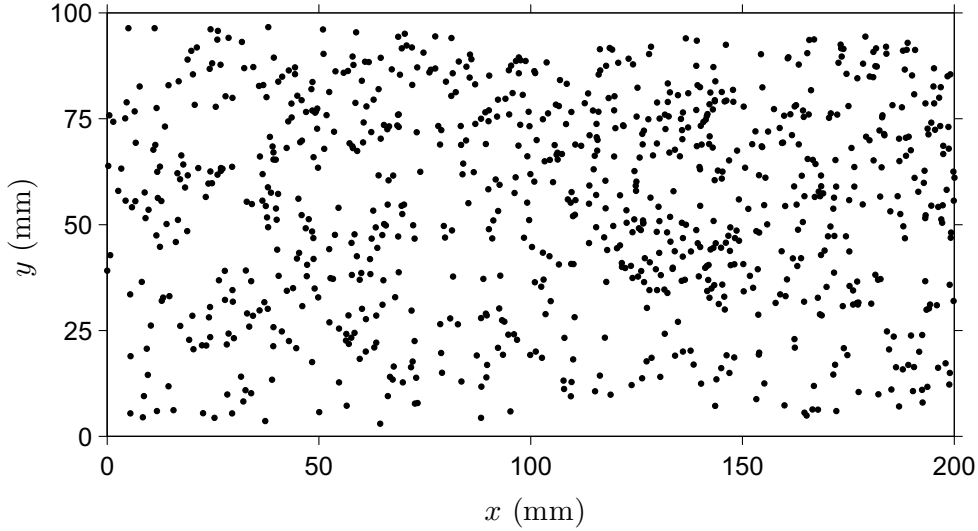
Figure 4.28: Distribtion of punctual tracers for a slice of the duct of $\Delta z = 5$mm at the midplane between walls. Simulation with $Re = 12700$.

for long times in the most turbulent case.

In order to compare the experimental measurements with those of simulations taken in equivalent conditions, we have evolved the initially structured configuration of tracers for a long period of time, reaching a homogeneous distribution. Figure 4.28 show a slice of $\Delta z = 5$mm of the duct, to get a sense of the high density of tracers and their homogeneous distribution in space. We have measured the average separation of apparent pairs of tracers by selecting as a pair only those initially separated a distance smaller than 2 mm in the $x - y$ plane, but larger than 1.5 mm in the z direction. Figure 4.27 shows the resulting curves, describing a linear growth of the separation, like in the experimental measurements of Figure 4.25, until the finite size effects of the duct enter into play. The fits of Figure 4.27 are given by

$$
\begin{cases}
d^{(Re=3800)} = & \left(0.54\frac{\text{cm}}{\text{s}}\right) t + 2.27\text{cm} \\[2ex]
d^{(Re=12700)} = & \left(2.07\frac{\text{cm}}{\text{s}}\right) t + 2.79\text{cm}
\end{cases}
\tag{4.17}
$$

which show a dependence of the rate of separation between tracers with Re similar to the experimental case of equation (4.15). In this case, an increase by a factor $\simeq 3.3$ of the Reynolds number causes a factor $\simeq 3.8$ in the growth of the separation rate.

The last aspect we will analyze concerning the dynamics of bubble pairs is the measurement of the statistics of times before separation beyond a minimum
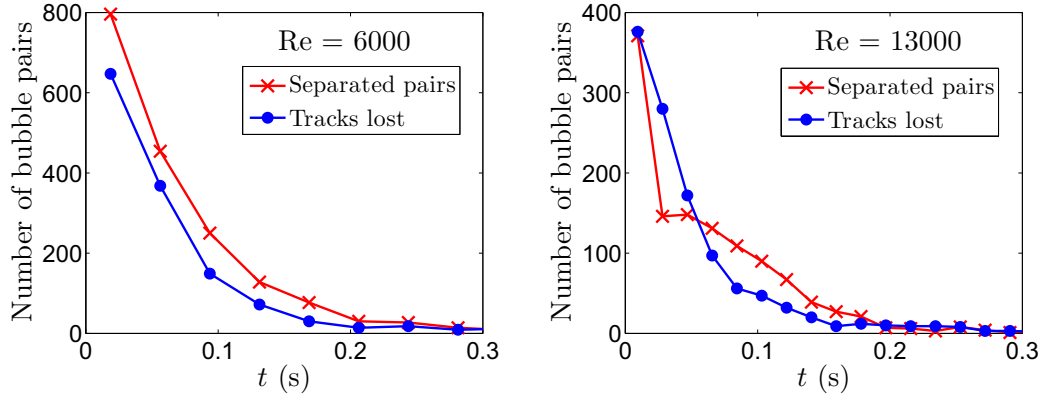
Figure 4.29: Crosses represent the duration of experimental (apparent) pairs of bubbles. Circles indicate the number of pairs to which we have lost track, after a given time, due to screening effects. *(Left)* Experiment D4, $Re = 6000$. *(Right)* Experiment D3, with $Re = 13000$.
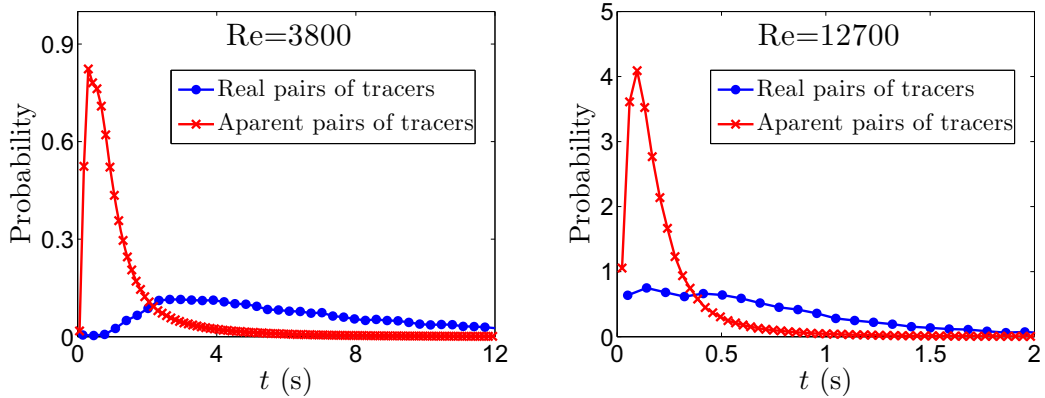
Figure 4.30: Normalized probability distribution of duration of pairs of tracers. *(Left)* $Re = 3800$. *(Right)* $Re = 12700$.

distance. In the experimental measurements, as well as in the simulations, we have considered the time lapse between the moment the pair reduces its separation to a distance smaller than 2 mm and the moment it surpasses 4 mm, always taken between their respective centers. In Figures 4.29 and 4.30 we show the experimental data and the simulated predictions, respectively.

Results are hard to compare due to the large amount of screening events in the experimental images, that produce an increasing uncertainty in the shape of the curves as the time lapse grows. In simulations, significant differences are observed between the distribution of probability for real pairs of tracers and that of apparent pairs, with much longer life times for real pairs, as a result of the strong correlations of velocities in nearby bubbles, as opposed to the case essentially un-

correlated for distant ones. From the detailed knowledge of the statistics of the time separation of both apparent and real pairs, taken from numerical simulations together with the appropriate characterization of the screening effects, the proper fitting functions could be obtained that would allow to correctly project the experimental data into a reduced set of parameters in order to extract the statistics of real versus apparent bubble pairs, and thus try to detect whether this observable captures some effect not contained in the passive tracer picture. We have not pursued this idea because, as pointed out before, the limited number of experiments available prevents from reaching statistically significant conclusions for the minority of the events of interest, namely those corresponding to the real pairs.

4.5   Conclusions

A new experimental setup for the study of monodisperse bubble suspensions in microgravity has been design and assembled. It has been prepared to resist the highly demanding mechanical requirements of experimentation in a drop tower, for which the setup needs to resist peaks of deceleration around forty times larger than normal gravity. With that new experimental setup we have conducted a series of 36 drops of 4.7 s in drop tower of ZARM in Bremen.

It is worth remarking that, with the innovative procedure here developed, its has been achieved for the first time in microgravity, a relatively homogeneous suspension of monodisperse, highly spherical bubbles in a turbulent flow. Achieving this type of configuration with the possibility to control separately the bubble size, the bubble density and the degree of turbulence, opens the possibility to obtain valuable data for both fundamental and applied studies, in relatively simple situations, amenable to theoretical analysis and interpretation. The key innovation in our setup is the combination of several independent T-junctions, which inject uniform and equally spaced bubbles into a square duct, within a turbulent flow. In this configuration, the minimum degree of turbulence used ($Re = 6000$) has proved to be enough to disperse bubbles through the duct.

Bubble density has been chosen so that bubble separation is of the order of the most energetic eddies in the flow, and smaller in diameter, so that the turbulence is most effectively exploited as a dispersion mechanism to distribute bubbles as homogeneously as possible in the duct, while minimizing the possibility of bubble coalescence. At the same time bubbles are larger than the dissipative scales of the turbulence, so that in principle they can have a nontrivial interaction with the turbulence, instead of a mere passive tracer role. Under the experimental conditions, the Weber number (which measures the ratio of inertial to capillary forces)

is small enough to keep the bubbles essentially spherical, resulting in important simplifications for theoretical and simulational modeling.

After a proper statistical analysis of the velocity of bubbles (captured from particle tracking techniques upon the processed videos of the experiments) it has been possible to analyze quantitatively for the first time the decay of the pseudo-turbulence. We have found that, while the viscous response time of a bubble is $\tau_B < 0.2$ s for our bubble sizes, implying a quick deceleration of the bubbles after the gravity swicth-off, the mean velocity of the residual flow initially dragged by the buoyant bubbles relaxes with a larger time of $\tau = 1.0$ s. In addition to this, for the case of a co-flow with $Re = 6000$, the excess of velocity fluctuations in the flow due to the pseudo-turbulence decays with a relaxation time of $\tau_x = 3.2$ s in the direction of the main flow and $\tau_y = 2.4$ in the direction transversal to it. For the cases with $Re = 13000$, instead, it has not been found any significant impact of the pseudo-turbulence upon the degree of velocity fluctuations of the flow. This seems to be due to the fact that the higher degree of intrinsic turbulence of the co-flow masks the effects of pseudo-turbulence.

Large scale Lattice-Boltzmann simulations have been performed to produce reference states of turbulence with the exact conditions of the experiments but without bubbles, to allow direct comparison with experimental data, and in particular to elucidate possible active roles of bubbles in modifying the carrier flow, or deviating from the mere passive tracer behavior. One of the conclusions of the numerical study is that the relative velocity fluctuations (scaled to its characteristic velocity) of a turbulent liquid flow is essentially independent of the degree of turbulence, in accordance with scaling arguments of fully developed turbulence, which do not have to be necessarily applicable in a finite duct at our values of Reynolds number. In the experiments, however, we observe that the relative velocity fluctuations displayed by bubbles deviate from this prediction, and reflect a tendency do decrease with increasing Reynolds number. This is consistent with similar observation in the previous chapter for turbulent bubble jets, and seems to be a genuine active effect of bubbles.

The Lattice-Boltzmann simulations have also been used to study the statistics of point-like tracers of the flow. In particular we have studied the first-passage time statistics associated to the separation of two-close tracers. We find that the average distance between a pair of tracers increase exponentially with an effective time scale that depends on the degree of turbulence in the flow. For the case of a pair of apparent tracers, though, where both tracers are closer in the plane of the pictures but far in the other direction (unmeasurable in our experiments) the average separation between them increases linearly with time. In the analysis of experimental data, we find a similar behavior for the apparent pairs, which dominate the statistics. Real pairs are comparatively rare, and any statistical

method to extract the corresponding information for those cases suffers from the overall lack of sufficient statistics of the experiments, which cannot be repeated as many times as desired for obvious reasons.

Chapter 5

Effects of g-jitter in Bridgman solidification

5.1 Introduction

The impact of different mechanical disturbances on crystal quality is a longstanding and crucial issue in crystal growth under microgravity conditions [Duffar et al. (2001); Benz and Dold (2002); Friedrich et al. (2003); Polezhaev and Nikitin (2009); Duffar (2010)]. Typical disturbances in microgravity environments involve different accelerations in the form of quasi-steady residual values, short pulses, pulse trains of finite duration and high frequency background signals or g-jitters [Duffar and Garandet (2000); Nikitin et al. (2001); Bessonov and Polezhaev (2001); Levtov et al. (2009); Zavalishin et al. (2009, 2010); Casademunt and Viñals (2001)]. Since the frequency structure of realistic accelerometric signals is often very complex due to the large number of uncontrolled sources that may be present in a given microgravity environment, a possible strategy that has been proposed is to model g-jitters as stochastic processes, in particular because it is difficult to assess a priori the extent to which the linear superposition principle of the effects of the forcing at different frequencies can be invoked in general, due to nonlinearities of the equations.

Stochastic characterization of real g-jitters was first discussed by Thomson et al. (1997), and stochastic modeling of g-jitters was applied to different physical processes relevant to both fundamental physics and space technology, such as in coarsening of colloidal suspensions [Thomson et al. (1997)], fluid-fluid interfaces [Zhang et al. (1993); Casademunt et al. (1993)] and in thermal natural convection [Thomson et al. (1995)]. In the present chapter[1] we pursue this approach in a

---

[1]This work has been accepted for publication on J. of Crystal Growth [Ruiz et al. (2012)].

realistic modelization of different prototypic setups of crystal growth in microgravity in the context of semiconductor materials. As impact indicators we use here the time evolution of the longitudinal and transversal segregation parameters. Following Refs. [Zhang et al. (1993); Casademunt et al. (1993); Thomson et al. (1995)], we will model a generic stochastic acceleration environment by means of the so-called narrow-band noise, a rather general Gaussian stochastic process that is characterized by three parameters: the noise intensity, a characteristic dominant frequency where it may be peaked, and a correlation time that controls band width of the frequency spectrum. This stochastic process interpolates between the two extreme cases of white noise and single-frequency noise.

The convective response of the velocity field in a cavity with a stochastic g-jitter transversal to a thermal gradient in a generic fluid configuration was studied in detail by Thomson et al. (1995). Here we will extend that approach to include typical confined crystal growth configurations and the coupling of the dopant concentration field to the flow field. We will also focus on parameter values and configurations that are as close as possible to realistic conditions of actual solidification setups in space. Therefore we aim at a quantitative characterization of segregation phenomena as a function of the statistics of the g-jitter. Furthermore, we will propose a simplified heuristic model that captures the behavior of the system with a remarkable accuracy with only a few parameters to be obtained from the full integration once and for all. The model provides a qualitative and quantitative understanding of the response of the dopant field to the acceleration driving forces, and becomes a predictive tool to check the effects of any arbitrary acceleration signal with a considerably reduced numerical effort. As a general conclusion, we will find that the system response is strongly dominated by the low-frequency components of the forcing.

5.2   Definition of the model and numerical integration

5.2.1   The problem. Setup and physical context

We study the directional solidification of a semiconductor melt inside an ampoule with a dopant as a diluted solute and in the presence of a weak fluctuating gravity. See Fig. 5.1 for a sketch of the geometrical configuration used.

The density gradients that drive natural convection receive in general contributions from both temperature and solute concentration fields. However, in the case of the present semiconductors, the dopant concentration is sufficiently small
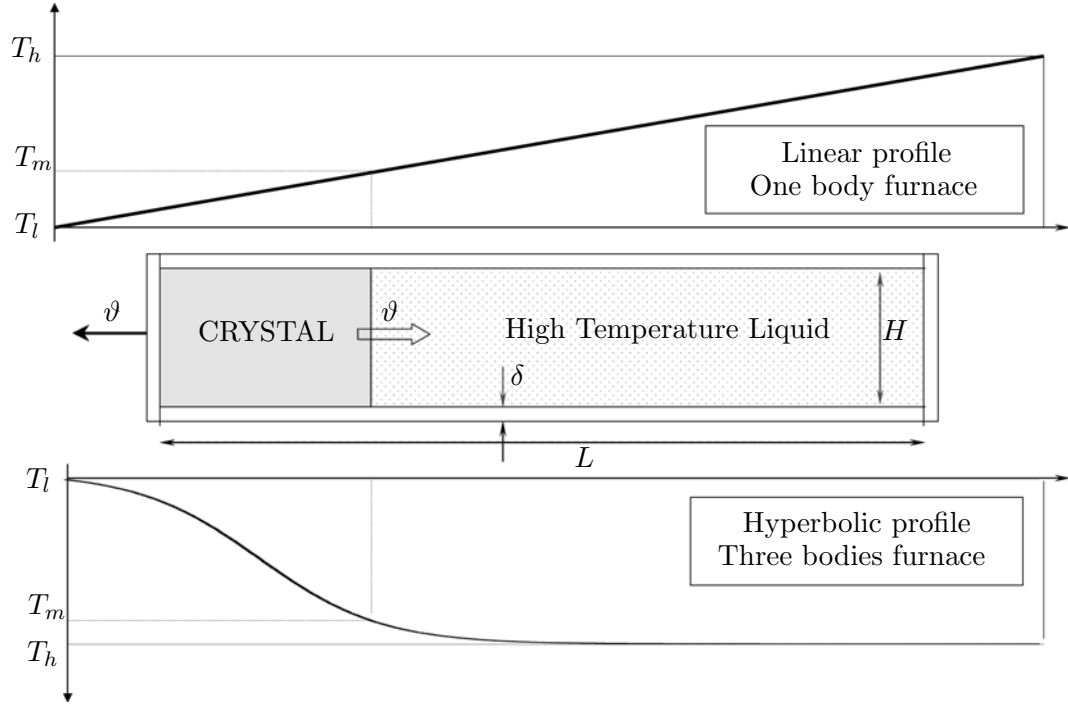
Figure 5.1: Global setup of the problem. Top and bottom: sketches of the two thermal profiles employed in the work (see text).

to neglect its contribution to buoyancy when compared to that due to thermal expansion. In addition, the typically small Prandtl numbers of both semiconductors imply that thermal field is only weakly affected by the induced convection and in general it reaches its essentially steady configuration in a very short transient. On the other hand, the solute diffusion is slower. Solute is expelled by the advancement of the solidification front, which forms a layer ahead the interface. This solute layer, in the absence of gravity, has a width of the order of the diffusion length D/v_p and, as shown by Tiller et al. (1953), is built on a time scale of the order of D/kv_p^2, being D the solute diffusivity, k the segregation coefficient and v_p the velocity of the solidification front imposed externally (see also [Smith et al. (1955); Caroli et al. (1993); Garandet et al. (2000)]).

Due to the incompressibility of the liquid phase, any residual acceleration can be assimilated to an effective (time-dependent) gravity, which will in general induce some degree of convection due to thermal buoyancy. Accordingly, there will be a significant solutal transport due to advection that will in general result in an inhomogeneous concentration profile in the final crystal. Our objective in this study is to correlate the type of time dependent residual gravity to the dopant segregation resulting from the thermally-induced solutal convection.

Within a perturbative approach of the effect of the residual gravity, it makes

sense to consider only an effective gravity vector that is oriented transversally to the advance of the solidification front. This is due to the fact that only the components of the density gradient that are perpendicular to the effective gravity do generate vorticity in the flow, and to lowest order the density gradient is oriented longitudinally. Transversal components of the density gradient will only be generated by convection due to the residual gravity and therefore their coupling to possible longitudinal components of gravity would correspond to higher order corrections. The geometric arrangement is thus that of natural (lateral) convection. Note that components of gravity parallel to the main density gradient can in principle generate convection through a Rayleigh-Bénard instability, but this would only occur for much larger values of gravity. We will also assume that the effective gravity has zero mean. If the mean value is significantly different from zero, the nature of the problem is fundamentally different as it will be dominated by this constant component.

In our simulations we switch on the time dependence of the residual gravity at a time when the solidification length is roughly 25% of the total length, so that the density profile has already developed when g-jitter starts. This is done for simplicity in order to avoid nontrivial and nongeneric effects associated to the early stages of rapid variation of the concentration profile, but the analysis could as well be generalized to g-jitters starting at $t = 0$. Also, to avoid end wall effects, we stop the simulation at a time when the solidification length is less than 70% of the total length of the ampoule.

5.2.2   Model equations and parameters

The numerical simulation of the growth process involves the resolution of the time dependent transport equations in the melt ahead of the solidification front with the appropriate boundary conditions at the moving interface, which we will consider as flat. Local equilibrium then implies that the interface is at the melting temperature, moving at a constant velocity v_p. Because of the continuous decrease of the melt volume in the ampoules of the characteristic setups of crystal growth in space facilities [Ruiz (2007)], the computation domain corresponding to the melt is a rectangle of height H and a time dependent length $L(t) = L(0) - v_p t$.

The transport equations for the velocity, temperature, and dopant concentration of the melt are written for an incompressible fluid in the Boussinesq-Oberbeck approximation as follows,

$$\nabla \cdot \mathbf{v} = 0, \tag{5.1}$$

$$\frac{\partial \mathbf{v}}{\partial t} + (\mathbf{v} \cdot \nabla)\,\mathbf{v} = -\frac{1}{\rho}\nabla P + \nu\nabla^2(\mathbf{v}) + \tilde{B}(t)\hat{y}, \tag{5.2}$$

$$\frac{\partial T}{\partial t} + \nabla \cdot (T\mathbf{v}) = \alpha \nabla^2 T, \tag{5.3}$$

$$\frac{\partial c}{\partial t} + \nabla \cdot (c\mathbf{v}) = D \nabla^2 c. \tag{5.4}$$

The buoyancy term $\tilde{B}(t)$ in the Navier-Stokes equation is given by

$$\tilde{B}(t) = \beta^T T \tilde{g}(t), \tag{5.5}$$

where β^T is the thermal expansion coefficient, T the temperature and $\tilde{g}(t)$ the time dependent gravity (in the transversal y-direction), which, in general, is an arbitrary function of time. Note that we neglect contributions to buoyancy originated at concentrations gradients.

In the stochastic case this fluctuating gravity has been modeled as a narrow-band noise, a stochastic process defined as Gaussian, with zero mean, and a spectrum given by Thomson et al. (1995)

$$P(\omega) = \frac{\tilde{G}^2 \tilde{\tau}}{2\pi} \left(\frac{1}{1 + \tilde{\tau}^2(\Omega + \omega)^2} + \frac{1}{1 + \tilde{\tau}^2(\Omega - \omega)^2} \right). \tag{5.6}$$

which is peaked at $\pm\Omega$ with a peak width of $\tilde{\tau}^{-1}$. Accordingly, the autocorrelation function reads

$$\langle \tilde{g}(t)\tilde{g}(t') \rangle = \tilde{G}^2 e^{-\frac{|t-t'|}{\tilde{\tau}}} \cos \Omega(t - t'), \tag{5.7}$$

where $\tilde{G}^2 = \langle \tilde{g}^2 \rangle$ is the second moment of the noise and $\tilde{\tau}$ is its correlation time. The limit $\tilde{\tau} \to \infty$ with $\tilde{G}^2$ finite corresponds to a monochromatic noise with frequency Ω. Close to this limit, $\tilde{G}^2$ is the appropriate measure of the noise intensity. In the opposite limit, $\tilde{\tau} \to 0$ with $D_g = \tilde{G}^2 \tilde{\tau}$ finite, this process reduces to a Gaussian white noise. Close to this limit the appropriate definition of noise intensity is D_g. Finally, for $\Omega = 0$ the narrow-band noise reduces to the so-called Ornstein-Uhlenbeck process [Gardiner (2009)].

The narrow-band noise can be easily generated in practice by using the following expression:

$$\tilde{g}(t) = \tilde{S}_1(t)\cos\Omega t + \tilde{S}_2(t)\sin\Omega t, \tag{5.8}$$

where $\tilde{S}_1, \tilde{S}_2$ are two independent Ornstein-Uhlenbeck processes defined by

$$< \tilde{S}_i(t) > = 0, \tag{5.9}$$

$$< \tilde{S}_i(t)\tilde{S}_j(t') > = \tilde{G}^2 \delta_{ij} e^{-\frac{|t-t'|}{\tilde{\tau}}}, \tag{5.10}$$

for $i, j = 1, 2$.

Finally, for the ampoule walls, the diffusion equation reads

$$\frac{\partial T}{\partial t} = \alpha_{sol} \nabla^2 T. \tag{5.11}$$

Table 5.1 shows the parameter values involved in all these equations for the two materials considered Ge : Ga and GaAs : Se, two common choices flown in many space missions, for instance in the early Apollo-Soyuz mission (Ge : Ga; 1971) or during NASA Space Shuttle missions (GaAs : Se; USMP1,1991 and EURECA, 1992). For characteristic values of $\tilde{g}(t)$ we have taken those fitted by Thomson et al. (1997) from real g-jitter data collected by a SAMS detector during a SL-J mission.

We define dimensionless variables by using H as length scale, H^2/ν as time scale, and the initial temperature difference along the cavity $\Delta T = T_h(0) - T_m$ as the characteristic temperature scale, where T_m is the melting temperature and $T_h(0)$ the initial highest temperature of the domain at the opposite side of this moving interface. We thus define the dimensionless temperature deviation as

$$\theta = \frac{T - T_m}{\Delta T}. \tag{5.12}$$

As discussed by Thomson et al. (1995), for a stochastic case with significant high-frequency components it is appropriate to scale the gravity by an acceleration scale of the form $\sqrt{\tilde{G}^2 \tilde{\tau} \nu}/H$ so that

$$g = \frac{H}{\sqrt{\tilde{G}^2 \tilde{\tau} \nu}} \tilde{g}. \tag{5.13}$$

Similarly, it is appropriate to define a stochastic Rayleigh number of the form

$$\mathrm{Ra}^* = \frac{\beta^T \Delta T H^2 \sqrt{\tilde{G}^2 \tilde{\tau}}}{\nu \sqrt{\alpha}}. \tag{5.14}$$

The dimensionless form of the parameters defined with a tilde will thereafter be written without tilde. Therefore, we have

$$G^2 = <g^2> = \frac{\mathrm{Pr}}{\tau} \tag{5.15}$$

and

$$B(t) = \frac{\mathrm{Ra}^*}{\mathrm{Pr}}(S_1(t) \cos \Omega t + S_2(t) \sin \Omega t)\theta = B_{st}(t)\theta, \tag{5.16}$$

with $B_{st}(t)$ the dimensionless stochastic buoyancy factor. Functions $S_i(t)$ have been scaled with the same factor that gravity, and times and lengths are now dimensionless. As an illustrative example, Fig. 5.2 shows a typical power spec-

trum of $B_{st}(t)$, generated with typical parameters extracted from g-jitter data corresponding to real microgravity environments, as mentioned above.

With regard to thermal boundary conditions, two generic profiles have been considered (see Fig. 5.1). The first one is a moving hyperbolic profile of temperature directly applied to the external part of the ampoule wall. The second one is a moving linear thermal profile also applied to the external part of the ampoule wall. Since experiments are usually carried out under vacuum conditions, it is reasonable to neglect any external convective transport and simply apply the thermal profile on the ampoule walls considered isotropic, non-reactive and with low thermal conductivity (the values used in all cases are very close to those of quartz). The thermal contact between the inner solid walls and the liquid phase have been considered perfect excluding the formation of free surfaces inside the ampoule, and heat flux continuity has been imposed in the internal side of all walls.

The solidification front moves at constant velocity v_p, and the solute concentration at both sides of the interface are related by the segregation coefficient k as $c_S = kc$. Then, the solute conservation at the interface reads

$$\frac{\partial c}{\partial x} = -\text{Sc } v_p \ (1 - k)c \tag{5.17}$$

where Sc$= \nu/D$ is the Schmidt number. Eq.(5.17) is thus the boundary condition imposed on the concentration field at the interface. For the other boundaries, zero solute flux is imposed. Finally, no-slip boundary conditions for the velocity field are applied to all the boundaries of the domain including the solid-liquid interface.

The quality of the grown crystals is usually defined in the literature in terms of the dopant segregation and typically make use of two quantitative indicators, the longitudinal and the transversal segregation parameters [Garandet et al. (1994)]. The dimensionless longitudinal segregation parameter defined as a transversal average

$$\zeta(x) = \int_0^1 c^{sol}(x, y) dy \tag{5.18}$$

is most adequate to characterize the overall transients of the build-up of the concentration profile thus characterizing the history of the process, given that the x-coordinate is directly mapped to time. Here we will mostly focus on the transversal segregation parameter defined as

$$\xi(x) = \frac{c_{max}^{sol}(x) - c_{min}^{sol}(x)}{c_{avg}^{sol}(x)}, \tag{5.19}$$

where c_{max}^{sol}, c_{min}^{sol}, and c_{avg}^{sol} are the maximum, minimum, and average concentration
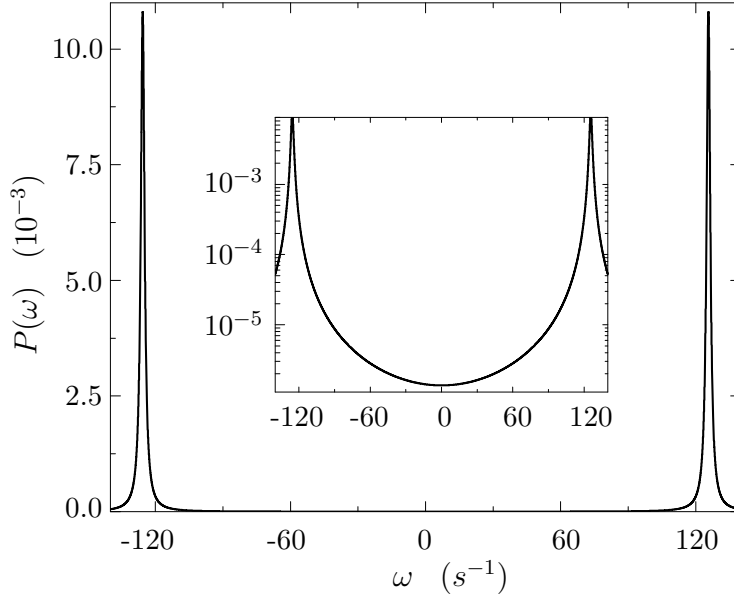
Figure 5.2: Two-sided power spectrum of a typical dimensionless stochastic buoyancy factor signal. The inset show a central detail in logarithmic scale.

values along the transversal direction in the solid interface. This indicator is most sensitive to the convection induced by the residual gravity and reflects all the complexity of the time-dependence of the g-jitter.

5.2.3   Numerical methods

The transport equations have been integrated using finite volume methods. To do this, all the equations are rescaled in the x direction (to a unity computational length) and then discretized in a non-uniform mesh. We have used the SIMPLE algorithm (Semi-Implicit Method for Pressure-Linked Equations), discretizing both convective and diffusive terms by a centered scheme and using averaged values for transport coefficients. Pressure has been solved by means of the Fast Fourier Transform method (FFT). As starting condition we use fluid at rest ($\mathbf{v} = 0$), the melting temperature ($\theta = 0$) for all the domain and a homogeneous value of the concentration ($c = 1$). More computational details may be found in [Ruiz (2007)] and also in Table 5.1. The simulation of the stochastic signal for the time-dependent gravity $g(t)$ is based on an adapted integral algorithm [Fox et al. (1988)] for which we have used a pseudorandom number generator first introduced by Marsaglia et al. (1990) and later improved by James (1990).
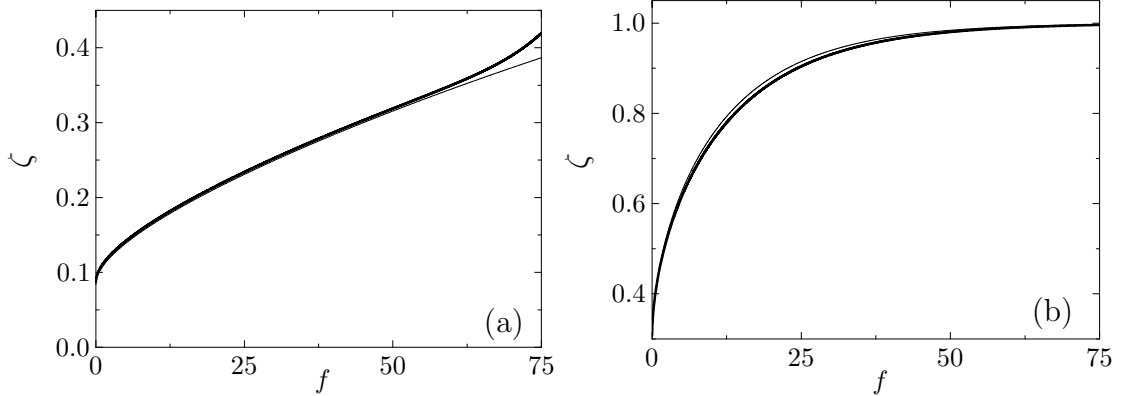
Figure 5.3: Comparison between the longitudial segregation numerically obtained in the pure solutal diffusion case (thick line) and the corresponding analytical solution for the semi-infinite diffusion problem (thin line), as a function of the percentual solidified fraction; (a) Ge : Ga and (b) GaAs : Se.

5.3 Results from direct numerical integration

5.3.1 The build-up of the concentration profile

As a first check and reference case we numerically solve the purely diffusive case of solidification in the absence of convection, at zero-g, and compare the results obtained with analytical predictions. In this case the results directly show the transient process of redistribution of solute while the layer ahead the interface is formed [Tiller et al. (1953)]. Fig. 5.3 shows our numerical solution for the pure solutal diffusion case in terms of the longitudinal segregation as a function of the solidified fraction f, defined as the percentual fraction of the length of the whole rectangular cavity that has solidified. Since the pulling velocity is constant, $f = 100 \frac{v_p t}{L(0)}$ is directly a measure of time. The Smith solution [Smith et al. (1955); Garandet et al. (2000); Verhoeven et al. (1988)] of the 1D semi-infinite diffusion problem is plotted for comparison. Explicitly, this solution reads

$$\frac{c_s}{c_0} = \frac{1}{2} + \frac{1}{2}\mathrm{erf}\left(A_1\sqrt{f}\right) + \frac{A_2}{2}e^{-A_3 f} - \frac{A_2}{2}e^{-A_3 f}\mathrm{erf}\left(A_1 A_2 \sqrt{f}\right), \qquad (5.20)$$

where A_1, A_2 and A_3 are constants that depend on the segregation coefficient. The agreement between both curves is excellent. A slight departure at late stages can be attributed to finite size effects, not included in the analytical approximation. Notice also that for the GaAs:Se case the steady state of the concentration field is attained but in the Ge:Ga case, the initial transient is not complete even at the end of calculations due to the small value of the segregation coefficient (see Table 5.1).

Figure 5.4: (a) Two stochastic transversal segregation realizations corresponding to linear (thick line) and hyperbolic (thin line) thermal boundary conditions in the Ge : Ga case; (b) Detail on the relation existing between the stochastic transversal segregation output (top) and the noise input -equivalently, the stochastic buoyancy factor- (bottom) for a small temporal window labeled as 1 in (a). The correlation time, $\tilde{\tau}$, and the frequency, Ω, used here for the generation of the stochastic buoyancy factor are 1 s and $40\pi s^{-1}$ respectively.

5.3.2   Stochastic g-jitters

The numerical integration of the stochastic case for the two materials and the two thermal boundary conditions considered here produces the stochastic transversal segregation realizations such as those shown in Figs. 5.4 and 5.5. In both examples we have used low values of $\tilde{G} = \sqrt{\langle \tilde{g}^2 \rangle} = 2 \times 10^{-4}$ cm/s^2. The response of the system as measured by the stochastic transversal segregation parameter can typically be seen as the superposition of an erratic, slow, large-amplitude wandering and a small amplitude rippling on the scale of the characteristic frequency Ω of the noise (see the detailed comparison of the stochastic buoyancy and the segregation parameter in Figs. 5.4b and 5.5b). Results show that the Ge : Ga growth system seems to be more sensitive than the GaAs : Se one to this type of perturbations and that, in all cases, the hyperbolic thermal boundary condition produces a large-scale response significantly bigger than the one obtained under linear thermal boundary conditions. The latter is clearly associated to the fact that the effect of the thermal buoyancy is stronger in the hyperbolic case due to larger temperature gradients. On the other hand, the dependence on the substance is not so direct. While the larger value of Schmidt number of GaAs : Se would seem to favor a stronger advective transport, one has to take into account that the boundary layer of excess concentration in front of the interface, of size of the order of $\ell = D/v_p$, is also smaller for GaAs : Se. With regard to the longitudinal segregation, the noises considered here do not significantly alter the
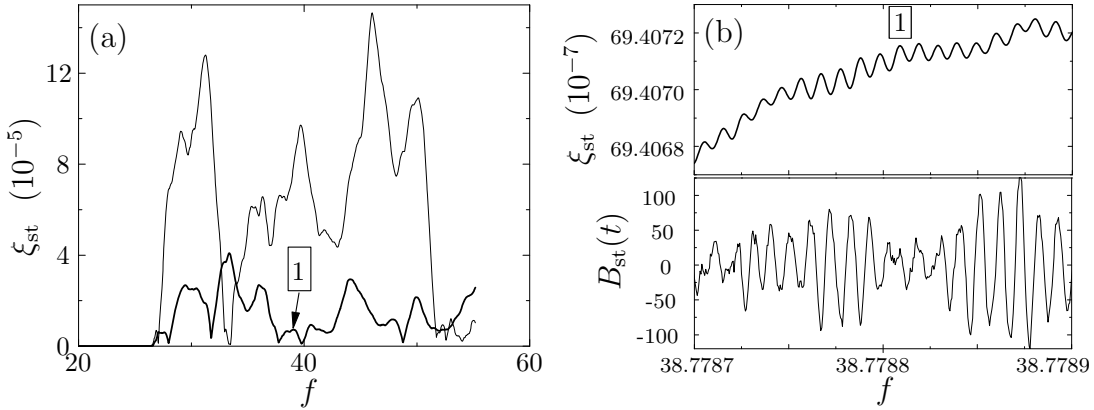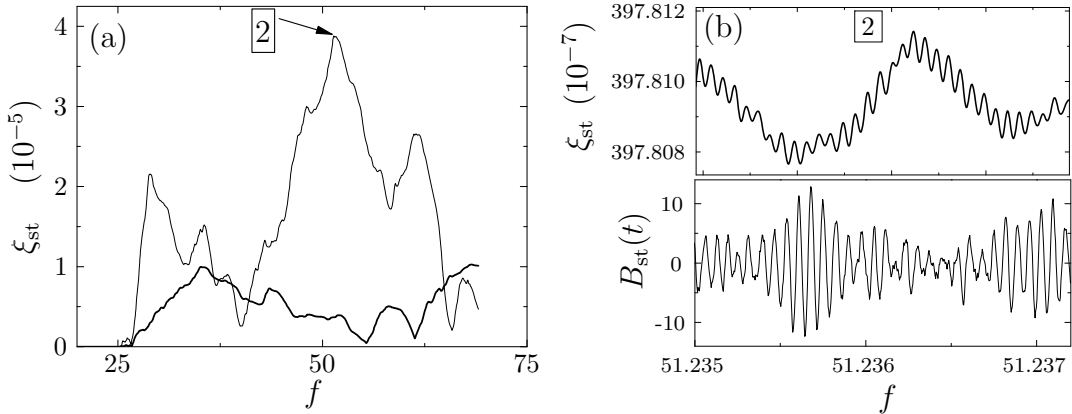
Figure 5.5: (a) Two stochastic transversal segregation realizations corresponding to linear (thick line) and hyperbolic (thin line) thermal boundary conditions in the GaAs : Se case; (b) Detail on the relation existing between the stochastic transversal segregation output (top) and the noise input -equivalently, the stochastic buoyancy factor- (bottom) for a small temporal window labeled as 2 in (a). The correlation time, $\tilde{\tau}$, and the frequency, Ω, used here for the generation of the stochastic buoyancy factor are 1 s and $40\pi s^{-1}$ respectively.

basic diffusive state, so the Smith solution fits well the computed profiles in both Ge : Ga and GaAs : Se cases. From a general perspective, it is worth remarking that, even though the power spectrum of the g-jitter is strongly peaked at Ω the response at this time scale is of very low amplitude. On the other hand, the wandering of the segregation parameter at time scales of the full experiment exhibits much larger amplitudes even though it is associated to the low-frequency part of the g-jitter spectrum, which is several orders of magnitude weaker (see Fig. 5.2). In coming sections below we will analyze this phenomenon in more detail.

While single realizations of the evolution illustrate the typical outcome one may expect in a single experiment, in order to properly characterize the quantitative response of the system to this kind of stochastic g-jitter, it is necessary to consider averages over an ensemble of independent realizations. The correct simulation of the response of the system to the whole range of time scales of the stochastic g-jitter makes the direct integration of the evolution equations highly demanding. Due to this high computational cost, we have limited the statistics of each case to 25 realizations (see additional quantitative details in Table 5.1). Results of the time-dependent averages of the different stochastic transversal segregation coefficients are shown in Figs. 5.6 and 5.7. The four curves of each figure correspond to different levels of noise intensity. The curves appear still rather noisy due to the relatively poor statistics, but show that the response is approximately proportional to the noise amplitude $\tilde{G}$. In the asymptotic steady regime, a temporal average is expected to be equivalent to an ensemble average. Therefore,
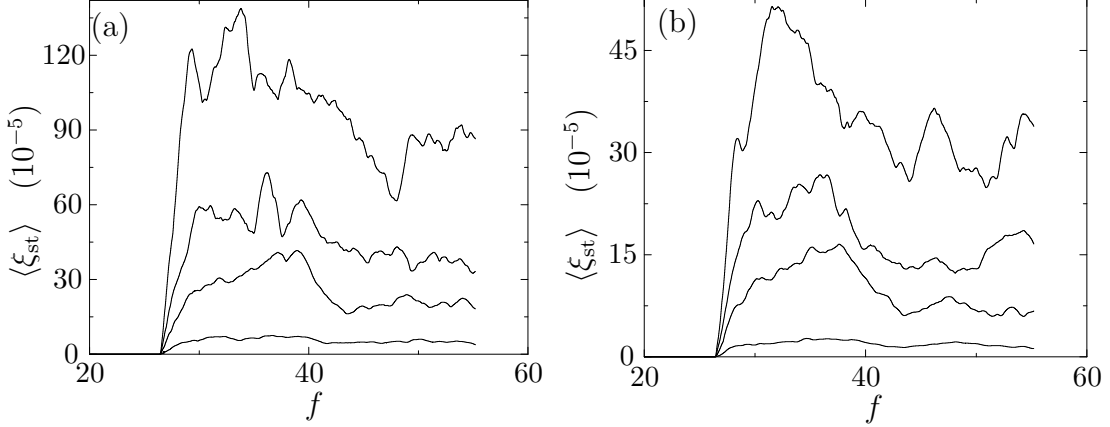
Figure 5.6: Ge : Ga averaged transversal segregation curves as a function of the per-
centual solidified fraction for four different values of the the external noise intensity.
(a) hyperbolic thermal profile, (b) linear thermal profile. The noise amplitudes $\tilde{G}$ cor-
responding to the four curves are, from top to bottom, 4×10^{-3}, 2×10^{-3}, 10^{-3} and
2×10^{-4} cm/s^2 respectively. Also, in all cases, the correlation time and the frequency
are $\tilde{\tau} = 1s$ and $\Omega = 40\pi s^{-1}$.
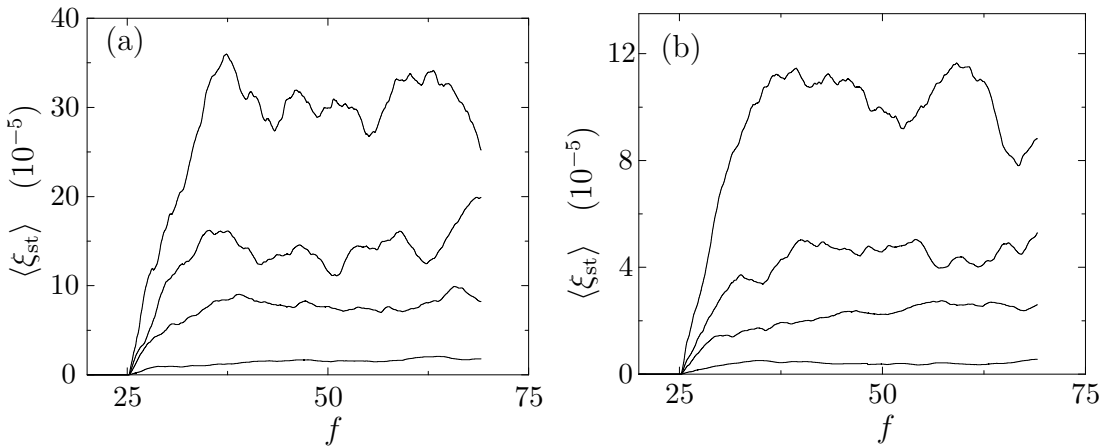
Figure 5.7: GaAs : Se averaged transversal segregation curves as a function of the
percentual solidified fraction for four different values of the external the noise intensity.
(a) hyperbolic case; (b) linear case. The noise amplitudes corresponding to the four
curves are, from top to bottom, 4×10^{-3}, 2×10^{-3}, 10^{-3} and 2×10^{-4} cm/s^2 respectively.
Also, in all cases, the correlation time and the frequency are $\tilde{\tau} = 1s$ and $\Omega = 40\pi s^{-1}$.
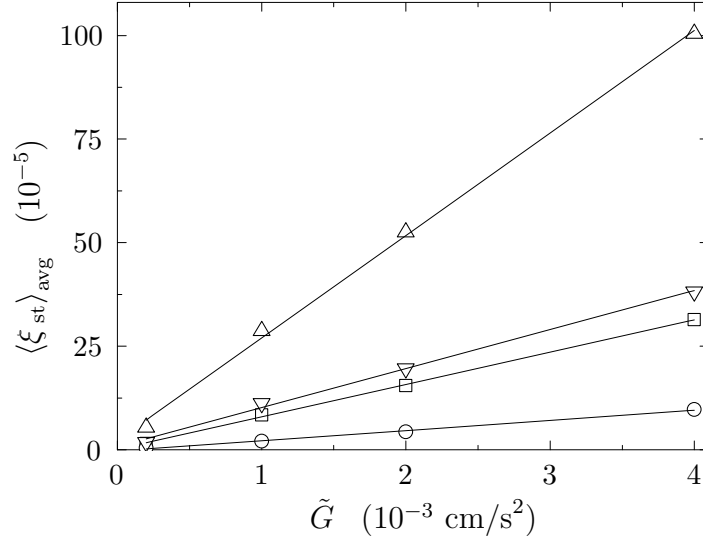
Figure 5.8: Steady state average values of the four different averaged transversal segregation curves as a function of the square root of the dimensional noise intensity. Upper and lower triangles corresponds to the Ge : Ga hyperbolic and linear cases, while that squares and circles corresponds to GaAs : Se hyperbolic and linear ones.

we may effectively improve the statistics by fitting a horizontal line in the steady part of the evolution. Then, the obtained values of the asymptotic saturation of the response do scale linearly with $\tilde{G}$, as shown in Fig. 5.8. This fact suggests that a linear response theory approach may be adequate enough for the description of the behavior of the system in all situations considered here.

5.3.3 Deterministic sinusoidal g-jitters

Since the spectrum of the narrow-band noise used in this study is quite narrowly peaked at a characteristic frequency, it is very interesting and illustrative to consider the reference case of a deterministic harmonic g-jitter with that same frequency. Thus, to compare with the stochastic results we consider a dimensionless deterministic buoyancy term of the form

$$B(t) = A\cos(\Omega t + \phi)\theta = B_{det}(t)\theta, \qquad (5.21)$$

with $B_{det}(t)$ the dimensionless deterministic buoyancy factor. In order to compare stochastic and deterministic signals with similar intensity (as long as the power spectrum is well peaked at $\pm\Omega$), we must have that A is of the order of typical maxima of $B_{st}(t)$ (see the more detailed discussion of Thomson et al. (1995)). Since we will show that the response is stronger for the stochastic case, and for $\Omega\tau \gg 1$, a conservative choice is to slightly overestimate the amplitude A to be compared to a

Figure 5.9: Two deterministic transversal segregation realizations corresponding to two different thermal boundary conditions, linear and hyperbolic, in the Ge : Ga case. Inset: Detail on the relation existing between the transversal segregation output (top) and the deterministic buoyancy factor (bottom), for a small temporal window (labeled as 1 in the main figure). Parameters of the deterministic signal correspond to the equivalence to the noisy case with a noise amplitude $\tilde{G}$ equal to 2×10^{-4} cm/s^2 (see text).

given stochastic signal by imposing that $A > B_{st}(t)$ during the whole realization. In view of Eq.(5.16), the values of B are proportional to Ra*/Pr (which is a Grashoff number based on the stochastic $\tilde{G}$ times the stochastic functions $S(t)$). But because $S(t)$, due to the employed nondimensionalizations, are proportional to the square root of Pr/τ, $B(t)$ scales with Ra*/$\sqrt{\tau\mathrm{Pr}}$. A last fit using the values of the different $B_{st}(t)$ gives the final relationship $A = 5.2\mathrm{Ra}^*/\sqrt{\tau\mathrm{Pr}}$.

The deterministic g-jitter in the simulation has been switched on in the same way as in the stochastic case. In order to properly follow the fast temporal variations of the deterministic signal the values of the corresponding time steps have been kept also the same.

As before and independently of the thermal conditions used, axial segregation remains unchanged. So, Smith's profile fits the results for both Ge : Ga and GaAs : Se cases. With regard to the deterministic transversal segregation, Figs. 5.9 and 5.10 show two examples of the results obtained. The overall effect of a
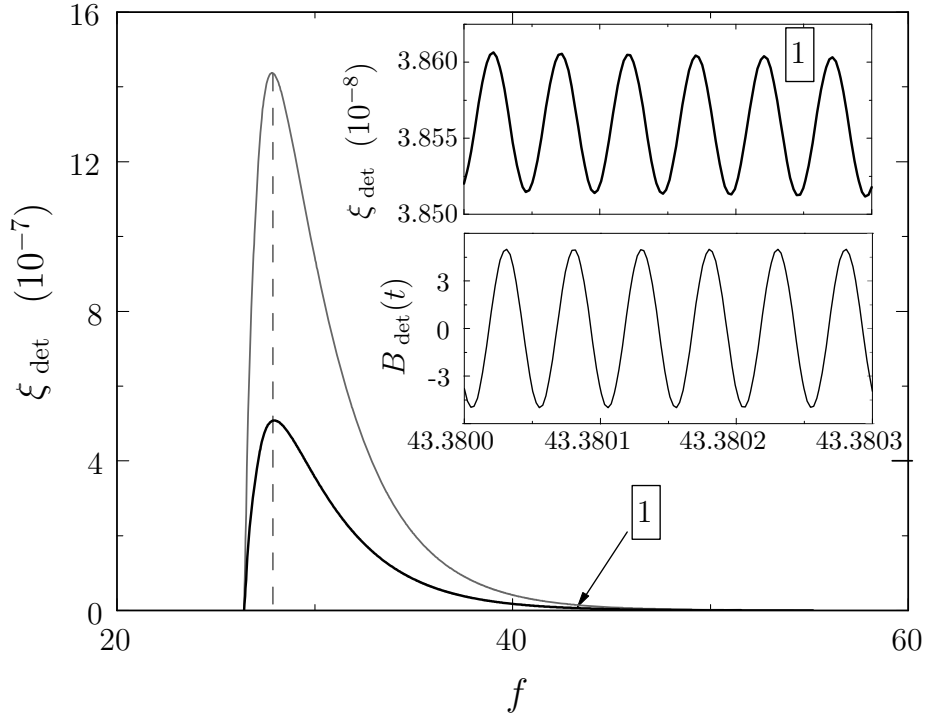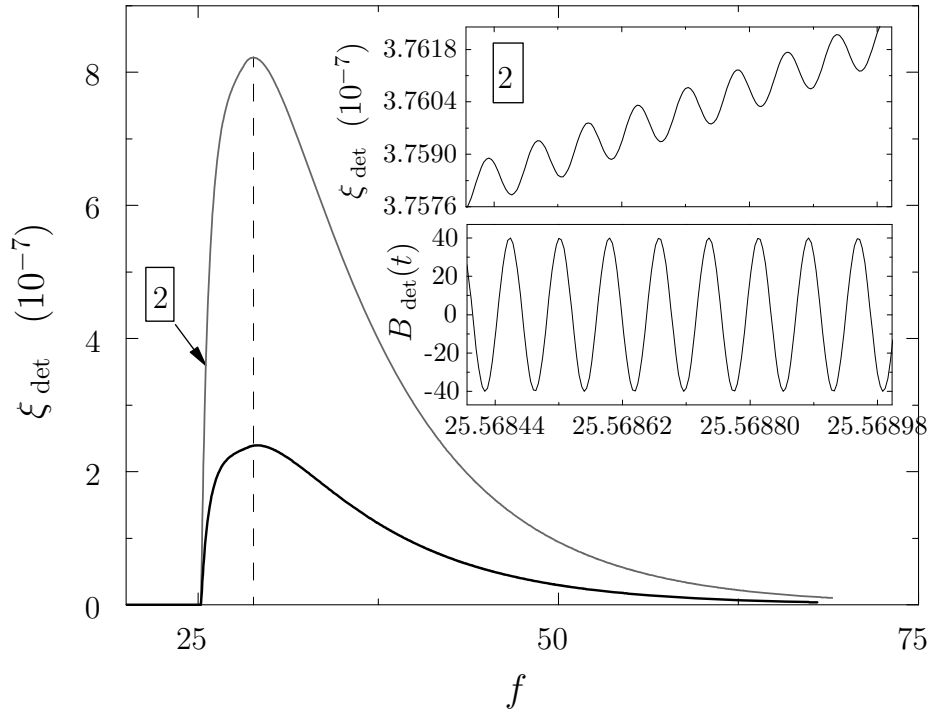
Figure 5.10: Two deterministic transversal segregation realizations corresponding to two different thermal boundary conditions, linear and hyperbolic, in the GaAs : Se case. Inset: Detail on the relation existing between the transversal segregation output (top) and the deterministic buoyancy factor (bottom), for a small temporal window (labeled as 2 in the main figure). Parameters of the deterministic signal correspond to the equivalence to the noisy case with a noise amplitude $\tilde{G}$ equal to 2×10^{-4} cm/s^2

sinusoidal forcing instantaneously switched on consists of a sudden, fast increase of the response up to a maximum value and then a slower decrease asymptotically to zero, with characteristic time scales that depend on the material, and type of boundary conditions considered. This behavior is to be compared with the stochastic one which, on average, saturates to a finite asymptotic value different from zero. The arguments used for the stochastic case apply now to explain that the Ge : Ga case is slightly more sensitive than the GaAs : Se one to this kind of perturbations and, in all cases, the hyperbolic thermal boundary condition produces a response significantly bigger than the one obtained using linear thermal conditions. Superposed to this overall envelope, small ripples with negligible amplitude appear following the oscillations of the harmonic forcing. A phase shift between the resulting segregation and the external forcing is, in general, expected as is seen in the insets of Figs. 5.9 and 5.10.

Fig.5.11 shows the dependence of the maximum of the response to the amplitude and the phase of the forcing. The dependence on the amplitude reflects the
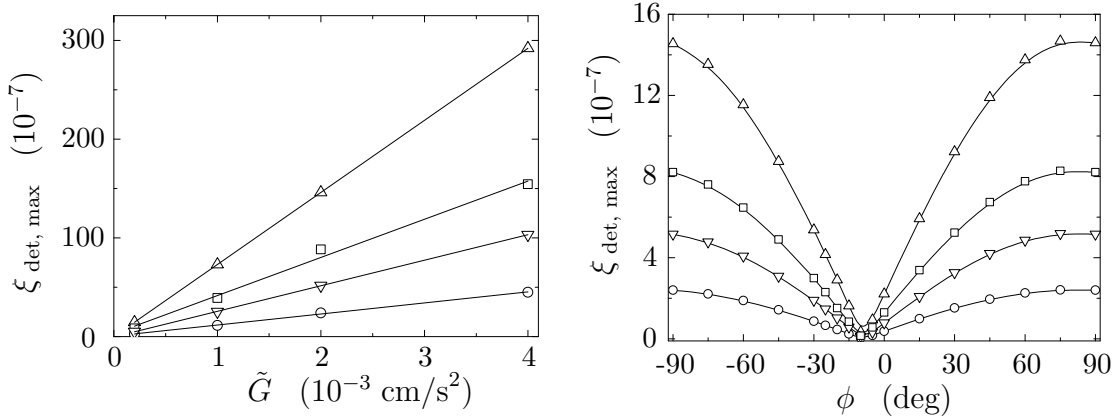
Figure 5.11: Maximum value of the transversal segregation parameter during the temporal evolution of the deterministic case, as a function of (a) the square root of the equivalent noise intensity, (b) the phase of the harmonic perturbation. Upper and lower triangles corresponds to the Ge : Ga hyperbolic and linear cases, while that squares and circles corresponds to GaAs : Se hyperbolic and linear ones. The deterministic amplitudes A used here correspond to the four noise intensities employed for the noisy case by employing the appropriate proportionality factors (see text).

validity of linear response theory. Remarkably, the dependence of the response on the phase of the forcing is very strong, with a very pronounced minimum at a phase close to zero. The reason behind this behavior and the other observed features in both stochastic and deterministic cases will become clear in the following section, where a simple analytical model of the system will be discussed. As a general observation, we point out that the overall response is significantly smaller in the deterministic case than in the stochastic one, as shown in Fig. 5.12, as a consequence of the different low-frequency content of the two type of perturbations.

Remarkably, the ratio of the average segregation in the stochastic case to the maximum of the deterministic one remains roughly independent of the forcing intensity and of the type of thermal boundary conditions. However, a significant dependence of this ratio on the substance is obtained. Specifically, the case of Ge : Ga seems to have a larger ratio of the stochastic to deterministic response. This dependence must be traced back to the interaction with the low-frequency part of the spectrum, which in turn depends on the characteristic time scales of dissipation of each substance, as described in the following section.

As a final comment, it is worth stressing that the resulting segregation parameter values corresponding to the action of the accelerometric signals employed in this work, modeled from real g-jitter measurements in microgravity platforms [Thomson et al. (1997)], result in principle to be sufficiently small to be neglected
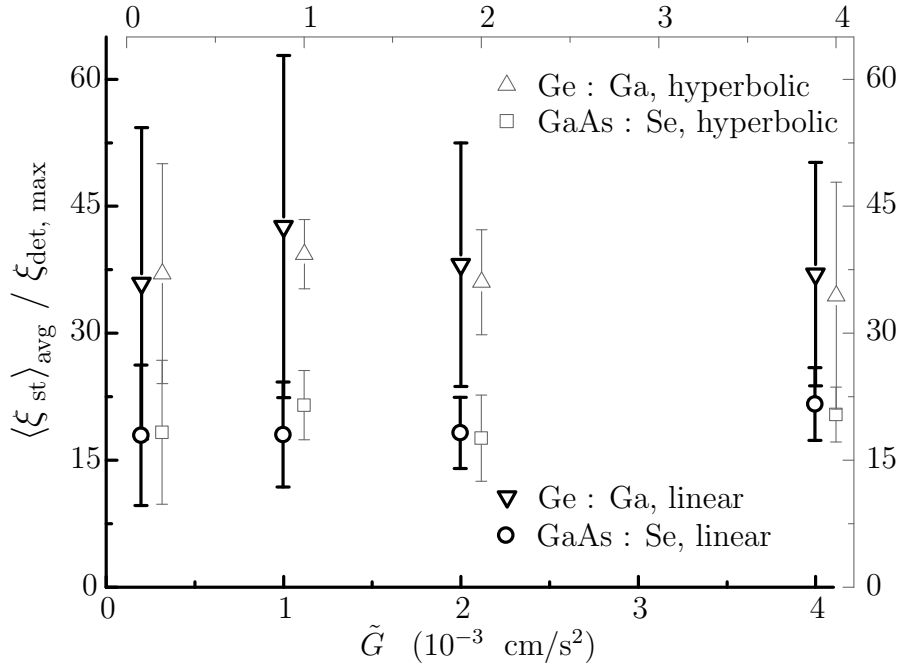
Figure 5.12: Ratio of the averaged transversal segregation rate of the noisy case to the maximum of the deterministic one, for the different simulated systems, as a function of the signal amplitudes. The error bars associated to each one of the averaged transversal segregation curves have been calculated evaluating the standard deviation of the data against the mean value in the corresponding asymptotic steady regime.

for most practical purposes. However, as it has just been mentioned, the analysis of the system to be done in the next section will show the importance of the low frequency components of the gravity, which for real signals could differ substantially. We will come back to this point below. The modeling to be developed in the next section, which will be tested with the previous results, will permit to make quantitative predictions for arbitrary noise statistics or for particular time-dependent signals.

5.4   Heuristic model

5.4.1   Definition of the model

In this section we will show that all the above phenomenology in the response of the concentration field to the present acceleration environment can be captured with remarkable accuracy by an extremely simple heuristic model. In addition to

the theoretical insight into the dynamical behavior of the system, this simplified model will provide an interesting predictive tool where the effects of any given acceleration signal from real data, could be tested without relying on the full numerical integration of the problem.

The model starts by assuming a linear response of the flow field to the buoyancy force, which is justified because the forcing induced by the residual acceleration is assumed to be small. The linearized equation for the vorticity, in the frame moving with v_p, takes the simple form

$$\frac{\partial \vec{\omega}}{\partial t} = v_p \frac{\partial \vec{\omega}}{\partial x} + \nu \nabla^2 \vec{\omega} + \vec{g}(t) \times \vec{\nabla}\rho, \qquad (5.22)$$

where ρ is the mass density. In general the density gradient contains contributions from both thermal and solutal gradients, but in our problem the thermal contributions to buoyancy are strongly dominant and we can neglect the dopant concentration gradients in Eq.(5.22). To linear order the density gradient is given by the unperturbed problem, which because of the small values of Prandtl number, will remain essentially constant in time after a very short transient.

As a result the spatial structure of the buoyancy term will define the spatial structure of the response. Extending the heuristic analysis of Thomson et al. (1995), the basic point is that the vorticity generated by the buoyancy acquires a single-vortex structure as for weak natural convection. This will combine, in general, different eigenmodes of the cavity, but we assume that it will be dominated by a single slow mode. The characteristic time scale of this slow mode must be of the order of a viscous relaxation time.

Within the same spirit, we assume that the strength of the coupling of the buoyancy term is also characterized by a single parameter F. This yields a simple equation for the amplitude of the single-vortex mode of the form

$$\dot{\omega} = -a\omega + FB(t), \qquad (5.23)$$

where both a and F can be estimated but can be more precisely fitted from numerical simulations of the full problem. The accelerometric signal $B(t)$ corresponds to what previously denoted by $B_{st}(t)$ or $B_{det}(t)$. $B(t)$ can in principle be an arbitrary function of time of order one but, once the problem has been linearized, it will be sufficient to study sinusoidal dependences of it. Note that, by construction, such a simple model is not expected to capture the correct response to the very high-frequency components of the signal.

Since the thermal field is essentially decoupled from the flow for our values of Prandtl number, we only need to couple the flow field to the solute transport. We are thus left with the linearized equation for the concentration departure from the

steady profile as $\delta c(x, y) = c(x, y) - c_0(x)$ which, in the frame moving with the solidification velocity v_p, takes the form

$$\frac{\partial \delta c}{\partial t} = v_p \frac{\partial \delta c}{\partial x} + D\nabla^2 \delta c - \delta \vec{v} \cdot \vec{\nabla} c_0, \tag{5.24}$$

where the velocity field $\delta \vec{v}$ is small, given by the order of $\vec{\omega} \equiv \vec{\nabla} \times \delta \vec{v}$. In principle the unperturbed profile is weakly time-dependent during the experiment. This is expected to have a small effect, in particular in the time window here explored, which excludes the initial stages of the concentration build-up in front of the interface, where this time dependence may be more significant. We will see *a posteriori* that this assumption is justified. Then, consistently with the simple response to buoyancy of the flow field, we may expect that an effective description in terms of an amplitude for the concentration distortion with a single relaxation time may capture the dominant large-scale and long-time behavior of the concentration distortion.

The coupling with the flow field is described by the last term of Eq. (5.24). Consistently with the single-mode effective description, this term reduces to a linear coupling between the amplitude of the concentration mode and of the vorticity mode. This leads to an equation for the amplitude c of the concentration disturbance of the form

$$\dot{c} = -bc + \gamma'\omega, \tag{5.25}$$

where b and γ' are also parameters to be fitted from the full equations. The time scale associated to b will necessarily be a characteristic diffusion time of the solute. For times smaller that b^{-1} the coupling term proportional to γ' in Eq. (5.25) describes the advection of the concentration by the fluid motion. At longer times, the inhomogeneity created must be relaxed by solutal diffusion.

Combining the two Eqs. (5.23) and (5.25) we get

$$\ddot{c} + (a + b)\dot{c} + abc = \gamma B(t), \tag{5.26}$$

where we have defined $\gamma \equiv \gamma' F$. We therefore get a simple ordinary differential equation, that of a forced harmonic oscillator with damping, for the temporal evolution of a single variable $c(t)$, the amplitude of the main mode of the concentration distortion, and whose absolute value should be related to the segregation parameter evaluated for the complete system in previous sections. This simplified model depends on three parameters: a and b, related to dissipative temporal scales of the system, and γ, which couples the $c(t)$ variable to the actual accelerometric signal, and thus provides the scale for the response to the forcing. We will see that this extremely simple description explains remarkably well many of the observed features in the full direct numerical simulation of the problem, not

only at a qualitative level but also quantitatively to a remarkable extent. The set of parameters of the model are expected to be characteristic of the specific material and setup configuration, but independent of the type of time dependence of the forcing. Therefore, if suffices to determine the model parameters from a single simulation for each case. Then, as long as this reduced linear response model is sufficiently accurate, the same parameters will serve for any arbitrary time-dependence of the forcing [2]. The order of magnitude of the parameters a and b can be estimated from simple dimensional analysis. The relaxation time of the vorticity for instance, must take the form of $a^{-1} \sim \Lambda_\omega^2/\nu$, where Λ_ω is a characteristic scale of the problem in the longitudinal direction, since for our large aspect ratio, the vorticity relaxation in much faster in the transversal direction.[3] Similarly, for solutal diffusion we must have $b^{-1} \sim \Lambda_c^2/D$. In this case however, the relevant longitudinal length scale is essentially given by the diffusion length $\ell_D = D/v_p$, which is smaller than H so, in our cases it is the transversal diffusion which is the dominant relaxation mechanism. We will see in the following sections that the actual parameters a and b that best fit the full simulations are indeed insensitive to the intensity of the forcing and to the actual thermal boundary conditions and, consistently with the above dimensional analysis, they depend only on the geometry and the material parameters (see Table 5.2).

5.4.2   Periodic forcing

If we assume a periodic forcing of the form $B(t) = A\cos(\Omega t + \phi)$, with the initial conditions $c(0) = 0$ and $\dot{c}(0) = 0$, the solution of Eq. (5.26) reads

$$c(t) = c_1 e^{-at} + c_2 e^{-bt} + c_0 \cos(\Omega t + \phi - \delta), \qquad (5.27)$$

---

[2]In situations where the transient dynamics of the unperturbed concentration layer in front of the interface can not be neglected, for instance if the time-dependent gravity is switched on from the start of the experiment, an appropriate, slow time-dependence of $\gamma(t)$ can be assumed to improve the analysis

[3]Note that, since L is time dependent, the vorticity relaxation time is in principle slowly time dependent too. The results obtained in the fitting procedure for a in the following sections are thus effective values and may differ for distinct substances, even though the vorticity relaxation is in principle decoupled from the solutal concentration dynamics. That is, the effective value of a obtained from the evolution of the concentration field may encompass a history dependence that in turn is controlled by the solutal time scales.

where the constants c_1, c_2, c_0 and δ are given by

$$c_1 = \frac{c_0}{a-b}\left(b\cos(\phi-\delta) - \Omega\sin(\phi-\delta)\right), \tag{5.28}$$

$$c_2 = \frac{-c_0}{a-b}\left(a\cos(\phi-\delta) - \Omega\sin(\phi-\delta)\right), \tag{5.29}$$

$$c_0 = \frac{\gamma A}{\sqrt{(ab-\Omega^2)^2 + [(a+b)\Omega]^2}}, \tag{5.30}$$

$$\delta = \tan^{-1}\frac{\Omega(a+b)}{ab-\Omega^2}. \tag{5.31}$$

To gain insight into this solution, it is useful to consider the physically relevant limit $\Omega \gg a, b$, i.e. gravity oscillations are rapid compared to the scales of the response of the system. Then we can write down an approximate solution as

$$c(t) \simeq \frac{\gamma A}{\Omega}\frac{\sin\phi}{(a-b)}\left(e^{-bt} - e^{-at}\right) + \frac{\gamma A}{\Omega^2}\cos(\Omega t + \phi - \pi). \tag{5.32}$$

The form of this solution as a function of time, given essentially by the first term of the r.h.s. of Eq. (5.32), is very similar to the responses obtained by numerical simulations of the complete system, as shown for instance in Figs. 5.9 and 5.10. It presents a monotonous increase from zero, with initial slope $-\gamma A \sin\phi/\Omega$. In fact, even though the average acceleration is zero, the phase of the cycle at $t = 0$ provides in general an overall drift that is independent of a and b (as seen also by Thomson et al. (1995)). At the appropriate time scales, dissipation will take over to stop and reverse the growth of concentration distortion. The response thus reaches a maximum and then it decays to zero again asymptotically controlled by in the time scale $max(a^{-1}, b^{-1})$. Superposed to this shape, we must add the oscillatory part of the solution (last term of Eq. (5.32)), which has much smaller amplitude, and thus appears as a small, fast ripple of the solution as obtained in the full numerical simulation, although the phase of this oscillation with respect to the forcing cannot be captured by our low-frequency model.

Remarkably, the strong dependence of the system response on the initial phase ϕ of the forcing as seen in Fig. 5.11b is perfectly explained by our heuristic model. Given the dissipative time scales, the value of the maximum of the time-dependent response will depend directly on the initial growth of the response, which in turn is controlled by the initial phase. One expects maximal and minimal response near the extreme and the zeros respectively of the $\sin\phi$ factor of the approximate solution, i.e. maximal near $\phi = \pm\pi/2$ and minimal near $\phi = 0$. This is exactly what is observed in the full numerical results, as shown in Fig. 5.11b.

We will make use of this deterministic oscillating case to find the parameters a, b, γ of the effective model Eq. (5.26). To simplify the procedure we employ

the prediction of Eq. (5.27), but without the oscillating term, which becomes irrelevant for this purpose. The fitting function is then

$$c_{\text{fit}}(t) = c_1 e^{-at} + c_2 e^{-bt}, \tag{5.33}$$

with c_1, c_2 given by Eqs. (5.28-5.31). Then it is easy to fit a, b and c_0 for a single accelerometric signal, and find the third model parameter γ by using Eq. (5.30). An example of this nonlinear fitting can be found in the inset of Fig. 5.13. There we fit this function to the complete solution for GaAs : Se (thick line) in the hyperbolic case, with an oscillating forcing corresponding to $\tilde{G} = 4 \times 10^{-3}$ cm/s^2 and $\phi = -\pi/2$. For details about the quantitative values of all fittings, see Table 5.2. Notice the low values of the auxiliary parameter c_0 for both substances due to the low intensities of the noises used. Also note that the values of a, b and γ are dependent on the used substance but practically constant independently of the noise intensity. This agrees well with the fact that these parameters are related with intrinsic scales of the system, independently of the external forcing. In principle one could use a single fit for each given substance and geometry to find the corresponding parameters a, b, γ of the model and apply it to any other accelerometric signal.

5.4.3   Stochastic forcing

We now consider the case in which the accelerometric signal $B(t)$ is a narrow-band noise as defined in Eqs. (5.6) and (5.7). To this end we can integrate by standard ODE methods (fourth order Runge-Kutta) the heuristic model defined by Eq. (5.26) and the fitting parameters obtained with the deterministic case. We can now compare the simulation with the complete model and the heuristic approximation, using exactly the same time-dependent signal $g(t)$. The results are shown in Fig. 5.13.

Note that the agreement is very good, not only in the magnitude, but even in the detailed shape of the response. Given the extreme simplicity of the heuristic model, this level of agreement of both simulations is remarkable. We see that this heuristic approach can become a powerful predictive tool when the aim is to elucidate the effect of different time signals for $B_{st}(t)$, in particular if the forcing is stochastic and therefore some statistics are required. Note that the computational demands for the heuristic model have been dramatically reduced by several orders of magnitude with respect to the complete problem.

We can gain further insight on the behavior of the physical system by analyzing more in detail the properties of the model given by Eq. (5.26). In particular, the response of the system can then be worked out from the response function of
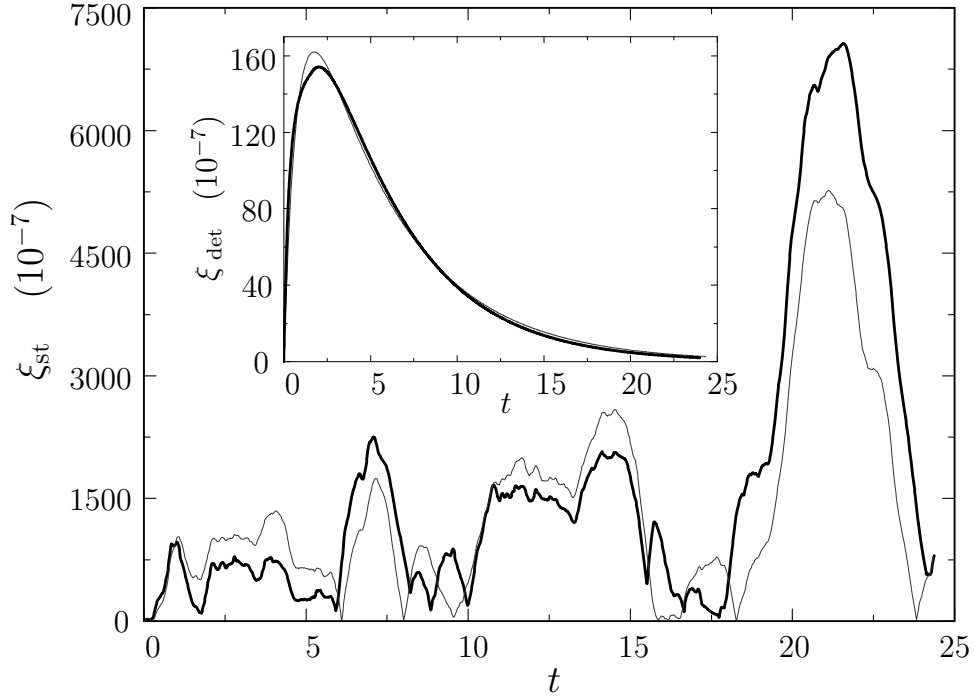
Figure 5.13: Stochastic transversal segregation parameter as a function of time, for GaAs : Se, obtained from both the complete simulation (thick line) and the integration of the heuristic model (thin line) by employing the same noisy signal. Inset: nonlinear fitting of Eq. 5.33 to the simulation of the complete model for the deterministic case, which is used to obtain the value of the three parameters needed in the noisy case.

Eq. (5.26) and in terms of a generic power spectrum of the noise $P(\omega)$. Specifically, the variance of the $c(t)$ variable in the steady state is given by

$$\langle c^2 \rangle = \gamma^2 \int_{-\infty}^{+\infty} \frac{d\omega}{(\omega^2 + a^2)(\omega^2 + b^2)} P(\omega).$$ (5.34)

For the power spectrum of narrow-band noise Eq. (5.6), and in the limit $\Omega \gg a, b$, this takes the simple form

$$\langle c^2 \rangle \simeq \gamma^2 \frac{\pi}{ab(a+b)} P(0).$$ (5.35)

This expression can be computed easily and reads

$$\langle c^2 \rangle \simeq \frac{\gamma^2}{ab(a+b)} \frac{\text{Ra}^{*2}}{\text{Pr}} \frac{1}{1 + \tau^2 \Omega^2}$$ (5.36)

Corrections of higher order in $a/\Omega, b/\Omega$ can be explicitly computed, but they are uninteresting for the present discussion. What is of importance here is that in view

of Eq. (5.35) it is apparent that the response of the system will depend basically on the low-frequency limit of the noise spectrum.

This fact is remarkable, since the zero frequency component can be a very small contribution to the total noisy signal. This is particularly true for narrow-band noise, for which the power spectrum is dominated by the main peaks at the nominal frequency, $i.e.$ $\pm\Omega$ (see Fig. 5.2). Note that the narrow-band noise, for the relatively large correlation times considered here, is similar to a monochromatic noise with some wandering in phase and amplitude. The key point here is that, while in the deterministic monochromatic signal the scale of the effect on the system was given by its amplitude A, which is related to the area of the peak at $P(\omega = \Omega)$ of a similar narrow-band noise, the main contribution to the effects of the narrow-band noise is given by the value of $P(0)$, and not by $P(\Omega)$. In other words, if we compare two signals with roughly the same frequency and amplitude, one deterministic and the other noisy, the response of the system will be significantly different, and will be stronger for the noisy signal, which has a zero-frequency component that is small but non-zero, compared to the deterministic monochromatic signal, which gets the low-frequency components only from the initial switch-on. We can see that in Fig. 5.12, where we plot the rate of the mean value of the transversal segregation parameter in the steady state of several noisy cases to the maximum of the deterministic response in their corresponding cases. In all cases the response to the narrow-band noise is one to two orders of magnitude larger than to the deterministic oscillations.

We should also stress that the parameters of the narrow-band noises [Thomson et al. (1997)], while obtained from accelerometric signals in real microgravity environments, were estimated to mainly model the principal frequency components of the accelerometric signal. The specific zero frequency components and hence the system responses are thus possibly underestimated. The results above call then for a more detailed characterization of real signals, in particular for low frequencies, which could be present to a much larger extent than in the narrow-band noises employed here. Note also that, in view of the system sensitivity to the low frequencies, the possible presence of a small constant component superposed to the stochastic signal could have a strong effect in the response of the system. To assess whether that is the case, depending on the system parameters, one should compare the solution for the noisy case in Eq. (5.35) to the solution of the model Eq. (5.26) for a constant forcing. It is easy to show that a constant buoyancy B, superposed to a fluctuating one with power spectrum $P(\omega)$, will indeed be dominant if $P(0) \ll B^2(a^{-1}+b^{-1})$, $i.e.$ the effect of the constant term depends on the longest of the temporal scales of the problem, as long as the system is let to reach its steady state. For a shorter temporal window, the same condition applies but by employing as temporal scale the duration of the window.
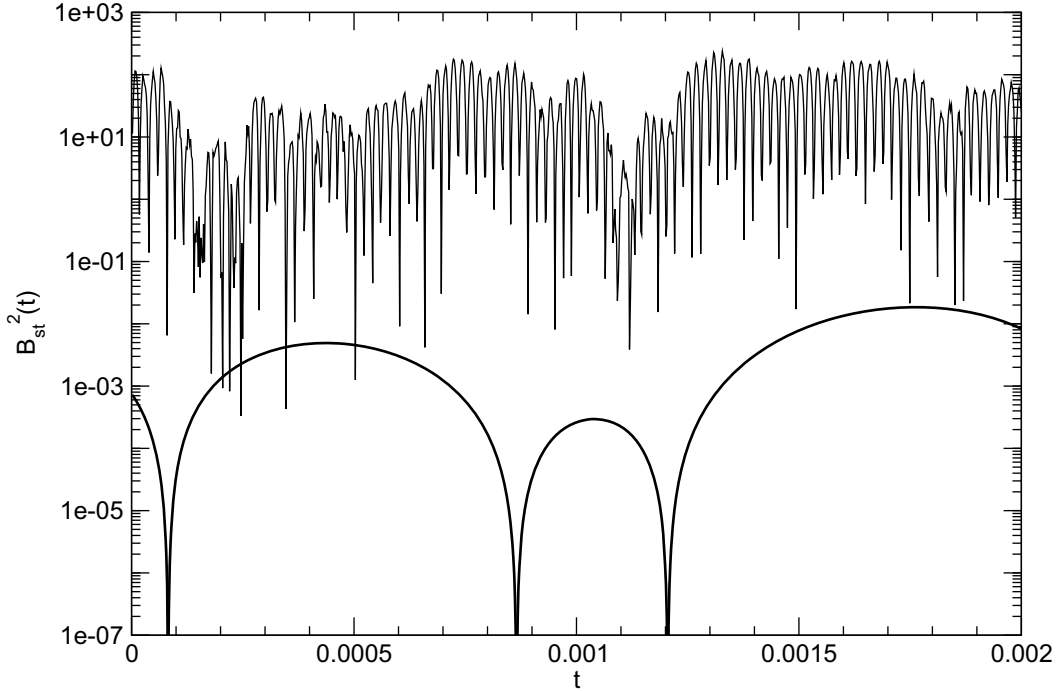
Figure 5.14: Square of the noise as a function of time, in logarithmic scale and in dimensionless units. Thin line: Both filtered and non-filtered signals (they superpose and are indistinguishable at this scale); Thick line: filtered low frequency component, corresponding to the difference between both signals (see text).

To further illustrate the effect of the low-frequency region of the spectrum we perform a very illuminating test. Given an appropriate separation of scales (peak width much smaller than the dominant frequency, i.e. $\Omega\tau \gg 1$), for a narrow-band noise the filtering of small frequencies gives a signal apparently indistinguishable from the original signal, but which in light of Eq. (5.35) should produce very different results when applied to the system. To show that, we have performed the filtering of a narrow-band signal with amplitude 2×10^{-4} cm/s^2, removing frequencies in a small window around the zero frequency (namely all frequencies smaller than $\Omega/35$.). We have then applied both signals (filtered and non-filtered) to both the complete and the heuristic models for the GaAs : Se case. The comparison of both signals is shown in Fig. 5.14. They are effectively indistinguishable when represented at the scales of the typical values of the signals themselves. We have also represented the difference between both signals. We see that the difference is several orders of magnitude smaller than the signals themselves, and of a very slow temporal dependence. In Fig. 5.15 the responses of the models are shown. Remarkably, we see that both filtered and non-filtered signals, apparently so similar to the eye, produce completely different responses when applied to both models.
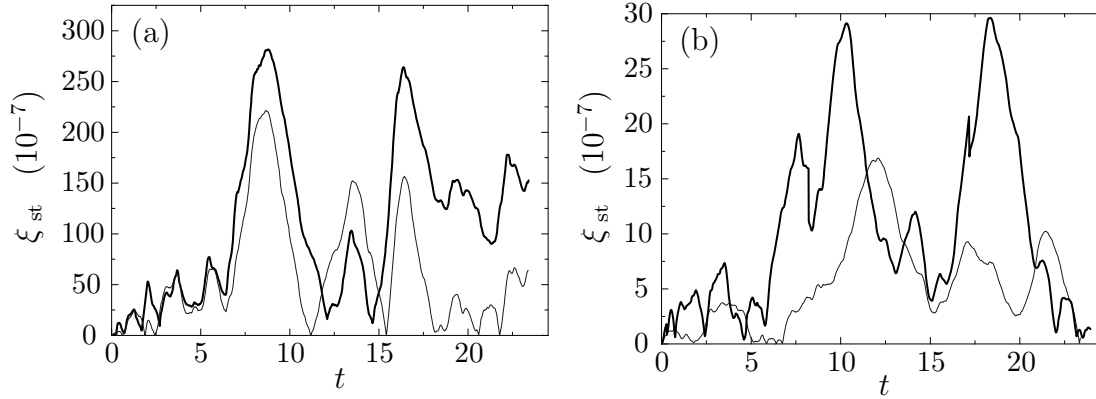
Figure 5.15: Comparison between the transversal segregation signals obtained using the complete problem (thick lines) and the heuristic one (thin lines) for a noise with low frequencies (a) included, (b) excluded.

This test also visualizes that the comparison between the complete model and its heuristic approximation is not quite satisfactory when the low-frequency filter has been applied to the stochastic signal. This is an indication that the heuristic model, which has reduced the description effectively to slow modes, is essentially a low-frequency approximation and obviously, it cannot be expected to capture the whole richness of the complete problem. The bottom line is thus that, as long as there is a significant (even small) low-frequency content of the g-jitter, this will be dominant and therefore the heuristic model will provide a reasonably accurate approximation of the system response, and explain all the phenomenology observed when changing the substance and the boundary conditions in terms of the two corresponding time scales to be fitted in each case. This is quite remarkable given the drastic simplification of the system description.

5.5   Conclusions

We have addressed the effects of a generic stochastic g-jitter into some realistic experimental setups for semiconductor crystal growth in microgravity. Specifically we have studied directional solidification of two semiconductor melts with a diluted dopant. We have compared direct numerical computation of the full problem in the presence of narrow-band noise and periodic deterministic signals of comparable intensity, showing that the segregation parameter that measures the resulting

Magnitude	.	Ge : Ga	GaAs : Se	Units
Cell height	H	2.5	2.5	cm
Aspect ratio	AR	4	4	$\frac{L(0)}{H}$
Final solidified fraction	F	55	68	$\%L(0)$
Kinematic viscosity	ν	1.30×10^{-3}	4.88×10^{-3}	cm^2/s
Diffusion coefficient	D	1.9×10^{-4}	4.5×10^{-5}	cm^2/s
Thermal diffusivity	α	1.82×10^{-2}	7.17×10^{-2}	cm^2/s
Segregation coefficient	k	0.087	0.3	-
Relative wall diffusivity	α_r	5.9×10^{-2}	15.1×10^{-2}	(α_{amp}/α)
Front velocity	v_p	$1. \times 10^{-4}$	1.4×10^{-4}	cm/s
Prandtl number	Pr	7.15×10^{-3}	$68. \times 10^{-3}$	(ν/α)
Schmidt number	Sc	6.8	108.4	(ν/D)
Peclet number	Pe	19.2×10^{-2}	7.2×10^{-2}	(VH/ν)
Amplitude of the gravity signal	$\tilde{G}$	$(2-40) \times 10^{-4}$	$(2-40) \times 10^{-4}$	cm/s^2
Correlation time ($\tilde{\tau} = 1s$)	τ	2.1×10^{-4}	7.8×10^{-4}	$\frac{\tilde{\tau}\nu}{H^2}$
Characteristic period ($T^* = 0.05s$)	T	1.0×10^{-5}	3.9×10^{-5}	$\frac{T^*\nu}{H^2}$
Stochastic Rayleigh number	Ra^*	$0.117 \ldots 2.34$	$0.054 \ldots 1.072$	$\frac{\beta^T \Delta T \tilde{G} H^2}{\nu}\sqrt{\frac{\tilde{\tau}}{\alpha}}$
Time step	Δt	$5. \times 10^{-7}$	1.95×10^{-6}	-
Total points used in each realization	N	1.25×10^7	1.25×10^7	-
Number of NBN considered in the ensemble average of independent realizations	-	25	25	-

Table 5.1: Definition and numerical values of the different parameters used.

$G\ (10^{-4}\ \mathrm{cm/s^2})$	2	10	20	40
$Ge : Ga$				
a	5.57 / 6.27	5.57 / 6.27	5.57 / 6.27	5.57 / 6.27
b	1.437 / 1.488	1.437 / 1.488	1.437 / 1.488	1.437 / 1.488
$c_0 \times 10^{10}$	1.179 / 4.248	5.894 / 21.24	11.79 / 42.48	23.58 / 84.96
$\gamma \times 10^2$	8.606 / 31.01	8.605 / 31.01	8.605 / 31.01	8.605 / 31.01
$GaAs : Se$				
a	1.199 / 1.281	1.197 / 1.281	1.198 / 1.281	1.197 / 1.281
b	0.186 / 0.189	0.186 / 0.189	0.186 / 0.189	0.186 / 0.189
$c_0 \times 10^{12}$	2.564 / 10.00	12.78 / 49.97	25.61 / 99.96	51.13 / 199.9
$\gamma \times 10^3$	1.738 / 6.780	1.733 / 6.774	1.736 / 6.776	1.733 / 6.773

Table 5.2: Quantitative results of the different fittings effected in this work. For each substance and configuration a single run using a deterministic signal with $\phi = -\pi/2$ has been employed. Left / right hand side corresponds to a linear / hyperbolic thermal arrangement.

quality of the crystal becomes larger in the case of stochastic forcing, although in general it remains sufficiently small for practical purposes. This first indication of the importance of the low-frequency domain of the forcing signal has been analyzed in detail with the help of a reduced description of the system that has turned out to be a remarkably accurate modeling of the system response to arbitrary time-dependent g-jitter. The model involves two effective time scales, one from viscous dissipation and one from solutal diffusion. Those can be fitted from the simulation of a single convenient case, and on the basis of linear response theory, the model can be extended to arbitrary signals. The accuracy of this model has been checked in representative cases. The combination of the analytical insights from this approximation, and the full computation of the complete problem in a variety of cases yields the two main conclusions of this work. First, we show that the low-frequency part of the g-jitter spectrum is dominant with respect to the overall response of the system, even if orders of magnitude smaller than other high-frequency components. Consequently, it would be very interesting to have access to details of accelerometric signals other than the main frequency components (those modeled by the narrow-band noise parameters), in particular with regard to the low frequency part of the spectrum. Consistently, if a small non-zero steady gravity component g is present, its effect in the segregation parameter may be significant. The low-frequency component $P(0)$ of the stochastic background will only dominate over the constant term if $P(0) \gg g^2 T$, where T is the longest characteristic time of the system or the time window of observation, whichever is smaller. Second, we show that a two-time scale linear response reduction of the problem is quantitatively accurate and independent of the type of time-dependent signal, for each given set of material parameters and boundary conditions. This

simplified modeling, which defines a low-frequency approximation of the linear response of the system, may potentially loose accuracy in those situations where the low-frequency components are not present or have been filtered out. For most practical situations, however, the heuristic model proposed provides a remarkable numerical tool to reasonably predict the behavior of such systems under arbitrary forcing without relying on very demanding numerical computation.

Chapter 6

Conclusions and perspectives

6.1 Summary of results and publications

Here we briefly revisit the main results and conclusions of this thesis in an itemized summary:

- We have developed a state-of-the-art Lattice-Boltzmann code capable to study relatively high levels of three-dimensional turbulence, around $Re \sim 10^4$ for pipe flows. We have parallelized it and tested it satisfactorily against recent results in the literature. In particular, we have introduced and explored a simple filtering procedure to suppress some numerical instabilities at high Reynolds numbers. With this code we have reproduced the conditions of experiments on duct flows for a simple liquid, in the absence of bubbles, as a reference state for comparison with the experiments performed with bubbles. In particular we have obtained and fully characterized steady turbulent flows for the cases of $Re = 3800$ and $Re = 12700$.

- We have developed an effective stochastic model for turbulent bubble jets, based on the k-ε approach to turbulence, with a local diffusivity depending on the local degree of turbulence. The model treats bubbles as passive tracers and is only expected to be correct asymptotically downstream. We have solved it using finite-volume techniques with the commercial software FLUENT. We have also performed systematic particle-tracking analysis of the drop tower experiments of Carrera et al. (2008), and obtained data for the statistics of the spatial distribution of bubble density, bubble velocity and dispersion of bubble velocity.

- We have obtained that the k-ε model accounts reasonably well for the overall structure of jets, specifically for the three statistical observables studied,

except for a few centimeters from the injection point. The model fails at predicting the opening angle of the bubble jet and its (weak) dependence with the Reynolds number. Bubbles at the margins of the jet exhibit relative velocity fluctuations that decrease for increasing Re, as opposed to the prediction of the k-ε model. The failures of the model occur at the jet margins, suggesting that the approach does not capture the correct physics of the boundary between turbulent and laminar flow, while bubble dispersion near the jet boundaries seems to be sensitive to that.

- We have achieved for the first time the experimental realization of a homogeneous suspension of monodisperse, highly spherical bubbles, in a turbulent carrier flow with controlled Reynolds number, in microgravity conditions. This proof of concept is the most innovative aspect of this thesis. We have defined and checked a method that allows to control different statistical and flow parameters separately, including bubble size, bubble density, and degree of turbulence of the liquid carrier. The method exploits the T-junction slug-flow generation introduced by Carrera et al. (2008). This has been achieved for bubble sizes in the millimeter range, $Re \sim 10^4$, and void fractions of few percents. Optimal performance of the injection system has been achieved for bubbles in the range between 1.6 and 2.5 mm of diameter.

- We have monitored and characterized quantitatively for the first time the decay of pseudo-turbulence (i.e. the excess turbulence generated by buoyant bubbles) as gravity is instantaneously switched-off. Bubble columns formed under buoyancy forces spread quickly to a homogeneous suspension. Bubbles relax to the local fluid velocity in the time scale of their viscous relaxation $\tau_B < 0.2$, while the mean velocity of the flow in our typical conditions relaxes with a larger characteristic time of 1.0 s. For cases with a co-flow of $Re = 6000$, velocity fluctuations of the pseudo-turbulence in the directions longitudinal and transversal relax with characteristic times of 3.2 s and 2.4 s, respectively. For stronger turbulence ($Re = 13000$) we have not measured a significant change in the velocity fluctuations, probably due to the relative less significant effect of the pseudo-turbulence.

- We have performed systematic particle-tracking analysis of the high-speed movies of the experiments on turbulent bubble suspensions, with focus on the statistics of mean velocity profiles and in particular on the relative dispersion of bubble velocities. In addition to the pseudo-turbulence transient, our results seem to observe a tendency of the relative velocity fluctuations to decrease for increasing Reynolds numbers, a result that is consistent with the observations at the margins of turbulent jets. This result contradicts the prediction of independence of this observable on Re from simple scaling

arguments. We have explicitly checked the prediction from the Lattice-Boltzmann simulation of the real conditions of the experiment and find also no dependence of those fluctuations with Re. Altogether, the evidence is that the decrease of the relative fluctuations with Re would be a genuine active effect of bubbles (not contained in the passive tracer picture). This informs us that bubbles do not behave in this respect as passive tracers, but we cannot conclude on whether the presence of bubbles modifies significantly the degree of turbulence of the carrier flow, at the small void fraction here considered.

- We have performed a thorough statistical characterization of the first passage-time statistics for the separation of close pairs of passive tracers in our Lattice-Boltzmann simulations. We show that the average distance between them increase exponentially in time with an effective exponent that depends on the degree of turbulence of the fluid. In the case of apparent pairs, they separate with a linear dependence in time. The comparison with actual bubble pairs in experiments shows a similar tendency of the separation rate with Re but in general the comparison is not conclusive because of the small number of real pair events in the experiments (which cannot be repeated at will) in comparison with dominant statistics of apparent pairs.

- We have solved numerically the Navier-Stokes equation coupled to thermal and solutal diffusion for the evolution of dopant concentration in semiconductor Bridgman solidification. The problem has been solved under the effect of stochastic g-jitters transversal to the temperature gradients. We have systematically characterized the response of the segregation parameter that measure the final quality of the crystal. It has been observed that the low-frequency part of the g-jitter spectrum is strongly dominant with respect to the overall response of the system, even if orders of magnitude smaller than the other high frequency components of the g-jitter spectrum.

- We have proposed and checked a very simple heuristic model, for the segregation of the dopant in semiconductor crystal growth, that defines a low-frequency approximation of the linear response of the system with two effective time scales, one from viscous dissipation and another from solutal diffusion. Those parameters can be estimated a priori but they are better fitted from one single realization of the g-jitter signal. After this fit, the model reproduce remarkably well the results from the full numerical integration of the problem, for any arbitrary signal with good accuracy and huge computational cost savings in relation to the full computational problem. The approach is a valuable predictive tool to estimate effects of arbitrary g-jitters at very low computational cost.

The results of this thesis have been partially published, but remain yet unpublished to a large extent. Two publications have already been accepted and two more are currently in preparation. The accepted publications are:

- P. Bitlloch, X. Ruiz, L. Ramírez-Piscina, J. Casademunt, "Spatial structure and velocity fluctuations in turbulent bubble jets in microgravity", *International Journal of Transport Phenomena*, **12**(3-4), 189-197 (2011).

- X. Ruiz, P. Bitlloch, L. Ramírez-Piscina, J. Casademunt, "Impact of stochastic accelerations on dopant segregation in microgravity semiconductor crystal growth", *Journal of Crystal Growth* (2012), in press.
  DOI: http://dx.doi.org/10.1016/j.jcrysgro.2012.06.027.

The first one contains the first part of chapter 3, with the discussion of the theoretical approach. The data analysis from the drop tower experiments of turbulent bubbles and its comparison with the theoretical prediction, as it is discussed in the second part of chapter 3 will be published in another paper, currently in preparation. The second accepted publication corresponds essentially to the entire chapter 5. Finally, the results of chapter 4, including the description of the experiment, the Lattice-Boltzmann simulations and the data analysis, are expected to give rise to another paper, also in preparation. In addition, the results of this thesis have been presented in a number of specialized conferences and meetings in the field of microgravity, and have reached the community with significant impact even before their publication. In this sense, it is worth mentioning the interest expressed by the European Office of Aerospace Research and Development (EOARD), as part of the United States Air Force Office of Scientific Research (AFOSR), to the point that they have offered to fund the continuation of our research for the coming three years, extending it to include phase change and thermal management for space applications. This EOARD project is currently in force.

6.2 Perspectives of future work

The perspectives for continuation of the work here reported encompass two main areas: (i) the completion of the study of bubble suspensions, from the data already acquired in the past campaigns in the ZARM Drop Tower, and its full publication; and (ii) the pursuit of an extension of the methods and ideas of the present study to include heat exchange and control.

(i) The huge amount of experimental data, over 350 Gbyte in high speed movies, from the 36 drops at ZARM has not been fully processed. A selected set of drops that performed optimally were selected for the presented data analysis.

However, some others present anomalies and malfunctions of the experimental setup are important to analyze, in order to improve the know-how for future experiments, given the limited access to repetition of this type of experiments. With this analysis and the completion of the particle-tracking processing, possibly with some improvement in the statistics of some observations, we will conclude the first part of this study, which aimed at developing the capacity of creating controlled bubble suspensions and to use it in a first characterization of simple cases. After this proof of concept, the method could now be pursued in more refined studies that could build on the experience of these first campaigns. An interesting complementary study that would not require microgravity conditions would be the characterization of the carrier flow in the exact same experimental setup, with Particle Image Velocimetry techniques (without bubbles), to allow for a more direct comparison of the passive vs active role of bubbles. The possibility to include the PIV system in the capsule for the full two-phase flow in microgravity, is technically possible but much more complicated.

(ii) The main effort in the next years will be devoted to the EOARD project *Injection of nucleate-boiling slug flows into a heat exchange chamber*, for which ESA has already committed to fund 4 campaigns at the ZARM facilities during this period, for a total of 64 new drops, under project *Slug Boiling*. The main idea is to devise a new system of slug flow injection, inspired in our previous studies, but forming bubbles out of liquid by local boiling, rather than two-phase mixing. Suspension of vapor bubbles once injected in a liquid cavity will then be used to study the behavior of vapor/liquid bubble suspensions under different heat control conditions for both fundamental and applied interests.

Indeed, one of the most critical issues for applications in space technology is precisely the development of high performance thermal management systems that take advantage of the large latent heat transportation. In particular, many thermal control systems involve liquid/vapor phase change in flowing conditions, a situation that is known as flow boiling. Although the interest on flow boiling in microgravity heat transfer is high, the existing experimental data is still quite limited, fragmentary, and often incoherent, while the knowledge of the fundamental physical mechanisms involved is far from satisfactory. Most research efforts so far have been driven more by the urgency of the engineering need of quantitative characterization, than the fundamental understanding of the physics involved. It is the purpose of the proposed research to make a step forward by combining our previous expertise in management of (non-thermal) two-phase flows in microgravity, with the needs of a more basic understanding of the physical processes involved in flow boiling heat transfer. Our rationale is similar to the one behind the studies in this thesis, that is, to focus on situations that are sufficiently simple and controllable so that one can get high quality data, which can be amenable to theo-

retical analysis and interpretation. The goal is to search for fundamental insights that may eventually lead to innovative approaches and potential breakthrough in space technology. The key innovation of our research plan is to consider for the first time the induction of controlled nucleate boiling in a capillary tube, with the practical goal of achieving a periodic slug flow. Bubbles will be nucleated at specific sites and detached by a laminar cross-flow to fill the entire diameter of the capillary. Once such slug flows are properly generated, we will be able to generate novel configurations of bubble suspensions to study coalescence, phase change dynamics and heat exchange in general in a turbulent medium under controlled conditions.

Apèndix A

Resum en català

A.1 Dolls turbulents de bombolles

En els darrers anys, el nombre d'investigacions realitzades en l'àmbit dels fluids bifàsics en condicions de microgravetat s'ha incrementat substancialment. Alguns dels motius són la creixent demanda tecnològica per a aplicacions espacials i la necessitat de perfeccionar el rendiment dels dispositius utilitzats actualment per a l'exploració de l'espai. Per exemple, els sistemes de suport vital i de control ambiental són dos casos que es veurien àmpliament beneficiats pels avenços en el control de fluids bifàsics en condicions de gravetat reduïda.

En concret, la generació de suspensions de bombolles monodisperses de dimensions controlades permetria la maximització de la superfície de contacte entre gasos i líquids, fet necessari per aplicacions en motors de propulsió i reactors químics, així com en bioreactors, on es requereix una oxigenació uniforme de cultius o teixits en creixement. No obstant, fins molt recentment, a la literatura hi ha hagut una mancança d'estudis en aquests tipus de suspensions en condicions de gravetat reduïda. Un dels motius principals d'aquesta manca és la dificultat associada a la generació de bombolles de mida controlada sense l'ajuda de les forces de flotació. Típicament, els sistemes estudiats en la literatura que controlen les dimensions de les bombolles treballen amb la injecció de caudals molt petits de gas, ja sigui a partir de la formació de bombolles micromètriques o amb ritmes lents de generació, que no permeten l'obtenció d'una fracció volúmica de gas prou gran.

Recentment, el nostre grup va dur a terme una sèrie d'experiments en la torre de caiguda del ZARM ("Centre de Tecnologia Espacial Aplicada i Microgravetat") a Bremen en els que s'utilitzava per primera vegada una junció en T per a la generació de bombolles en l'àmbit de la microgravetat [Carrera et al. (2008)]. El dispositiu es basa en dos tubs capil·lars de 1.5 mm de diàmetre connectats en

forma de T. Mitjançant la injecció simultània de líquid per un dels tubs i gas per l'altre, connectat transversalment al flux principal, s'aconsegueix que les bombolles es separin degut a la combinació de les forces capil·lars i d'arrossegament, essent negligibles les forces de flotació en aquestes condicions i, per tant, proporcionant un mètode de generació de bombolles insensible a la gravetat. Així, es forma en el capil·lar de sortida un flux de bombolles equiespaiades i de mida uniforme, de l'ordre del diàmetre del tub. Aquestes són, al seu torn, injectades a una cavitat cúbica de 10 cm per banda plena de líquid, distribuint-se en una forma aproximadament cònica, corresponent a la zona turbulent del doll submergit de líquid.

És ben conegut que el grau de turbulència en un doll submergit es manté constant al llarg del seu eix. Les dimensions dels remolins que el constitueixen van augmentant amb la distància al punt d'injecció en la mateixa mesura que en disminueix la seva velocitat, mantenint l'estructura espaciotemporal del flux estadísticament invariant sota un reescalament adequat de temps i espai. Les bombolles, en canvi, mantenen el seu diàmetre constant durant tot l'experiment, causant un impacte diferent en el fluid portador que les arrossega en funció de la distància de l'injector a la que es trobin. En el moment d'entrada a la cavitat són molt grans comparades amb els gradients de velocitat del flux, mentre que a una certa distància arribarien a ser menors que les escales més petites de la turbulència. El mateix ocorre amb el seu temps de resposta a les fluctuacions de velocitat de la turbulència, atès que inicialment són incapaces de seguir les ràpides fluctuacions del flux mentre que, a una determinada distància, les fluctuacions assoleixen uns temps característics molt majors que els de resposta de les bombolles. Tot això apunta en la direcció que les bombolles haurien de causar un impacte important en el flux per als primers 5 cm de la cavitat, i decréixer gradualment el seu efecte en el doll a distàncies majors.

Com a estudi teòric de referència utilitzem el programari de FLUENT per a resoldre el camp de velocitats promig del doll turbulent. Aquest es calcula a partir del mètode de volums finits, utilitzant el model conegut com a *realizable* k-ε per a la modelització de la turbulència mitjana a cada punt del sistema. Un cop coneguda la solució estacionària del camp de velocitats, descrivim la concentració mitjana de bombolles a través d'una equació tipus Fokker-Planck per a la distribució de probabilitats de trobar una bombolla a cada posició

$$\frac{\partial P(\mathbf{r}, t)}{\partial t} + \nabla \cdot (\mathbf{U} P) = \nabla \cdot [D_p \nabla P] \, , \tag{A.1}$$

que ha sigut integrada juntament amb el camp de velocitats del flux. En aquesta aproximació, tractem les bombolles com a traçadors passius del flux mitjà, que es veuen arrossegats per advecció, seguint les línies de corrent. Al mateix temps,

es desplacen entre les diferents capes internes del doll mitjançant un procés de difusió, que reflecteix les fluctuacions associades a la turbulència. El coeficient de difusió efectiu D_p en el marc d'aquest model k-ε està relacionat amb el grau local de turbulència i ve donat per

$$D_p = 0.09 \frac{k^2}{\varepsilon} \ . \tag{A.2}$$

Les possibles discrepàncies entre aquest model i els resultats experimentals permetran discernir fins a quin punt les hipòtesis del model s'ajusten a la realitat, o cal invocar en algun moment el caràcter actiu de les bombolles per explicar algun efecte.

Donat que les mesures experimentals han sigut preses a partir de les filmacions d'una càmera d'alta velocitat, la distància de la bombolla en la direcció de la visual, perpendicular al pla enregistrat, no és mesurable. Això provoca que a l'hora de fer estadística de velocitats i posicions de bombolles i comparar amb les previsions del model, cal projectar els resultats obtinguts de les simulacions sobre la direcció de la visual. En general s'observa que les prediccions del model sobre l'estructura espaial del doll de bombolles, així com del camp de velocitats mitjà i de les seves fluctuacions, s'ajusten força bé als experiments dins del marge d'incertesa experimental, per als dos paràmetres d'injecció estudiats corresponents a $Re = 690$ i 1170. Tot i així, s'observen alguns efectes que no incorpora correctament un model de turbulència tan senzill. A distàncies grans del punt d'injecció, s'obté un angle d'obertura del doll lleugerament major que el predit per la simulació. La lleugera dependència de l'obertura del doll amb el nombre de Reynolds també sembla incorrecta en el model. Ambdós efectes molt probablement tenen a veure amb el fet que el model no captura correctament la física de la interfase entre el flux turbulent a l'interior del doll i el laminar a l'exterior. Finalment, també en els marges del doll s'observa una tendència a la baixa de la dispersió relativa de velocitats en augmentar el nombre de Reynolds, contradient tant la predicció del model k-ε (que apunta en la direcció contrària) com simples arguments d'escala (que prediuen independència del nombre de Reynolds). Aquestes observacions són molt probablement la signatura d'un comportament actiu de les bombolles en el flux.

A.2 Suspensions de bombolles en un canal turbulent

L'objectiu d'una bona part del present treball és la generació i l'estudi de suspensions de bombolles monodisperses en el si d'un flux turbulent. A tal efecte

utilitzem quatre juncions capil·lars en T, com la utilitzada en la secció anterior, per injectar bombolles en un canal de secció quadrada i dimensions de 80x10x10 cm³. El flux en el canal es controla independentment dels paràmetres que governen la generació de les bombolles, de manera que podem variar el grau de turbulència en el fluid portador sense modificar les dimensions de les bombolles ni la seva freqüència d'injecció. Els paràmetres d'estudi han estat triats de manera que les bombolles (típicament en el rang entre 1.6 mm i 2.5 mm) siguin menors que els remolins més energètics del medi (de l'ordre de 10 mm), per tal d'afavorir la seva dispersió en el canal d'una forma el més homogènia possible, i a la vegada evitar fenòmens de coalescència. Al mateix temps, les bombolles són majors que l'escala de Kolmogorov, que ens determina les fluctuacions més petites del medi (de l'ordre de 0.1 mm), per tal que potencialment puguin tenir un paper més actiu en el flux, en contraposició al paper de simples traçadors passius del mateix. A més, en el rang de paràmetres escollit les bombolles són essencialment indeformables, mantenint per tant la seva esfericitat, cosa que en simplifica considerablement el seu estudi.

Per a caracteritzar la turbulència s'ha preparat un codi de simulació tipus Lattice-Boltzmann. Aquest ha sigut degudament paral·lelitzat i executat en el supercomputador *Marenostrum* del *Barcelona Supercomputer Center* utilitzant 256 processadors. També s'ha calculat durant llargs períodes de temps en un clúster de 16 nodes propi del Departament de Física Aplicada de la Universitat Politècnica de Catalunya. Els resultats de les simulacions per a $Re = 3800$ estan en ple acord amb els obtinguts per Pattison et al. (2009). S'ha resolt el flux també per a un cas amb $Re = 12700$. En comparar els resultats entre ambdós nivells de turbulència es troba que el grau de fluctuacions escalades segons la velocitat característica del medi es manté constant independentment del Re, resultat que està d'acord amb els arguments d'escala de la turbulència completament desenvolupada.

S'han dut a terme un total de trenta-sis llançaments del nou sistema experimental des de la torre de caiguda del ZARM i s'ha aconseguit, per primera vegada en microgravetat, una suspensió monodispersa de bombolles en el sí d'un flux turbulent. Els resultats de l'anàlisi de dades experimentals mostren un efecte observat per primera vegada: la dinàmica de relaxació de l'anomenada pseudo-turbulència, és a dir, de l'excés de turbulència generat col·lectivament per les bombolles en la fase de gravetat normal degut a les forces de flotació. Hem observat que la seva velocitat mitjana relaxa amb un temps característic de $\tau = 1.0$ s, mentre que la dispersió de velocitats, en canvi, relaxa amb una escala de temps més gran, de $\tau_x = 2.4$ s en la direcció del flux i de $\tau = 3.2$ s en la direcció transversal a aquest.

Pel que fa a les mesures de la dispersió relativa de velocitats, observem en general una tendència d'aquest observable a disminuir quan augmentem el nombre de Reynolds. Aquest resultat és coincident amb la tendència observada per a dolls

turbulents (en condicions diferents), i apunta a un efecte genuïnament actiu en el flux, en el sentit que les bombolles manifesten un comportament diferent del de traçadors passius.

Finalment s'ha estudiat l'estadística de temps de separació entre parelles de bombolles i s'ha comparat amb la predicció de traçadors passius simulada amb el mètode de Lattice-Boltzmann. Per bé que l'estadística dels experiments no permet detectar efectes actius, s'ha pogut caracteritzar el temps de separació de parelles de bombolles reals (no aparents).

A.3 Efecte de les vibracions gravitatòries residuals en solidificació tipus Bridgman de semiconductors

L'impacte causat per diferents tipus de pertorbacions d'origen mecànic de l'entorn microgravitatori, en la qualitat final de cristalls crescuts en plataformes orbitals ha estat des de fa temps un tema de crucial importància tecnològica. Les típiques pertorbacions sofertes en els entorns de microgravetat comporten diversos tipus d'acceleracions residuals en forma de polsos breus, trens de polsos de duració finita, valors residuals quasi-estacionaris i, per últim, sorolls de fons d'alta freqüència o vibracions gravitatòries.

Donat que l'estructura de freqüències d'un senyal acceleromètric real en una plataforma orbital és sovint molt complexa, atès el gran nombre de fonts incontrolades que hi contribueixen en un entorn donat de microgravetat, una possible estratègia proposada ha sigut modelitzar aquestes vibracions com una gravetat estocàstica.

La caracterització estocàstica de vibracions gravitatòries va ser discutida per primera vegada per Thomson et al. (1997), i la seva modelització va ser aplicada a diversos processos físics rellevants tant per a la física fonamental com per a la tecnologia espacial, incloent estudis de solidificació de suspensions col·loïdals, interfases entre fluids o la convecció tèrmica natural. Nosaltres hem seguit aquest punt de vista per estendre'l a l'estudi del creixement de cristalls de semiconductor, cas que implica un grau més de complexitat, en incorporar fenòmens de convecció termosolutal induïts per les acceleracions residuals.

Com a indicadors d'impacte de les vibracions residuals en la qualitat dels cristalls hem utilitzat l'evolució temporal dels paràmetres de segregació longitudinal i transversal, que mostren les variacions de concentració del dopant en les respectives direccions del cristall. Hem modelitzat una acceleració estocàstica genèrica

a través d'un senyal de soroll de banda estreta, definida com un procés estocàstic Gaussià caracteritzat per tres paràmetres: la intensitat del soroll, una freqüència dominant a on aquesta pot estar picada i un temps de correlació que controla l'amplada de banda de l'espectre de freqüències. Aquest procés estocàstic interpola entre els casos extrems de soroll blanc i soroll monocromàtic, permetent-nos una modelització més realista dels senyals obtinguts en entorns de microgravetat.

La resposta convectiva del camp de velocitats en una cavitat, deguda a un senyal estocàstic vibratori transversal a un gradient tèrmic, va ser estudiada en detall per Thomson et al. (1995). Nosaltres estenem el treball per incloure configuracions típiques de creixement de cristalls i l'acoblament de la concentració de dopant al camp de velocitats. També ens centrem en valors de paràmetres i configuracions properes a condicions realistes d'experiments de solidificació a l'espai. L'objectiu és obtenir una caracterització quantitativa del fenomen de segregació que vingui determinada com una funció de l'estadística de vibracions gravitatòries. Hem realitzat la simulació completa del problema i a més, hem proposat un model heurístic simplificat que captura el comportament del sistema amb una precisió notable, amb només uns pocs paràmetres lliures que poden ser ajustats en un sol cas, romanent constants per a qualsevol altra senyal. El model proporciona una comprensió qualitativa i quantitativa de la resposta del camp de dopants a les acceleracions, convertint-se en una eina predictiva de gran valor pràctic i teòric, que permet comprovar els efectes de qualsevol senyal acceleromètric arbitrari amb un cost computacional dramàticament reduït. Com a conclusió general d'aquest estudi, trobem que la resposta del sistema ve fortament dominada per les components de baixa freqüència del soroll gravitatori, inclús malgrat que aquesta zona de l'espectre tingui un contingut diversos ordres de magnitud menor que altres zones de l'espectre a freqüència finita.

References

Aidun, C. K. and Clausen, J. R. (2010), "Lattice-Boltzmann method for complex flows", *Annual Review of Fluid Mechanics*, **42**(1), 439 – 472.

Alexander, F. J., Chen, S. and Sterling, J. D. (1993), "Lattice Boltzmann thermohydrodynamics", *Phys. Rev. E*, **47**, R2249–R2252.

Arias, S. (2011), *An analysis of two-phase flows in conditions relevant to microgravity*, PhD Thesis.

Arias, S., Ruiz, X., Casademunt, J., Ramírez-Piscina, L. and González-Cinca, R. (2009), "Experimental study of a microchannel bubble injector for microgravity applications", *Microgravity Sci. Technol.*, **21**(1), 107–111.

Balachandar, S. and Eaton, J. K. (2010), "Turbulent dispersed multiphase flow", *Annu.Rev.Fluid Mech.*, **42**, 111–133.

Benz, K. W. and Dold, P. (2002), "Crystal growth under microgravity: present results and future prospects towards the International Space Station", *Journal of Crystal Growth*, pp. 1638 – 1645.

Bessonov, O. A. and Polezhaev, V. I. (2001), "Mathematical Modeling of Convection in the DACON Sensor under Conditions of Real Space Flight", *Cosmic Research*, **39**, 159–166.

Bhatnagar, P. L., Gross, E. P. and Krook, M. (1954), "A Model for Collision Processes in Gases. I. Small Amplitude Processes in Charged and Neutral One-Component Systems", *Phys. Rev.*, **94**, 511–525.

Biesheuvel, A. and Wijngaarden, L. V. (1984), "Two-phase flow equations for a dilute dispersion of gas bubbles in liquid", *Journal of Fluid Mechanics*, **148**, 301–318.

Binney, J. and Tremaine, S. (2008), *Galactic Dynamics*, Princeton series in astrophysics.

Bitlloch, P., Ruiz, X., Ramírez-Piscina, L. and Casademunt, J. (2011), "Spatial structure and velocity fluctuations in turbulent bubble jets in microgravity", *International journal of transport phenomena*, **12**(3-4), 189–197.

Boltzmann, L. (1872), "Weitere Studien über das Wärmegleichgewicht unter Gasmolekülen", *Sitzungsberichte Akademie der Wissenschaften*, **66**, 275 – 370.

Brennen, C. E. (2005), *Fundamentals of multiphase flow*, Cambridge University Press.

Caroli, B., Caroli, C. and Ramirez-Piscina, J. (1993), "Initial front transients in directional solidification of thin samples of dilute alloys", *Journal of Crystal Growth*, **132**, 377 – 388.

Carrera, J., Parthasarathy, R. and Gollahalli, S. (2006), "Bubble formation from a free-standing tube in microg", *Chem. Eng. S.*, **61**.

Carrera, J., Ruiz, X., Ramírez-Piscina, L., Casademunt, J. and Dreyer, M. (2008), "Generation of a Monodisperse Microbubble Jet in Microgravity", *AIAA Journal*, **46**(8), 2010 – 2019.

Carrica, P. M., Bonetto, F. J., Drew, D. A. and Lahey, R. T. (1998), "The interaction of background ocean air bubbles with a surface ship", *International Journal for Numerical Methods in Fluids*, **28**(4), 571–600.

Casademunt, J. and Viñals, J. (2001), "Stochastic modelling of the residual acceleration field in a microgravity environment", *Astrophysics and Space Science*, **276**, 123–133.

Casademunt, J., Zhang, W., Viñals, J. and Sekerka, R. (1993), "Stability of a fluid surface in a microgravity environment", *AIAA Journal*, **31**, 2027 – 2031.

Chen, S. and Doolen, G. D. (1998), "Lattice Boltzmann method for fluid flows", *Annual Review of Fluid Mechanics*, **30**(1), 329–364.

Chew, Y. T., Niu, X. D. and Shu, C. (2006), "Three-dimensional lattice Boltzmann BGK model and its application to flows with heat transfer in a rectangular microchannel", *International Journal for Numerical Methods in Fluids*, **50**(11), 1321 – 1334.

Colin, C., Legendre, D. and Fabre, J. (2001), "Bubble Distribution in a Turbulent Pipe Flow", *First International Symposium on Microgravity Research and Applications in Physical Sciences and Biotechnology.*, **ESA SP-454**.

d'Humieres, D., Ginzburg, I., Krafczyk, M., Lallemand, P. and shi Luo, L. (2002), "Multiple-relaxation-time lattice Boltzmann models in three dimensions.", *Philos Transact A Math Phys Eng Sci.*, **360**(1792), 437 – 451.

Du, R. and Shi, B. (2006), "A novel scheme for force term in the lattice BGK model", *International Journal of Modern Physics C (IJMPC)*, **17**(7), 945 – 958.

Duffar, T. (2010), *Bulk Crystal Growth Under Microgravity Conditions, in "Bulk Crystal Growth of Electronic, Optical & Optoelectronic Materials" (ed P. Capper)*, John Wiley & Sons.

Duffar, T., Benz, K. W. and Brinkman, A. (2001), "25 Years of Crystal Growth Experiments under Microgravity Conditions", *Proceedings of the First International Symposium on Microgravity Research and Applications in Physical Sciences and Biotechnology, Ed. O. Minster and B. Schürmann. European Space Agency,ESA*, .

Duffar, T. and Garandet, J. (2000), "Gravity driven disturbances during Bridgman crystal growth", *Acta Astronautica*, **47**, 317 – 323.

Fox, R., Gatland, I., Roy, R. and Vemuri, G. (1988), "Fast, accurate algorithm for numerical simulation of exponentially correlated colored noise", *Physical Review A*, **38**, 5938 – 5940.

Friedrich, J., Dagner, J., Hainke, M. and Müller, G. (2003), "Numerical modelling of crystal growth and solidification experiments carried out under microgravity conditions", *Crystal Research and Technology*, **38**, 726 –733.

Garandet, J., Favier, J. and Camel, D. (1994), *Segregation Phenomena in crystal growth from the melt*, Vol. 2 (Chap. 12) of *Handbook of Crystal Growth*, Elsevier.

Garandet, J. P., Corre, S., Kaddeche, S. and Alboussiere, T. (2000), "The influence of convection on the duration of the initial solute transient in alloy crystal growth", *Journal of Crystal Growth*, **209**, 970 – 982.

Gardiner, C. (2009), *Stochastic Methods. A Handbook for the Natural and Social Sciences*, Vol. 13 of *Springer Series in Synergetics*, Springer.

Gordillo, J. M., Cheng, Z., Ganan-Calvo, A. M., Márquez, M. and Weitz, D. A. (2004), "A new device for the generation of microbubbles", *Physics of Fluids*, **16**(8), 2828–2834.

Gore, R. A. and Crowe, C. T. (1989), "Effect of particle size on modulating turbulence intensity", *International Journal of Multiphase Flow*, **15**(2), 279–285.

Hadamard, J. S. (1911), "Mouvement permanent lent d'une sphere liquide et visqueuse dans un liquide visqueux", *C. R. Acad. Sci. Paris*, **152**, 1735–1738.

Haugan, M. P. and Lammerzahl, C. (2001), "Principles of Equivalence: Their Role in Gravitation Physics and Experiments that Test Them", *Lect. Notes Phys.*, **562**, 195–212.

Hays, L. G. and Elliott, D. G. (1974), "Two-phase Engine", *United States Patent 3972195*, . Assignee: Biphase Engines, Inc.

He, X. and Luo, L.-S. (1997), "Theory of the lattice Boltzmann method: From the Boltzmann equation to the lattice Boltzmann equation", *Phys. Rev. E*, **56**, 6811–6817.

Hecht, M. and Harting, J. (2008), "Implementation of on-site velocity boundary conditions for D3Q19 lattice Boltzmann", *Journal of Statistical Mechanics: Theory and Experiment*, **2010**(01), 13.

Hill, S., Kostyk, C., Motil, B., Notardonato, W., Rickman, S. and Swanson, T. (2010), *Thermal management systems roadmap.*, National Aeronautics and Space Administration.

Hou, S., Sterling, J., Chen, S. and Doolen, G. D. (1994), "A Lattice Boltzmann Subgrid Model for High Reynolds Number Flows", *Fields Institute Communications*, **6**, 1–18.

Huang, K. (1963), *Statistical Mechanics*, John Wiley & Sons, Inc.

Hurlbert, K., Bagdigian, B., Carroll, C., Jeevarajan, A., Kliss, M. and Singh, B. (2010), *Human health, life support and habitation systems roadmap*, National Aeronautics and Space Administration.

Ishii, M. and Hibiki, T. (2011), *Thermo-Fluid Dynamics of Two-Phase Flow (second edition)*, Springer.

Jafari, S. and Rahnama, M. (2011), "Shear-improved Smagorinsky modeling of turbulent channel flow using generalized Lattice Boltzmann equation", *International Journal for Numerical Methods in Fluids*, **67**(6), 700–712.

James, F. (1990), "A review of pseudorandom number generators", *Computer Physics Communications*, **60**, 329–344.

Jiménez, J. (1997), "Oceanic turbulence at millimeter scales", *Scientia Marina*, **61**(1), 47–56.

Kinsman, B. (2012), *Wind Waves: Their Generation and Propagation on the Ocean Surface*, Dover Publications.

Kolmogorov, A. N. (1941), "The Local Structure of Turbulence in Incompressible Viscous Fluid for Very Large Reynolds Numbers*", *Dokl. Akad. Nauk SSSR*, **30**(4), 299–302. (*In Russian, translated to English in 1991 at Proc. R. Soc. London A (434):9-13).

Kytömaa, H. K. (1987), *Stability of the structure in multicomponent flows*, Ph.D. Thesis. California Institute of Technology.

Landau, L. D. and Lifshitz, E. (1987), *Fluid Mechanics*, Course of Theoretical Physics - Volume 6, Pergamon Press.

Latt, J., Chopard, B., Malaspinas, O., Deville, M. and Michler, A. (2008), "Straight velocity boundaries in the lattice Boltzmann method", *Phys. Rev. E*, **77**, 056703.

Levtov, V. L., Romanov, V. V., Boguslavsky, A. A., Sazonov, V. V. and Sokolov, S. M. (2009), "Determination of quasi-static microaccelerations onboard a satellite using video images of moving objects", *Cosmic Research*, **47**, 513–524.

Lighthill, M. and Whitham, J. (1955), "On kinematic waves. I: Flow movement in long rivers. II: A Theory of traffic flow on long crowded roads", *Proc. Royal Soc. of London A*, **229**(1178), 281–345.

Lin, C.-L. and Lai, Y. G. (2000), "Lattice Boltzmann method on composite grids", *Physical Review E*, **62**, 2219–2225.

Lou, Y.-Q. (2005), "Two-fluid Dynamics in Clusters of Galaxies Pairwise Velocity Statistics of Dark Halos", *Chinese Journal of Astronomy and Astrophysics*, **5**(1), 6.

Marsaglia, G., Narasimhan, B. and Zaman, A. (1990), "A random number generator for PC", *Computer Physics Communications*, **60**, 345–349.

Maxey, M., Chang, E. and Wang, L. (1996), "Interactions of Particles and Microbubbles with Turbulence", *Experimental Thermal and Fluid Science*, **12**, 417–425.

Mazzitelli, I. M. and Lohse, D. (2009), "Evolution of energy in flow driven by rising bubbles", *Physical Review E*, **79**(066317).

Mazzitelli, I. M., Lohse, D. and Toschi, F. (2003), "The effect of microbubbles on developed turbulence", *Physics of fluids*, **15**(1), L5–L8.

McQuillen, J., Colin, C. and Fabré, J. (1998), "Ground-based gas-liquid flow research in microgravity conditions: state of knowledge", *Space Forum*, pp. 165–203.

Melling, A. and Whitelaw, J. (1976), "Turbulent flow in a rectangular duct", *J.Fluid Mech.*, **78**(2), 289–315.

Meyer, M., Johnson, L., Palaszewsky, B., Goebel, D., White, H. and Coote, D. (2010), *In-space propulsion systems roadmap*, National Aeronautics and Space Administration.

Narain, R., Golas, A., Curtis, S. and Lin, M. C. (2009), "Aggregate dynamics for dense crowd simulation", *ACM Trans. Graph.*, **28**(5), 122:1–122:8.

NASA (2005), *NASA sounding rocket program handbook*, Sounding rockets program office. Suborbital & Special orbital projects directorate.

Nikitin, S. A., Polezhaev, V. I. and Sazonov, V. V. (2001), "Measurement of the Quasistatic Component of Microaccelerations Using a Convection Sensor onboard a Satellite", *Cosmic Research*, **39**, 167–174.

Nourgaliev, R., Dinh, T., Theofanous, T. and Joseph, D. (2003), "The lattice Boltzmann equation method: theoretical interpretation, numerics and implications", *International Journal of Multiphase Flow*, **29**(1), 117 – 169.

Obukhov, A. M. (1941), "Spectral energy distribution in turbulent flow", *Dokl. Akad. Nauk USSR*, **32**(1), 22–24.

Ohta, H., Baba, A. and Gabriel, K. (2002), "Review of existing research on microgravity boiling and two-phase flow", *Ann. N.Y. Acad. Sci.*, pp. 410–427.

Pattison, M. J., Premnath, K. N. and Banerjee, S. (2009), "Computation of turbulent flow and secondary motions in a square duct using a forced generalized lattice Boltzmann equation", *Phys. Rev. E*, **79**, 026704.

Peltzer, R. D. and Griffin, O. M. (1988), "Stability of a Three-Dimensional Foam Layer in Seawater", *Journal of Geophysical Research*, **93**(C9), 10,804–10,812.

Polezhaev, V. I. and Nikitin, S. (2009), "Conjugate Problems of Transport Phenomena under Quasi-steady Microaccelerations in Realistic Spaceflight", *Annals of the New York Academy of Sciences*, pp. 570 – 584.

Premnath, K. N., Pattison, M. J. and Banerjee, S. (2009), "Dynamic subgrid scale modeling of turbulent flows using lattice-Boltzmann method", *Physica A Statistical Mechanics and its Applications*, **388**, 2640–2658.

Pruppacher, H. R., Klett, J. D. and Wang, P. K. (1998), "Microphysics of Clouds and Precipitation", *Aerosol Science and Technology*, **28**(4), 381–382.

Qian, Y., d'Humières, D. and Lallemand, P. (1992), "Lattice BGK models for Navier-Stokes Equation", *Europhys. Lett.*, **17**, 479–484.

R.Clift, Grace, J. and Weber, M. (1978), *Bubbles, Drops and Particles*, Academic Press.

Reichardt, H. (1942), *Gesetzmässigkeiten der freien Turbulenz*, VDI - Foeschungsheft 414. (2nd ed.1951).

Richards, P. (1956), "Shockwaves on the highway", *Operations Research*, **4**(1), 42–51.

Richardson, L. (1922), *Weather Prediction by Numerical Process*, Cambridge University Press.

Ruiz, X. (2007), "Modelling of the influence of residual gravity on the segregation in directional solidification under microgravity", *Journal of Crystal Growth*, **303**, 262 – 268.

Ruiz, X., Bitlloch, P., Ramírez-Piscina, L. and Casademunt, J. (2012), "Impact of stochastic accelerations on dopant segregation in microgravity semiconductor crystal growth", *Journal of Crystal Growth*, . In press, DOI: http://dx.doi.org/10.1016/j.jcrysgro.2012.06.027.

Rybczynski, W. (1911), "On the translating motion of a fluid sphere in a viscous medium", *Bull. Acad. Sci. Cracovie*, **40**, 40–46.

Salazar, J. P. and Collins, L. R. (2009), "Two-particle dispersion in isotropic turbulent flows", *Annu.Rev.Fluid Mech.*, **41**, 405–432.

Schlichting, H. (1979), *Boundary-Layer Theory*, McGraw-Hill Classic Textbook Reissue. Seventh Edition.

Shih, T.-H., Liou, W. W., Shabbir, A., Yang, Z. and Zhu, J. (1995), "A new k-ϵ eddy viscosity model for high reynolds number turbulent flows", *Computers & Fluids*, **24**(3), 227 – 238.

Smagorinsky, J. (1963), "General circulation experiments with the primitive equations: I. The basic experiments.", *Monthly Weather Review*, **91**, 99–164.

Smith, V. G., Tiller, W. A. and Rutter, J. W. (1955), "A mathematical analysis of solute redistribution during solidification", *Canadian Journal of Physics*, **33**, 723 – 745.

Sterling, J. D. and Chen, S. (1996), "Stability analysis of lattice Boltzmann methods", *J. Comput. Phys.*, **123**, 196–206.

Stokes, G. G. (1851), "On the Effect of the Internal Friction of Fluids on the Motion of Pendulums", *Cambridge Philos. Trans.*, **9**, 8–106. (Reprinted in *Mathematical and Physical Papers*, 2nd ed., Vol. 3. Cambridge Library Collection, 2009).

Succi, S. (2001), *The Lattice Boltzmann Equation for Fluid Dynamics and Beyond*, Oxford University press.

Sun, H., Liu, H. and Guo, L.-J. (2005), "PEM fuel cell performance and its two-phase mass transport", *Journal of Power Sources*, **143**, 125–135.

Suñol, F. (2011), *Bubble and droplet flow phenomena at different gravity levels*, PhD Thesis.

Thomson, J. R., Casademunt, J., Drolet, F. and Viñals, J. (1997), "Coarsening of solid-liquid mixtures in a random acceleration field", *Physics of Fluids*, **9**, 1336 – 1343.

Thomson, J. R., Casademunt, J. and Viñals, J. (1995), "Cavity flow induced by a fluctuating acceleration field", *Physics of Fluids*, **7**, 292 – 301.

Tiller, W. A., Jackson, K. A., Rutter, J. W. and Chalmers, B. (1953), "The redistribution of solute atoms during the solidification of metals", *Acta Metallurgica*, **1**, 428 – 437.

Tryggvason, G., Lu, J., Biswas, S. and Esmaeeli, A. (2006), "Studies of Bubbly Channel Flows by Direct Numerical Simulations", *Conference on Turbulence and Interactions TI2006*, .

van Driest, E. (1956), "On turbulent flow near a wall", *J. Aeronaut Sci.*, **23**(11), 1007–1011.

Verhoeven, J., Gill, W., Puszynski, J. and Ginde, R. (1988), "Macrosegregation during convetion-free plane front solidification.I. Rectilinear geometry", *Journal of Crystal Growh*, **89**, 189 – 201.

Verschaeve, J. C. G. (2009), "Analysis of the lattice Boltzmann Bhatnagar-Gross-Krook no-slip boundary condition: Ways to improve accuracy and stability", *Phys. Rev. E*, **80**, 036703.

Versteeg, H. and Malalasekera, W. (1995), *An introduction to computational fluid dynamics. The finite volume method*, Pearson Prentice Hall.

Voit, J. (2005), *The Statistical Mechanics of Financial Markets*, Springer.

Webb, R. L. (1994), *Principles of enhanced heat transfer*, John Wiley & Sons, Inc.

Wichterle, K., Smutná, K. and Večeř, M. (2009), "Shape and rising velocity of bubbles", *Proceedings of the 36th International Conference of Slovak Soc.of Chem. Eng.(SSCHE)*, .

Yin, X., Koch, D. L. and Verberg, R. (2006), "Lattice-Boltzmann method for simulating spherical bubbles with no tangential stress boundary conditions", *Phys. Rev. E*, **73**, 026301.

Zavalishin, D. A., Belyaev, M. Y. and Sazonov, V. V. (2009), "Estimation of dynamic characteristics of the International Space Station from measurements of microaccelerations", *Cosmic Research*, **47**, 173–184.

Zavalishin, D. A., Belyaev, M. Y. and Sazonov, V. V. (2010), "Determination of characteristic frequencies of elastic oscillations of the International Space Station construction", *Cosmic Research*, **48**, 352–361.

Zhang, W., Casademunt, J. and Viñals, J. (1993), "Study of the parametric oscillator driven by narrow band noise to model the response of a fluid surface to time-dependent accelerations", *Physics of Fluids A*, **5**, 3147 – 3161.

Zou, Q. and He, X. (1997), "On pressure and velocity boundary conditions for the lattice Boltzmann BGK model", *Physics of Fluids*, **9**(6), 1591–1598.